

EVENT-BY-EVENT NET-LAMBDA FLUCTUATIONS IN
LEAD-LEAD COLLISIONS AT $\sqrt{s_{NN}} = 5.02$ TeV WITH THE ALICE
DETECTOR AT THE LHC

by
Ejiro Naomi Umaka

A dissertation submitted to the Department of Physics,
College of Natural Sciences and Mathematics
in partial fulfillment of the requirements for the degree of

Doctor of Philosophy
in Physics

Chair of Committee: Rene Bellwied
Committee Member: Ratti Claudia
Committee Member: Ed Hungerford
Committee Member: Yuliya Gorb
Committee Member: Donna Stokes

University of Houston
May, 2020

ABSTRACT

This dissertation documents the calculation of the cumulants of the net- Λ multiplicity distribution in Pb-Pb collisions at $\sqrt{s_{NN}} = 5.02$ TeV with the ALICE detector at the LHC so as measure, on an event-by-event basis, the effects of quantum number conservation during the phase transition of strongly interacting matter. The Quantum Chromodynamics (QCD) phase diagram depicts a phase transition from a deconfined quark-gluon plasma phase into confined hadronic matter. The quark-gluon plasma is created in ultra-relativistic heavy-ion collisions such as the heavy-ion collisions measured in ALICE, which stands for A Large Ion Collider Experiment. ALICE is a general-purpose, heavy-ion detector at the CERN Large Hadron Collider which focuses on QCD, the strong-interaction sector of the Standard Model.

Called the QGP for short, the quark-gluon plasma only exists for a short time (10^{-23} seconds), and at LHC energies, it is only slightly bigger than the size of a proton, making direct observation impossible. Despite this, the temperature and baryon chemical potential of the QGP formation can be indirectly characterized by linking theory (thermodynamic susceptibilities calculated in lattice QCD) and phenomenological models with observables created in the collision such as event-by-event net-particle multiplicity fluctuation measurements. In heavy-ion collisions, fluctuations can be as a result of inhomogeneities in the energy and baryon number deposition in the initial state or due to thermal fluctuations in the subsequent evolution of the system. The latter represents the fluctuations under investigation, particularly in the vicinity of a phase transition. Trivial fluctuations induced by the experimental measurement process such as volume fluctuation effects and baryon number conservation also exist and they are addressed in this analysis.

The observables studied and documented in this dissertation are the first two cumulants of the net- Λ distribution. In particular, the mean and variance of the net- Λ distribution and their ratios were calculated and compared to statistical baselines to search for deviation, if any, from Poisson behavior. The pseudorapidity dependence of the ratio of the second cumulant of the net- Λ distribution to the sum of the mean of the Λ and $\bar{\Lambda}$ distributions was also calculated to explore global conservation laws. The deviation from Poisson behavior found in the second cumulant is attributed to global baryon number conservation.

AUTHOR'S CONTRIBUTION

The work presented in this dissertation was done while I a PhD student with the ALICE collaboration. The work analyzes Pb-Pb data collected in 2015 to measure the event-by-event net- Λ distribution. The $\Lambda \rightarrow p\pi^-$ is reconstructed by a cut based approach, where cuts are applied on the daughter tracks and V0 selections. Some of the reconstruction techniques follow the approach done by the ALICE Strangeness PAG [72]. However, different selections were chosen while reconstructing the Λ and $\bar{\Lambda}$ in order to increase the purity of the sample, since fluctuation measurements rely heavily on a pure multiplicity sample.

Apart from building on pre-existing framework for the Λ and $\bar{\Lambda}$ reconstruction, all the analysis work presented in this dissertation are my own. The analysis work includes: signal extraction, corrections, systematic uncertainties estimation, and calculation of the cumulants of the Λ and $\bar{\Lambda}$ distributions. The correction procedure includes corrections for background due to combinatoric pairs, due to secondary Λ and $\bar{\Lambda}$ from weak decays, and finally, due to efficiency losses. The correction to remove secondary Λ and $\bar{\Lambda}$ follows the same approach used by the ALICE Strangeness PAG.

The analysis framework used to reconstruct Λ and $\bar{\Lambda}$ particles relies on the ALICE Time Projection Chamber (TPC) for identifying its daughter tracks (p and π). At the time when the data was collected, the TPC design was based on the Multi-Wire Proportional Chamber (MWPC) technique with cathode pad readout. However, due to substantial increase in luminosities expected after the second long shutdown (LS2) of the LHC, the current ALICE TPC readout chamber (with a gating grid) had to be replaced due to the expected increase in data acquisition rate by a factor of 100. The new readout chamber design is based on Gas Electron Multiplier (GEM) technology that operates on continuous mode due to intrinsic ion back flow blocking capabilities. My contribution to the readout chamber upgrade includes: quality assurance tests on the GEM foils, electrical measurements of the readout chambers and trial runs of the new readout chambers in the ALICE cavern.

ACKNOWLEDGMENTS

There are a number of people that in one way or another led to my decision to acquire a doctoral degree in physics. I think it is not an overstatement to emphasize the role of unassuming role models in shaping the career decisions of young students. While I was an undergraduate student, of significance were my encounters with Donna Stokes, Margaret Cheung, and Yuliya Gorb. I believe it was taking a course in ordinary differential equations that cemented my decision to one day become a scientist and a professor. The specific path through high energy physics was due to meeting Rene Bellwied, who happens to be my PhD advisor. I have had a very rich PhD career and I am quite grateful for it. I would also like to thank other members of my PhD dissertation committee —Claudia Ratti, and Ed Hungerford for their insightful comments.

In addition, I would like to thank Anthony Timmins for getting us up to speed with the necessary software packages at the beginning of our graduate studies. Included in the list of ‘us’ are Corey Myers and Surya Pathak. Many thanks to you both for your support and for sharing similar PhD woes with me. Outside the university, I would like to thank Jaki Norohna-Hostler and Barbara Jacak, who, in many ways, and without knowing motivated and encouraged me to complete this dissertation. Also of note is the career guidance given by Christine Nattrass at the final stage of my PhD career. Every individual mentioned helped in getting me to the finish line and onto the next phase of my career. A big thank you to you all!

As for the search for truth, I know from my own painful searching, with its many blind alleys, how hard it is to take a reliable step, be it ever so small, towards the understanding of that which is truly significant.

—Albert Einstein

TABLE OF CONTENTS

ABSTRACT	ii
ACKNOWLEDGMENTS	iv
LIST OF FIGURES	xii
LIST OF TABLES	xiii
1 INTRODUCTION	1
1.1 Properties of quarks	6
1.1.1 Quark spin and charge	6
1.1.2 The color charge	6
1.1.3 Weak isospin	7
1.1.4 The Standard Model	8
1.2 Properties of gluons	10
1.2.1 Gluon color states	10
1.2.2 Screening in QCD	10
1.2.3 Coupling constant in QCD	11
1.2.4 Color confinement	13
1.3 Probes of strongly interacting matter	14
1.3.1 QCD phase diagram	15
1.3.2 Hadronization model and its freeze-out parameters	18
1.3.3 QCD Equation of State (EOS)	21
1.3.4 Lattice QCD (LQCD)	22
1.3.5 Theory meets phenomenological model	24
2 FLUCTUATIONS OF CONSERVED QUANTITIES	25
2.1 Fluctuations of conserved quantities in a thermal system	25
2.1.1 Susceptibilities of conserved quantities from LQCD	26
2.1.2 Chemical freeze-out parameters from LQCD	28
2.2 Fluctuations of conserved quantities in experiment	28
2.2.1 Connecting theory to experiment	30
2.2.2 Experimental limitations and considerations	32
2.3 Dissertation research motivation	34
3 THE ALICE EXPERIMENT AT THE LARGE HADRON COLLIDER	38
3.1 A Large Ion Collider Experiment (ALICE)	39
3.2 ALICE Coordinate System	41
3.3 ALICE Time Projection Chamber (TPC)	42
3.3.1 TPC layout	43
3.3.2 TPC working principle	46
3.3.3 TPC principle of particle identification	47
3.4 V0 particle identification	50
3.5 VZERO Detector	52

3.5.1	Centrality determination	53
3.6	Pseudorapidity density of charged particles	55
4	STATISTICAL DISTRIBUTIONS, ERRORS, AND EXTRANEOUS FLUCTUATIONS	56
4.1	The Poisson distribution	56
4.2	Negative Binomial distribution	57
4.3	Statistical errors	59
4.4	Induced extraneous fluctuations and conservation laws	61
4.4.1	Volume fluctuation effects	61
4.4.2	Conservation laws	63
5	ANALYSIS METHOD	65
5.1	Selections	65
5.1.1	Data and event selection	65
5.1.2	Track selection	66
5.1.3	V0 selection	69
5.2	Λ and $\bar{\Lambda}$ invariant masses	72
5.2.1	Background estimation and signal extraction	73
5.2.2	Raw and background corrected Λ and $\bar{\Lambda}$ multiplicities	75
5.3	Monte Carlo correction factors	76
5.3.1	Feed-down contribution to Λ and $\bar{\Lambda}$	76
5.3.2	Efficiency correction	79
5.3.3	MC closure: a test of efficiency correction procedure	81
5.4	Systematic uncertainties	85
5.4.1	Selection cuts	86
5.4.2	Final systematic uncertainties	88
6	RESULTS, DISCUSSION, AND FUTURE DIRECTIONS	90
6.1	Centrality dependence of the raw Λ , $\bar{\Lambda}$ and net- Λ cumulants	91
6.2	Centrality dependence of the background and feed-down corrected Λ , $\bar{\Lambda}$ and net- Λ cumulants	92
6.3	Centrality dependence of the efficiency corrected Λ , $\bar{\Lambda}$ and net- Λ cumulants	94
6.4	Comparison of Λ , $\bar{\Lambda}$ and net- Λ cumulants to HIJING	96
6.5	Comparison of Λ , $\bar{\Lambda}$ and net- Λ cumulants to net-protons at ALICE	97
6.6	Pseudorapidity dependence of ratio of $\kappa_2(\Lambda - \bar{\Lambda})$ to $\kappa_2(skellam)$	98
6.7	Conclusions and future directions	100
A	APPENDICES	101
A.1	Polynomial fits to Λ and $\bar{\Lambda}$ Invariant masses	101
A.2	Hagedorn fits to Ξ^+ and Ξ^- spectra	101
	BIBLIOGRAPHY	108

LIST OF FIGURES

1.1	A schematic view of the history of the universe. At $t = 0$ the Big Bang goes off. One microseconds (μ_s) later, protons are formed from the quark-gluon plasma. . . .	1
1.2	An illustration of the evolution of heavy-ion collisions. At $\tau = 0$ fm/c (1 fm = 10^{-15} meters, $c = 3 \times 10^8$ meters/seconds), the ions collide. At about 10 fm/c the particles created from the QGP cease all elastic scattering (kinetic freeze-out) before reaching the detector at 10^{15} fm/c. Illustration credit: Chun Shen.	2
1.3	Temperature versus baryon density diagram of the QCD phase structure. The LHC and RHIC experiments explore different areas of the x-axis due to varying collision energy. Figure taken from [2].	3
1.4	Color charge of quarks in baryons and mesons.	7
1.5	Weak decay of the Λ baryon.	8
1.6	Elementary particles of the Standard Model.	9
1.7	The coupling constant, α_s , as a function of energy scale, Q . The solid line, dashed line, and uncertainty band are QCD predictions. (The scale (M_Z) represents the mass of the Z boson). The black dots are the data from CMS obtained from jet measurements with other experimental data from previous measurements at CMS and ZEUS superimposed [12].	12
1.8	An illustration showing the creation of quark-antiquark pair from attempting to split two quarks. The result of attempting to split the two quarks leads to the creation of two mesons. Illustration credit: Flip Tanedo of Quantum Diaries.	13
1.9	Experimental view of the QCD phase diagram. The RHIC Beam Energy Scan probes the different regions of the phase transition in search of a critical point. Chemical freeze-out indicates the cessation of inelastic scattering, while kinetic freeze-out indicates the cessation of elastic scattering.	15
1.10	State of matter during the evolution of the collision process. The collision overlap zone represents the initial collision. The confined hot matter reaches thermalization in the next stage. This is followed by expansion and cooling of the deconfined matter, which in turn reaches chemical, and kinetic freeze-out before hitting the detector. . .	18
1.11	Energy dependence of the thermal parameters: T and μ_B . The red square boxes are the yields from data. The data are from mid-rapidity, $y = 0$ (where all the particles are emitted in the transverse direction). Rapidity is a measure of energy and longitudinal momentum ($y = 1/2 \ln[(E + P_L)/(E - P_L)]$). Figure taken from [34].	19
1.12	Phase diagram of strongly interacting matter. The points represents the thermal fits of hadron yields at various collision energies [35] [36] [37].	20
1.13	The speed of sound squared from lattice QCD (HISQ and stout) and the HRG model versus temperature. The vertical band marks the crossover region, $T_c = (154 \pm 9)$ MeV. The horizontal line to the top right corresponds to the ideal gas limit. Figure taken from [38].	24

2.1	BNL-Bielefeld-CCNU collaboration results of baryon number susceptibility: χ_2^B (left) and $\frac{\chi_4^B}{\chi_2^B}$ (right) as a function of temperature computed from LQCD at $\mu_B = 0$ [39]. $N_\tau = 1/aT$ are the inverse lattice spacings and the horizontal line on the left plot is the value for a non-interacting gas. The continuum extrapolated results are for lattice spacing, a , extrapolated to $a = 0$. The yellow vertical band on the right plot marks the phase crossover region, $T_c = (154 \pm 9)$ MeV.	27
2.2	Comparison of lattice results with STAR data [43].	31
2.3	Thermal fits of the integrated hadron yields in Pb-Pb collisions at $\sqrt{s_{NN}} = 2.76$ TeV measured at ALICE. Figure taken from [44].	35
2.4	Continuum extrapolated lattice calculations on flavor specific susceptibilities. Left figure shows a comparison of the second order susceptibility of the light quark, χ_2^u , to the second order susceptibility of the strange quark, χ_2^s . Right plot shows a comparison of the ratio of the fourth order to second order susceptibilities for light and strange quarks $\frac{\chi_4}{\chi_2}$. Results are also shown for the respective HRG predictions. Figure taken from [45].	36
2.5	Predictions of net- Λ FO surface based on comparison of net- Λ cumulant ratios from the STAR experiment to HRG kaon and charge/proton FO. Figure taken from [46].	37
3.1	CERN accelerator complex.	38
3.2	The ALICE experiment. Figure taken from [48].	40
3.3	A description of ALICE coordinate system axis, angles and detector sides. Figure taken from [52].	41
3.4	Transverse momentum resolution in the central rapidity region ($ \eta < 0.8$) for TPC tracks combined with hits in the ALICE Inner Tracking System (ITS). Figure taken from [50].	42
3.5	3D view of the Time Projection Chamber. Figure taken from [54].	43
3.6	Charge particle track drifting to readout. Figure taken from [57].	46
3.7	Values of ionization in argon at normal density (relative to $\beta\gamma \approx 4$). Note, $\beta\gamma = P/\mu c$, where $\beta = v/c, \gamma = (1 - \beta^2)^{-1/2}, \mu, P =$ mass, momentum of the particle respectively. The data are the points from Lehraus et al (1978), and the dashed line are model predictions from Sternheimer. The solid line is the most probable energy loss in 4.5 cm of pure argon with the PAI model. Figure taken from [58].	48
3.8	Specific ionization energy loss of the negative tracks in the TPC as a function of rigidity in Pb-Pb collisions at $\sqrt{s_{NN}} = 5.02$ TeV. The dashed lines are the parameterization of the Bethe-Bloch function. The inset shows the mass of ${}^3\overline{He}$ and ${}^4\overline{He}$ after combining TPC and time-of-flight (TOF) measurements. Figure taken from [55].	49
3.9	A schematic of the Λ decay topology and its Distance of Closest Approach (DCA) choices.	51
3.10	A schematic of the VZERO detectors and their distances from the interaction point.	52
3.11	A schematic of the two Lorentz contracted ions before and after the collision. The degree of overlap is the impact parameter, b . Figure taken from [60].	53
3.12	Distribution of the sum of the amplitudes in the VZERO scintillators with NBD-Glauber fit shown as the red line. The centrality classes are within the vertical lines. The insert is the distribution for the more peripheral centralities. The ratio plot is the ratio of the NBD-Glauber fit to the data. Figure taken from [61].	54

4.1	Poisson probability distributions as a function of the number of occurrences. λ is the mean number of occurrences, which is also equal to the variance.	57
4.2	Comparison of Poisson and Negative Binomial distributions both centered at 20. The sample size of the left plot is small so the NBD (black line) is more spread out than the Poisson (red line). As the sample size gets larger, the NBD converges on the Poisson (as seen in the right plot).	58
4.3	Error estimation on κ_n with subsampling method. Note that κ_n and C_n are used interchangeably throughout this dissertation. Shown here are error estimates of the mean (left) and variance (right) of the raw net- Λ multiplicity distribution.	60
4.4	Centrality bin width correction (CBWC) of raw C_n of the net- Λ multiplicity distribution. Shown here are with and without CBWC of C_2 (left) and C_3 (right).	62
4.5	Net-protons measured at ALICE compared to models incorporating baryon number conservation. The left panel shows the normalized values of κ_2 of net-baryons for different values of Δy_{corr} , where $\Delta y_{corr} = 2 y_B - y_{\bar{B}} $. The right panel is the model plotted on the ALICE net-proton fluctuation measurement. Figure taken from [68].	63
5.1	Distribution of the vertex Z position with vertex cut at $ z < 10$ cm (left). Centrality distribution of the selected events (right).	66
5.2	TPC dE/dx as a function of momentum in Pb-Pb collisions for the positive (left) and negative (right) tracks.	67
5.3	Number of positive (left) and negative (right) daughter track crossed rows from the TPC as function of daughter track transverse momentum. The horizontal dashed line indicates a selection for greater than 80 track clusters.	68
5.4	TPC dE/dx selection of $ n\sigma < 3$ on daughter tracks for Λ (p and π^-) and for $\bar{\Lambda}$ (\bar{p} and π^+).	68
5.5	Cosine of pointing angle selection of > 0.99 for Λ (left) and $\bar{\Lambda}$ (right).	69
5.6	The V0 radius versus Λ (left) and $\bar{\Lambda}$ (right) invariant mass. A selection of greater than 5 cm is chosen to reconstruct the Λ and $\bar{\Lambda}$ candidates.	70
5.7	Distance of closest approach of the V0 to the primary vertex versus Λ (left) and $\bar{\Lambda}$ (right) invariant mass. A selection of less than 0.25 cm is chosen to reconstruct the Λ and $\bar{\Lambda}$ candidates.	70
5.8	Distance of closest approach of the V0 daughters versus Λ (top figure) and $\bar{\Lambda}$ (bottom figure) invariant mass. A selection of less than 0.8σ is chosen to reconstruct the Λ and $\bar{\Lambda}$ candidates.	71
5.9	Pseudorapidity coverage as a function of invariant mass of Λ (left) and $\bar{\Lambda}$ (right) after track and V0 selections (found in tables 5.1 and 5.2).	72
5.10	Λ (left) and $\bar{\Lambda}$ (right) invariant mass distributions in $1.5 < p_T < 1.6$ [GeV/c] and 0-10 % centrality class.	72
5.11	Linear fits to Λ (left) and $\bar{\Lambda}$ (right) invariant mass distributions in $1.5 < p_T < 1.6$ [GeV/c] and 0-10 % centrality class.	73
5.12	Λ (left) and $\bar{\Lambda}$ (right) background fraction versus p_T in 10% centrality classes for 0-80%.	74
5.13	Λ , $\bar{\Lambda}$, and Λ - $\bar{\Lambda}$ multiplicities before and after background correction. Plotted are the counts per event in 0-10% centrality class.	75
5.14	Feed-down matrices for Λ and $\bar{\Lambda}$. Left panel: feed-down to Λ includes Ξ^- and Ξ^0 (in numerator). Right panel: feed-down to $\bar{\Lambda}$ includes Ξ^+ and Ξ^0 (in numerator).	77

5.15	Feed-down contribution to Λ and $\bar{\Lambda}$. Left panel: in red is the number of secondary Λ and in blue is the number of all reconstructed Λ (top left figure) in 0-10% centrality class. The bottom figure is the same relationship for $\bar{\Lambda}$. Right panel: the fraction of secondaries for Λ (top right figure) and $\bar{\Lambda}$ (bottom right figure) in all centrality classes.	78
5.16	Reconstruction efficiencies for Λ (left) and $\bar{\Lambda}$ (right).	79
5.17	Efficiency factors specific for the Λ and $\bar{\Lambda}$ cumulants, κ_n	80
5.18	Invariant mass of Λ (left) and $\bar{\Lambda}$ (right) from Monte Carlo HIJING in 0-10% centrality class fitted with a polynomial of degree 1 to estimate the background.	81
5.19	HIJING reconstructed Λ (left) and $\bar{\Lambda}$ (right) background fraction, B_{frac} , in all centrality classes. Not shown is the 70-80% class, which had very little entries to fit.	82
5.20	Secondaries contribution to reconstructed level Λ (left) and $\bar{\Lambda}$ (right) from Monte Carlo HIJING.	83
5.21	Monte Carlo Closure test for the mean (top figure) and variance (bottom figure) of the net- Λ cumulants from HIJING MC event generator.	84
5.22	Plots of the cumulants based on the selection cuts of table 5.5 (top panel) and their comparison to the default values in the ratio plot (bottom panel).	87
5.23	Summary of the contributions to the systematic uncertainty to the cumulants for 0-10% centrality class.	88
5.24	Systematic uncertainties in 0-10% centrality class for $\kappa_2(\Lambda - \bar{\Lambda})$ and $\kappa_2(skellam)$ in $ \eta < 0.3$ (top figure) and $ \eta < 0.8$ (bottom figure).	89
6.1	Centrality dependence of the first two raw cumulants of Λ , $\bar{\Lambda}$ and net- Λ distribution. The ratio plot is a comparison of the variance of the net- Λ distribution (red circles) to a Poisson distribution —Skellam (black boxes). The Skellam is a sum of the Λ and $\bar{\Lambda}$ distributions. The single first and second moments are the orange and blue points respectively.	91
6.2	Centrality dependence of the first two cumulants of Λ , $\bar{\Lambda}$ and net- Λ distribution corrected for background and feed-down. The ratio of $\kappa_2(\Lambda - \bar{\Lambda})$ to $\kappa_2(Skellam)$ approaches unity in all centrality classes after correction for background and weak decays.	93
6.3	Experimentally measured first and second cumulants of the Λ , $\bar{\Lambda}$ and net- Λ distributions corrected for efficiency. The bottom panel is the corresponding ratio of the net- Λ second cumulant to the Skellam baseline.	94
6.4	Experimentally measured first and second cumulants of the Λ , $\bar{\Lambda}$ and net- Λ distributions compared to HIJING MC generated events. The lines are the corresponding cumulants from HIJING. Note that the single first moments and second moments from HIJING closely converge.	96
6.5	Experimentally measured first and second cumulants of the Λ , $\bar{\Lambda}$ and net- Λ distributions compared to measured p, \bar{p} and net-p cumulants from ALICE. The net-proton results plot is taken from [70].	97

6.6	The pseudorapidity dependence of the second cumulant of net- Λ fluctuation measurement (top panel) and the ratio to Skellam baseline (bottom panel) in 0-10% centrality class. The ratio is compared to expectation from a model incorporating effects of global baryon number conservation (red dashed line) and to HIJING MC generator (dashed black line).	98
A.1	Background estimation from linear fits to Λ invariant masses within p_T range: [1.0 - 2.0 GeV/c].	102
A.2	Background estimation from linear fits to Λ invariant masses within p_T range: [2.0 - 4.0 GeV/c].	103
A.3	Background estimation from linear fits to $\bar{\Lambda}$ invariant masses within p_T range: [1.0 - 2.0 GeV/c].	104
A.4	Background estimation from linear fits to $\bar{\Lambda}$ invariant masses within p_T range: [2.0 - 4.0 GeV/c].	105
A.5	Ξ^- spectra measured in $\sqrt{s_{NN}} = 5.02$ TeV Pb-Pb collisions with the Hagedorn fits in green to smooth out the spectra. The counts of Ξ^- are used to estimate the feed-down to Λ	106
A.6	Ξ^+ spectra measured in $\sqrt{s_{NN}} = 5.02$ TeV Pb-Pb collisions with the Hagedorn fits in green to smooth out the spectra. The counts of Ξ^+ are used to estimate the feed-down to $\bar{\Lambda}$	107

LIST OF TABLES

1.1	Quark flavor and weak isospin.	8
3.1	Time Projection Chamber parameters. Table adapted from [53].	45
3.2	A description of topological variables for Λ and $\bar{\Lambda}$ reconstruction.	51
3.3	Centrality classes from $dN_{ch}/d\eta$ measured in Pb-Pb collisions at $\sqrt{s_{NN}} = 5.02$ TeV at $\eta < 0.5$. $\langle N_{part} \rangle$ is obtained with the Glauber model. Table adapted from [62].	55
5.1	A summary of daughter tracks selection for Λ and $\bar{\Lambda}$	67
5.2	Topological selections for Λ and $\bar{\Lambda}$ reconstruction.	69
5.3	Background (B) counts per centrality class within signal range (B+S) for Λ and $\bar{\Lambda}$ in $1.11 < \text{inv. mass} < 1.122$ [GeV/ c^2] and $1.0 < p_T < 4.0$ [GeV/ c].	74
5.4	Λ and $\bar{\Lambda}$ selection criteria for systematic uncertainty estimation.	85
5.5	Explicit description of the total cut variations for Λ and $\bar{\Lambda}$ used to estimate systematic uncertainties in the cumulants.	85
5.6	Relative uncertainties on the cumulants due to the different selections. The results are for 0-10% centrality class, $1 < p_T < 4$ GeV/ c , and $ \eta < 0.5$	87

1 Introduction

What if you could go back in time and perhaps see when you were born? Why not even further back in time to when your parents were born and even their parents? How about fast rewinding to one microsecond after the Big Bang? What will you see? The answer is nothing, because the cells that make up your eyes (and body) that consist of ordinary matter have not yet formed. One micro second after the Big Bang, the universe would have been in a state of a quark-gluon plasma—a very hot and dense ‘soup’ of asymptotically free quarks and gluons. It is from the cooling and expansion of this quark-gluon plasma that nuclear matter observed today emerged. A pictorial description of this process can be viewed in fig. 1.1.

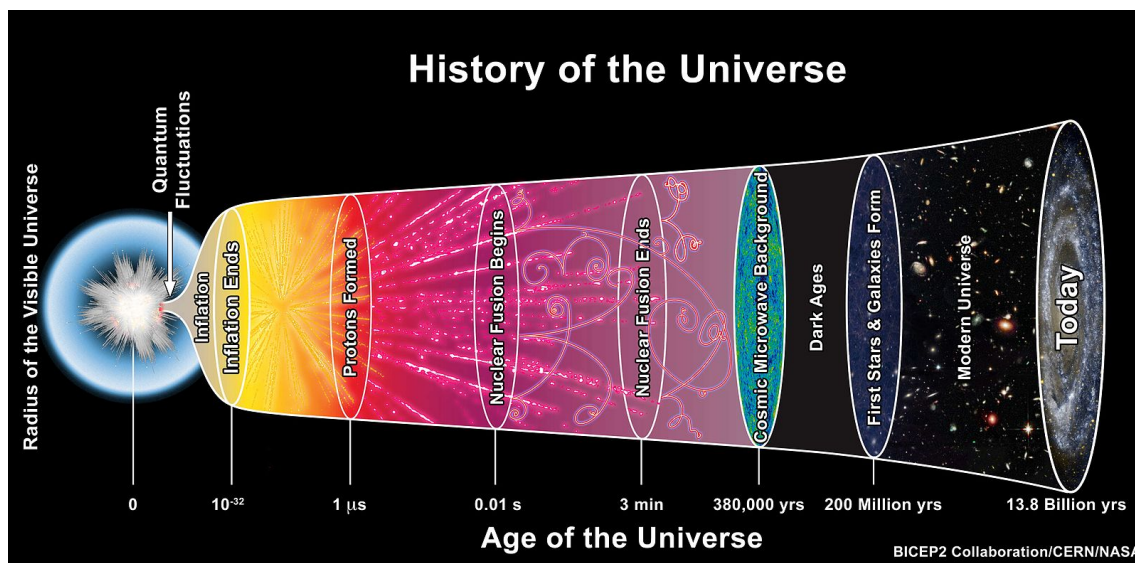


Figure 1.1: A schematic view of the history of the universe. At $t = 0$ the Big Bang goes off. One microsecond (μs) later, protons are formed from the quark-gluon plasma.

As the quark-gluon plasma (QGP) is no longer present in nature (though, there are some speculations that it may be found in the core of neutron stars), the only way to study it is through relativistic heavy-ion collisions or “Little Bangs”. Before the heavy ions collide, they are accelerated to speeds almost equal to the speed of light. At high densities and/or temperatures, the QGP is formed, which cools to form hadrons, (a process known as hadronization) before hitting the detector.

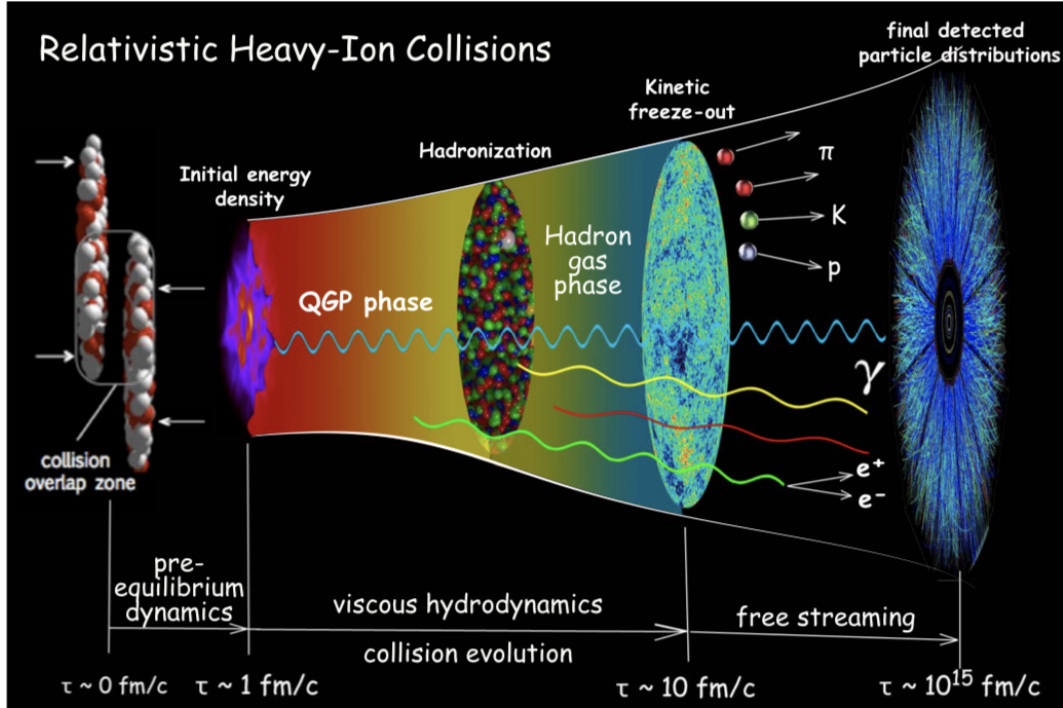


Figure 1.2: An illustration of the evolution of heavy-ion collisions. At $\tau = 0 \text{ fm}/c$ ($1 \text{ fm} = 10^{-15}$ meters, $c = 3 \times 10^8$ meters/seconds), the ions collide. At about $10 \text{ fm}/c$ the particles created from the QGP cease all elastic scattering (kinetic freeze-out) before reaching the detector at $10^{15} \text{ fm}/c$. Illustration credit: Chun Shen.

A schematic of this process is shown in fig. 1.2.

The creation of the quark-gluon plasma in a heavy-ion collision experiment was first reported at the Relativistic Heavy Ion Collider (RHIC) in 2005 [1]. The creation of this plasma fascinates particle and nuclear physicists till this day. While some research groups focus on its phase structure, others focus on studying its properties. These properties can range from studying how the plasma flows—that is, its shear viscosity to entropy density ratio and azimuthal asymmetry of particle yields, to how energetic partons (or jets) are affected as they propagate through the colored medium (the QGP). The QGP is referred to as a colored medium because the quarks and gluons of which it consists carry a color charge. The color charge is analogous to the electric charge. A distinction, however, is that the force in question is the strong force, not the electromagnetic force.

The theory that governs the interaction of quarks and gluons is quantum chromodynamics

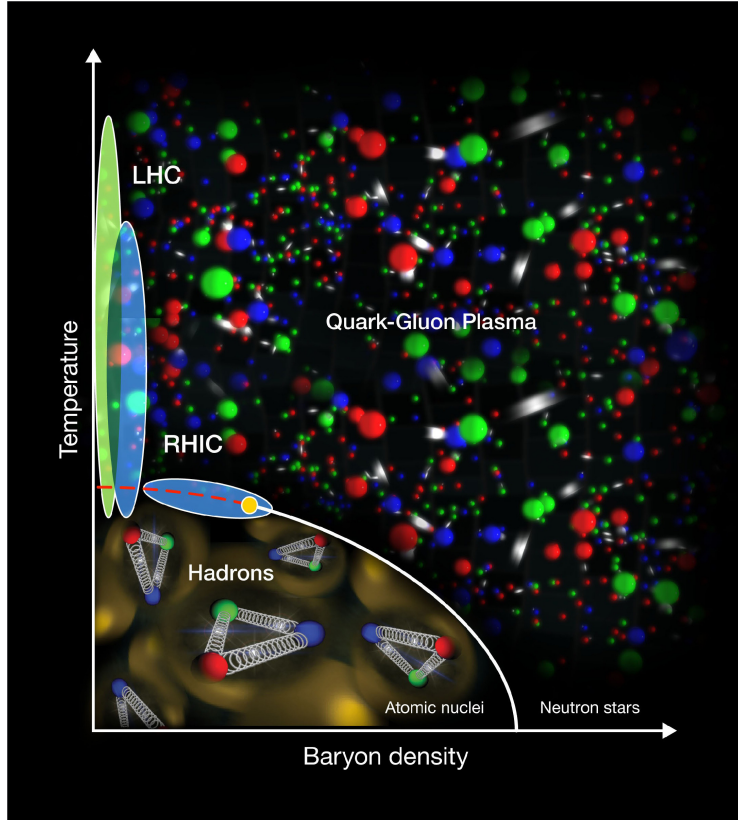


Figure 1.3: Temperature versus baryon density diagram of the QCD phase structure. The LHC and RHIC experiments explore different areas of the x-axis due to varying collision energy. Figure taken from [2].

(QCD) [4]. The usefulness of QCD is not only limited to degrees of freedom of the quarks and gluons, it also extends to the description of the mass spectrum of hadrons (e.g. protons, neutrons, pions ...) and deep-inelastic processes [5]. The thermodynamic parameters of QCD are its temperature, T , and its baryon chemical potential, μ_B . Armed with lattice QCD (LQCD), a well established non-perturbative approach to solving the QCD theory of quarks and gluons [6], and model calculations, one can define a space with these thermodynamic parameters (T and μ_B) to create the QCD phase diagram, which depicts a transition from asymptotically free quarks and gluons at high temperatures and/or densities into hadronic matter. An illustration of the phase transition in strongly interacting matter is shown in fig. 1.3. It is merely a schematic because the values of T and μ_B

where a phase transition occurs from quarks and gluons into hadrons is not well known. The phase structure of strongly interacting matter is, in fact, the focus of this dissertation. Phase transitions in strongly interacting matter can be explored by studying the response of the thermalized system to external perturbations, which are calculated using the thermodynamic susceptibility. By studying the thermodynamic susceptibilities, the fluctuation of conserved quantities can be extracted. There is a direct link between the thermodynamic susceptibilities of conserved quantities and net-particle fluctuation measurements. Experimentally, the conserved quantities (net-charge, net-baryon, and net-strangeness number) are calculated using net-particle species (multiplicities) created in the collision. For net-baryon number, the net-protons are used. Similarly, the net-pions and net-kaons are used for the net-charge and net-strangeness quantum numbers respectively. These choices of net-particle multiplicities are proxies for net-conserved quantities. Thus, in experiment, the complete net-conserved quantity is not recovered, given that the net-protons are not the only net-baryons produced in the collision. Neither are the net-kaons the sole net-strange particles produced in the collision. The current choice of proxies are convenient because they are charged, which allows for easy tracking and they are produced in larger proportion in the collision, making their use for net-particle fluctuation measurements, a statistics hungry measurement, possible.

Notwithstanding, one can extend the study of the phase structure of strongly interacting matter via net-particle multiplicity fluctuation measurements to include the event-by-event net-lambda distribution extracted from the ALICE detector at the LHC. Although weakly decaying and neutrally charged, it can be reconstructed via its charged daughters (protons and pions). Due to the fact that the lambda particle is a strange baryon, its fluctuation measurement provides a more complete picture of the study of the conserved quantities: net-strangeness and net-baryon number. There are other questions to be tackled with the study of net-lambda fluctuation measurement. These include whether the chemical freeze-out parameters of the net-lambda are different from that of the net-proton when compared separately, and in addition, the correlation between strangeness and baryon number. The question is: does the lambda particle prefer to behave like a baryon or like a strange particle, or both?

Before diving deeply into the details surrounding net-particle fluctuation measurements in heavy-ion collision experiments (this is saved for chapter 2), the theoretical framework upon which the phenomena under study is established, as well as a thermalization model that can be exploited to study the phase structure of strongly interacting matter are discussed. Therefore, the remainder of this chapter will describe the elementary particles and the forces that govern them, and attempt to make a case for a phenomenological model that has been successful in describing the phase structure of strongly interacting matter. Good agreement has been observed in the results from the model, theory, and net-particle fluctuation measurements of the data in different regimes of the QCD phase diagram. This supports the validity of net-particle fluctuation measurements as a useful probe of the QCD phase diagram.

Chapter 3 covers details of the ALICE experiment and its subdetectors. Statistical distributions that can be used to characterize event-by-event net-particle multiplicity distributions and the effect of trivial fluctuations that can mask the true fluctuation measurements are covered in chapter 4. The analysis method is presented in chapter 5, while the results and conclusions are presented in chapter 6.

1.1 Properties of quarks

Quarks are elementary particles that make up what were thought as fundamental particles, i.e., protons and neutrons. Through deep inelastic scattering experiments at the Stanford Linear Accelerator Center (SLAC), the proton was found to consist of point-like internal structures, namely quarks and gluons [7]. If a particle consists of three valence quarks (for example, the proton), it is called a baryon; whereas particles with a valence quark-antiquark pair (e.g. the π^+ particle) are called mesons. Collectively, baryons and mesons are called hadrons. There are six flavors (or types) of quarks —up, down, strange, charm, top and bottom; and they individually contain intrinsic properties such as: electric charge, mass, color charge, spin, and weak isospin.

1.1.1 Quark spin and charge

A particle's spin is its intrinsic angular momentum. Not unlike the proton, the quarks are fermions —obeying the Pauli exclusion principle, which states that two identical fermions are prohibited from occupying the same quantum state at the same time. However, unlike the proton, quarks come in fractional electric charge. There are two types (or flavors) of quarks that make up the proton —up and down quarks. Given that the proton is a baryon, it must, as a result, be made of three quarks. The proton has an electric charge of (+1); whereas the up and down quarks have an electric charge of $(+\frac{2}{3})$ and $(-\frac{1}{3})$ respectively. It is therefore intuitive to infer that the third quark within the proton is the up quark —to make a combined electric charge of (+1).

1.1.2 The color charge

As briefly mentioned in the previous section, the color charge is an analog to the electric charge in the electromagnetic force. The creation of this additional charge was necessary because of the Pauli exclusion principle, which prohibits more than one quark from occupying the same quantum state at the same time. An example is the Delta resonance (Δ^{++}), which contains three up quarks uuu . It is known that such a particle exists, and because quarks are fermions they cannot be in the same quantum state. Thus, a new charge (the color charge) was created to account for this. A

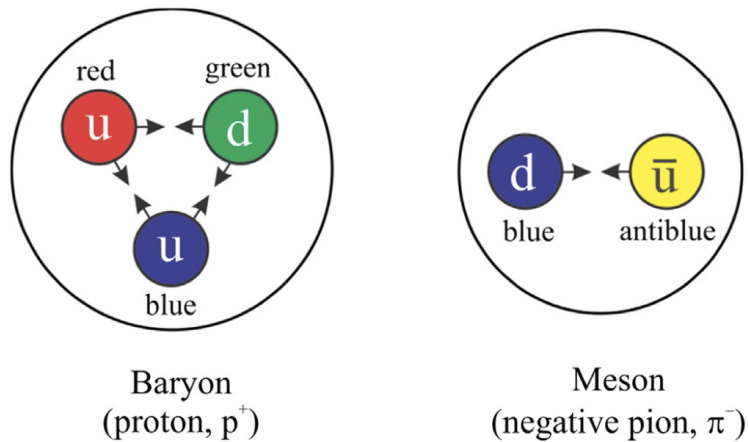


Figure 1.4: Color charge of quarks in baryons and mesons.

quark can have three different color quantum states, namely: red, blue, and green (see fig. 1.4). Similarly, the anti-quarks can have three different anti-color quantum states —anti-red, anti-blue, and anti-green. A combination of all three color charges within a baryon, makes the baryon ‘color neutral’. Whereas, the mesons becomes color neutral by having a color and anti-color quark pair.

1.1.3 Weak isospin

Quarks are capable of changing flavors via weak interactions (one of the fundamental forces in nature). This type of decay is described through the weak isospin quantum number $-T_3$. Table 1.1 shows a list of the quark flavors and their associated weak isospin quantum number. Quark types with different T_3 signs can transform into one another. When the transformation occurs, the quark emits or absorbs the W^\pm boson (a weak force mediator), which results in a change in flavor. As an example, as shown in fig. 1.5, the Λ -particle with quark content: uds , decays into two particles: p^+ and π^- with quark contents: uud and $\bar{u}d$ respectively. This occurs because the decay process allows for the emission of a W^- boson from the s quark, which changes its flavor from s to u . Furthermore, the emitted W^- boson decays into a $\bar{u}d$ quark pair, which forms the π^- .

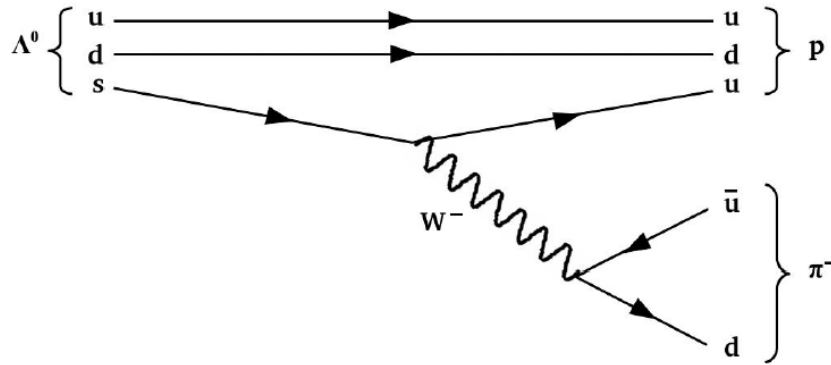


Figure 1.5: Weak decay of the Λ baryon.

Quark Flavor	Symbol	Weak Isospin (T_3)
up	u	$+\frac{1}{2}$
down	d	$-\frac{1}{2}$
strange	s	$-\frac{1}{2}$
charm	c	$+\frac{1}{2}$
bottom	b	$-\frac{1}{2}$
top	t	$+\frac{1}{2}$

Table 1.1: Quark flavor and weak isospin.

1.1.4 The Standard Model

The standard model lists the six types of quarks, their corresponding electric charges, masses, and force carrier, the gluon. Also listed are the leptons and the other force carriers. Fig. 1.6 shows a schematic of the standard model—a kind of periodic table of the elements for particle physics.

The leptons are the electron, muon, tau and their corresponding neutrinos. The four fundamental forces are the strong force, electromagnetic force, the weak force, and gravitational force, which are mediated by the gluon, photon, W^\pm and Z^0 bosons, and the graviton (not shown) respectively.

With respect to the quarks, one can describe the standard model as a list of quark flavors and the forces they interact with. This is the case because the quarks have mass, hence they are influenced by gravity. They have electric charge, color charge, and weak isospin, hence they are influenced by the electromagnetic, strong, and weak forces, respectively.

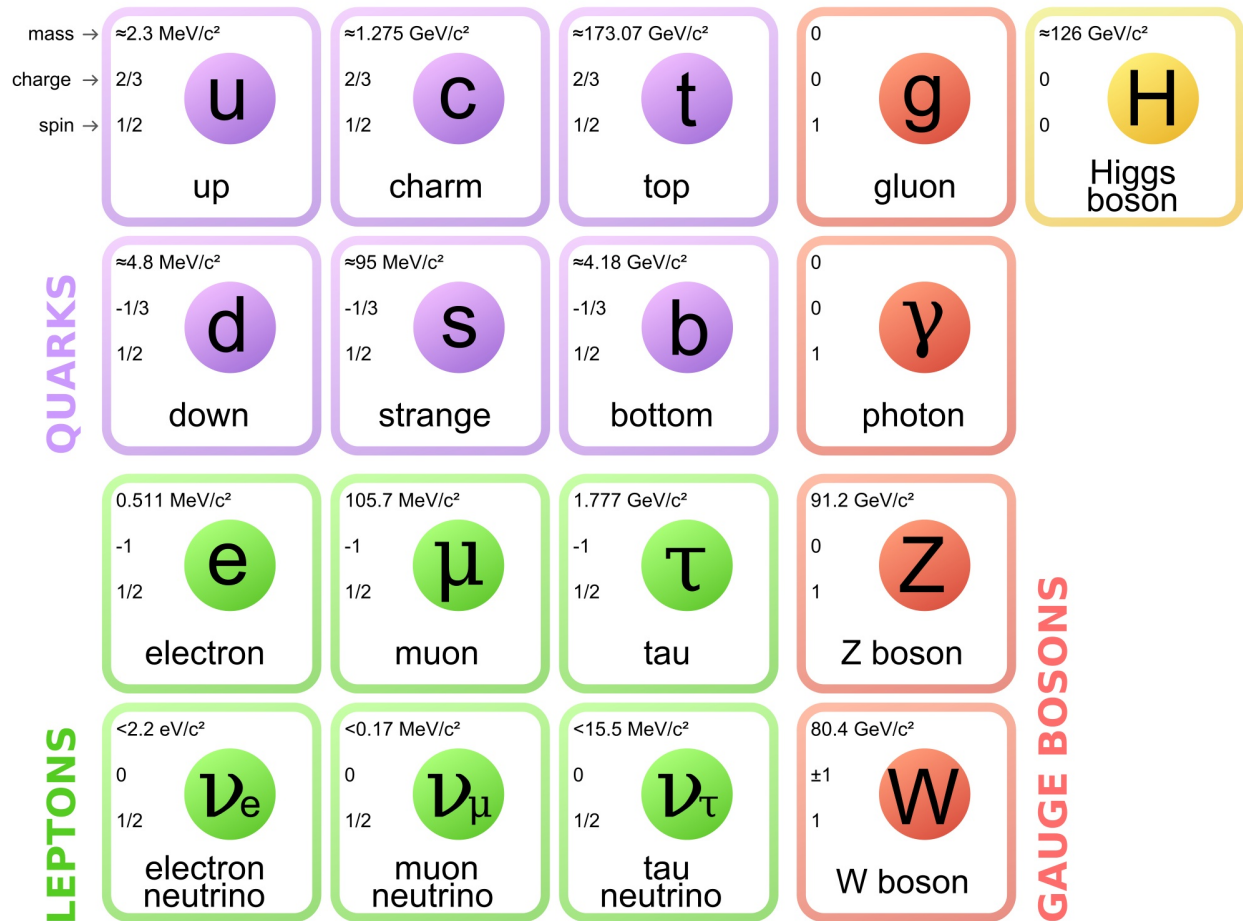


Figure 1.6: Elementary particles of the Standard Model.

1.2 Properties of gluons

The gluons act as exchange particles for the strong force that holds quarks together. One could think of the gluons as objects that ‘glue’ quarks together to form hadrons. Apart from carrying a color charge, the gluons exhibit screening, color confinement, and asymptotic freedom. Details of these phenomena are discussed in the following sections.

1.2.1 Gluon color states

Gluons carry color charge, and as a result, also participate in strong interactions. As mentioned in previous sections, there are 3 color states and 3 anticolor states, namely —red, green, blue, and anti-red, anti-green, anti-blue; with corresponding symbols: r, g, b , and $\bar{r}, \bar{g}, \bar{b}$. It may be intuitive to assume that there are 9 color states of color and anti-color in gluons, however, there are only 8 independent color states. This is the case because long-range gluon interactions do not exist —that is, only color neutral (or color singlet) states can interact with one another, and only colored states can interact with each other. In other words, the color singlet state: $(r\bar{r} + b\bar{b} + g\bar{g})/\sqrt{3}$ for color and anti-color gluons does not exist.

1.2.2 Screening in QCD

Screening is a qualitative idea that describes the action of a field on virtual particles carrying relevant charge. In QED (quantum electrodynamics), virtual charged particle-antiparticle pairs (e^+e^-), are created in the vacuum from a single electron in propagation. The e^+e^- pair is associated with a loop carrying an electric field pointed in opposite direction of its parent electron’s electric field. The result is a smaller net field. The idea of screening is used to explain the fall off of charge at greater distances —that is, to avoid the so-called “zero-charge problem” associated with QED. In QCD however, a similar vacuum polarization effect exists, though the charge in play here is the color charge. Also different is that the virtual gluon color charge can be associated with a color field parallel to its parent quark’s color field. This leads to antiscreening, which enhances the field rather than diminishing it.

1.2.3 Coupling constant in QCD

The strong interaction equivalent to the fine-structure constant in electrodynamics, $\alpha = \frac{1}{137}$, that characterizes the strength of the coupling of an elementary charged particle with the electric field is the strong coupling constant, α_s . The strong coupling constant is the fundamental coupling underlying the interactions of quarks and gluons in QCD. Due to screening and anti-screening, the strong coupling constant varies in strength with the momentum transfer. The scale of the interaction is related to the four momentum transfer, Q , such that, the effective α_s can be expressed in terms of Q as:

$$Q^2 \frac{\partial \alpha_s}{\partial Q^2} = \beta(\alpha_s) = - \left(\frac{\alpha_s}{4\pi} \right)^2 \sum_{n=0} \left(\frac{\alpha_s}{4\pi} \right)^n \beta_n \quad (1)$$

Eq. 1 shows the scale dependence of the strong coupling constant expressed as perturbative series and controlled by the β - function with first terms [8] [9] [10]:

$$\beta_0 = 11 - \frac{2}{3}n_f \quad (2)$$

$$\beta_1 = 102 - \frac{38}{3}n_f \quad (3)$$

The exact analytic solution to Eq. 1 is known to β_0 order only. At β_0 order its solution is [11]:

$$\frac{Q^2}{\alpha_s} \frac{\partial \alpha_s}{\partial Q^2} = -\frac{1}{4\pi} \beta_0 \quad (4)$$

Rearranging:

$$-\frac{4\pi d\alpha_s}{\beta_0 \alpha_s^2} = \frac{dQ^2}{Q^2} \quad (5)$$

Integrating between Q^2 and μ_0^2 , (where μ_0 is an arbitrary scale):

$$\frac{4\pi}{\alpha_s(\mu_0^2)} - \frac{4\pi}{\alpha_s(Q^2)} = \beta_0 \ln \left(\frac{\mu_0^2}{Q^2} \right) \quad (6)$$

One can define a QCD scale parameter, $\Lambda_{QCD} \approx 200\text{MeV}$, such that:

$$\Lambda_{QCD}^2 \equiv \mu^2 e^{-\frac{4\pi}{\beta_0 \alpha_s(\mu^2)}} \quad (7)$$

which yields:

$$\alpha_s(Q^2) = \frac{4\pi}{\beta_0 \ln(Q^2/\Lambda_{QCD}^2)} \quad (8)$$

From Eq. 8, the relationship between the coupling and momentum transfer is an inverse one, such that at large momentum transfers, the coupling is small. As a result, at short distances the interaction is weaker. In this domain, the interaction is exhibiting “asymptotic freedom”. This has been experimentally verified at the Compact Muon Solenoid (CMS) experiment at the LHC. Fig. 1.7 shows measurements of the coupling constant at varying energy scales.

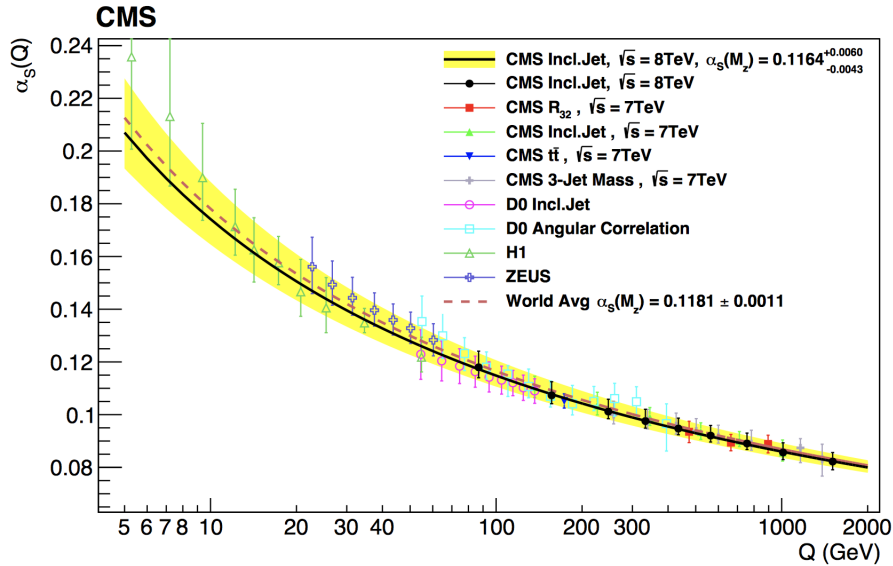


Figure 1.7: The coupling constant, α_s , as a function of energy scale, Q . The solid line, dashed line, and uncertainty band are QCD predictions. (The scale (M_Z) represents the mass of the Z boson). The black dots are the data from CMS obtained from jet measurements with other experimental data from previous measurements at CMS and ZEUS superimposed [12].

1.2.4 Color confinement

Due to the fact that gluons carry a color charge, they self interact, and thus contribute to the coupling. As a result, anti-screening of the color charge results in increased strength of the coupling constant between two colored objects as they are pulled apart. This may be the reason why quarks and gluons are bound within hadrons. Unlike QED where the electric field between two electrically charged objects decreases as they are pulled apart, two color charged objects in QCD will gain a constant force (at large distances) due to a string that is created between the two colored objects as they are pulled apart [13]. The attempt to separate the two colored objects from each other will instead lead to the formation of quark-antiquark pair (as shown in fig. 1.8).

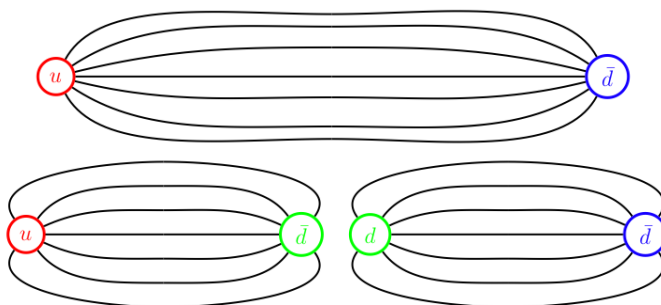


Figure 1.8: An illustration showing the creation of quark-antiquark pair from attempting to split two quarks. The result of attempting to split the two quarks leads to the creation of two mesons. Illustration credit: Flip Tanedo of Quantum Diaries.

The result of color confinement is due to nature of the QCD potential. At large distances, the potential increases with distance, while at small distances the potential decreases with distance. Written explicitly, the strong potential is:

$$V_s(r) \propto -\frac{4}{3} \frac{\alpha_s}{r} + kr \quad (9)$$

There also exists a phenomenon called “deconfinement”. In the formation of a quark-gluon plasma in heavy-ion collisions where asymptotic freedom exists, the force between two colored objects is screened by polarized charges between them —a process known as “Debye screening”. As a result,

the coupling becomes weaker, so that at short distances, the strong potential takes the form:

$$V_s(r) \propto -\frac{\alpha_s}{r} e^{-r/\lambda_D} \quad (10)$$

Where, λ_D is the screening length and r is the distance between the quarks in question. As a specific example, J/ψ is a meson formed from charm quark and anti-quark, $c\bar{c}$. One of the ways to test for the creation of the quark-gluon plasma (QGP) in heavy-ion collisions is through the suppression of J/ψ . This can be achieved by knowing that if the Bohr radius of J/ψ is larger than the screening length, λ_D , the charm quark and anti-quark will melt into the rest of the medium (QGP). This means the charm quark and anti-quark are now free to interact with other quarks in the medium and likely pair up with light quarks: $\bar{u}\bar{d}$, to form $c\bar{u}$ and $c\bar{d}$ pairs —thus, leading to a reduction or suppression of J/ψ .

1.3 Probes of strongly interacting matter

This section covers a phenomenological and theoretical approach used to map the QCD phase diagram. By mapping, the intention is to state that the values of the temperature and baryon chemical potential when matter transitions from a state of deconfined quarks and gluons into confined hadronic matter is not very well known. The approaches include a thermal fit of the yields produced in heavy-ion collisions with a statistical hadronization model and the calculation of the equation of state of QCD to extract generalized susceptibilities. Both procedures extract the chemical freeze-out parameters: T and μ_B of the QCD phase diagram. However, they both have their limitations and are restricted to different degrees of freedom. On the one hand, the thermalization models are associated with hadron degrees of freedom, and on the other hand, the lattice QCD (LQCD) calculations are associated with quarks and gluons degrees of freedom. More details on the two approaches are provided in the remainder of this section. However, a brief description of the behavior of matter in the different regimes of the QCD phase diagram will precede a description of the two approaches.

1.3.1 QCD phase diagram

Before the discovery of QCD and its properties such as asymptotic freedom, a temperature limit for hadronic matter had already been predicted by Hagedorn via a statistical bootstrap model with $T \simeq 170$ MeV [14]. Moreover, the existence of asymptotic freedom in QCD implied the existence of a new high temperature phase of weakly interacting quarks and gluons, i.e., the QGP [15]. Already, two distinct regimes (quark gluon plasma and hadronic matter) can be identified (as seen in fig. 1.9) through discoveries in QCD and the statistical hadronization model.

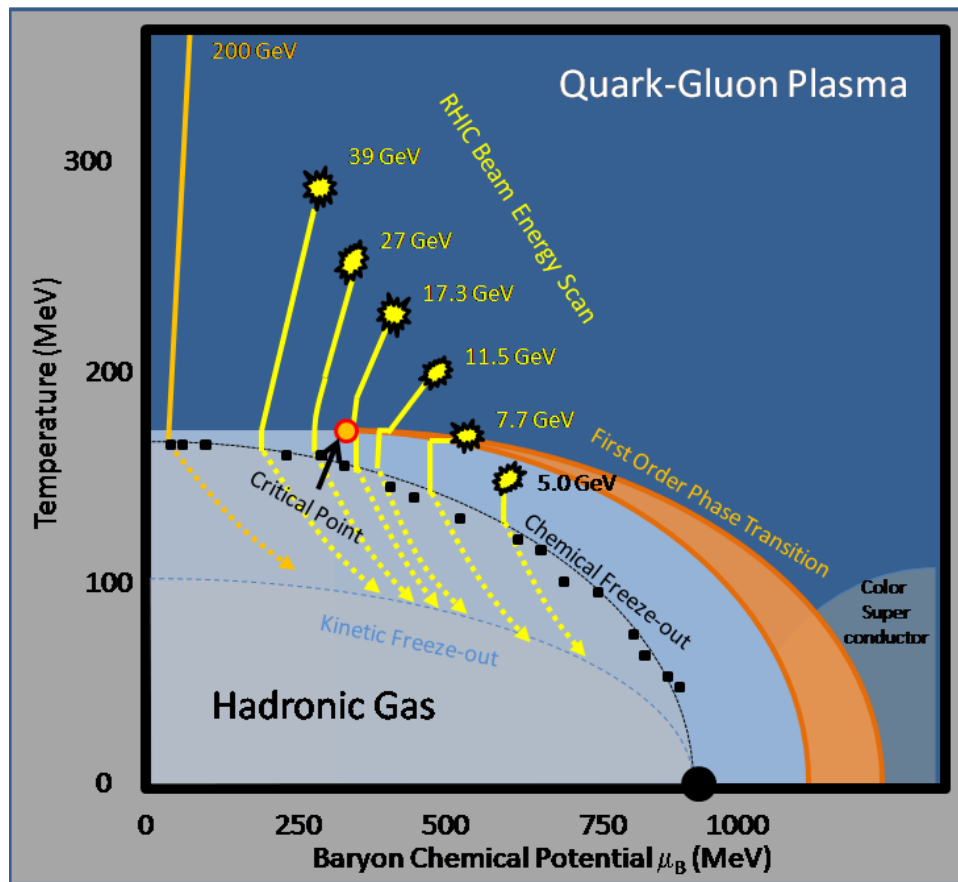


Figure 1.9: Experimental view of the QCD phase diagram. The RHIC Beam Energy Scan probes the different regions of the phase transition in search of a critical point. Chemical freeze-out indicates the cessation of inelastic scattering, while kinetic freeze-out indicates the cessation of elastic scattering.

The existence of the QGP is not only supported by QCD. Heavy-ion collision experiments have discovered a wealth of data and phenomena that support the creation of the QGP in experiments. Some of these observations were: J/ψ suppression [16], enhanced production of strange hadrons in heavy-ion collisions (compared to pp collisions) [17], strong suppression of high energy jets and heavy quarks [18], and large azimuthal asymmetry in the particle yields or elliptic flow, v_2 [19]. What was surprising about the experimental measurements was that if the QGP consisted of weakly interacting quarks and gluons, then why did it show fluid dynamic behavior (from the v_2 measurements) and jet quenching (from strongly suppressed high energy jets)? What experiment discovered was that the QGP was in fact, a strongly interacting liquid [20] [21] [22] [23].

At high temperatures the quarks and gluons have thermal momenta with $p \approx T \geq \Lambda_{QCD}$. Although asymptotic freedom implies a weakly interacting QGP due to high momentum transfer between particles in the QGP that interact at large scattering angles, there is a large thermal population of mobile charges, where $n \approx T^3$, so that, at the point where Debye screening dominates, the density of mobile charges effectively screens the interaction at distances beyond the Debye length, leading to deconfinement. This implies that the high temperature QGP must be separated from the low temperature hadronic phase by a phase transition. The question is what is the nature of the phase transition. Is it first order, second order, or a rapid crossover? Lattice QCD calculations predict that the phase transition is first order if the quarks (u, d, s) are assumed to be massless. If instead the light quarks (u, d), are considered to be massless and the heavier quarks, (s, c, b, t), are considered massive, the phase transition is second order [24]. However, for realistic quark masses the phase transition is a rapid crossover [25]. An order parameter, the chiral condensate (given that the QGP is chirally symmetric), can be used to probe the existence of a transition temperature, T_c . The results show $T_c \approx 151 \pm 3 \pm 3 \pm \text{MeV}$ [26], which occurs at vanishing baryon chemical potential, μ_B . At larger chemical potentials, the rapid crossover might turn into a first order phase transition, with a critical point separating the crossover from the first order phase transition line [27]. At the critical point, the correlation length of the system diverges. This implies that in heavy-ion collisions, within the vicinity of the critical point, the phase transition can be probed via

enhanced fluctuations [28]. The focus of this dissertation is the region of the QCD phase diagram where a rapid crossover is expected at high T and close to zero μ_B .

In the region of high baryon chemical potential, there is, instead, cold quark matter. This is a rich, yet completely separate line of study in the phase structure of strongly interacting matter. However, it is important to point out that the main difference between the hot QGP and cold quark matter is that dense population of states near the quark Fermi surface leads to qualitative changes in the ground state of dense matter. In this super dense liquid of quarks, attractive interactions between quark pairs lead to a color superconductivity and the formation of a $\langle qq \rangle$ condensate.

1.3.2 Hadronization model and its freeze-out parameters

Statistical hadronization models are useful in predicting hadron production in ultra-relativistic nucleus-nucleus collisions. The first successful use of a statistical hadronization model was achieved in 1994 for Brookhaven AGS and Si + Au(Pb) collisions data [31]. Nucleus-nucleus collisions are highly dynamical events. Five distinct stages can be identified through the evolution of the collision, namely: (i) initial collisions, (ii) thermalization, (iii) expansion and cooling, (iv) chemical freeze-out, and (v) kinetic freeze-out. A schematic of these stages is shown in fig. 1.10, where the vertical lines show a demarcation of the different stages. At the initial stage, the fireball is formed. At

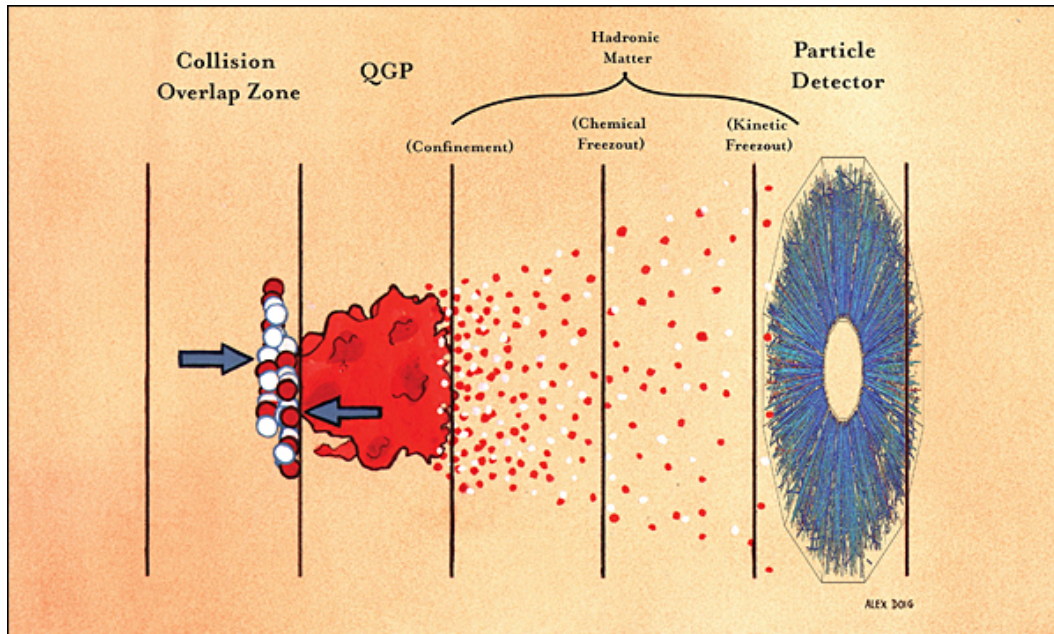


Figure 1.10: State of matter during the evolution of the collision process. The collision overlap zone represents the initial collision. The confined hot matter reaches thermalization in the next stage. This is followed by expansion and cooling of the deconfined matter, which in turn reaches chemical, and kinetic freeze-out before hitting the detector.

thermalization, equilibrium is established, while at chemical freeze-out (possibly hadronization), the inelastic collisions cease, which implies the hadron yields and distribution over species are frozen. At kinetic freeze-out, elastic collisions are fixed, implying spectra and correlations are frozen. The statistical or thermal hadronization model describes the chemical freeze-out of the collision, which is

assumed to be driven by rapid changes in energy and entropy density near the phase boundary [32]. The fireball created in the collision is assumed to be in chemical equilibrium when rapid changes in density near the phase boundary lead to an almost simultaneous freeze-out of all hadrons at the chemical freeze-out temperature, T , and chemical freeze-out baryon chemical potential, μ_B . T and μ_B are the so-called chemical ‘freeze-out’ parameters. The extracted parameters (T and μ_B) as a function of center of mass energy in the thermal model show that μ_B drops monotonically with increasing collision energy, and T initially increases but levels off at center of mass energies per colliding nucleon pair of about 20 GeV and at a temperature of around 160 MeV (as shown in fig. 1.11). The freeze-out points of fig. 1.11 can be put together for a phenomenological

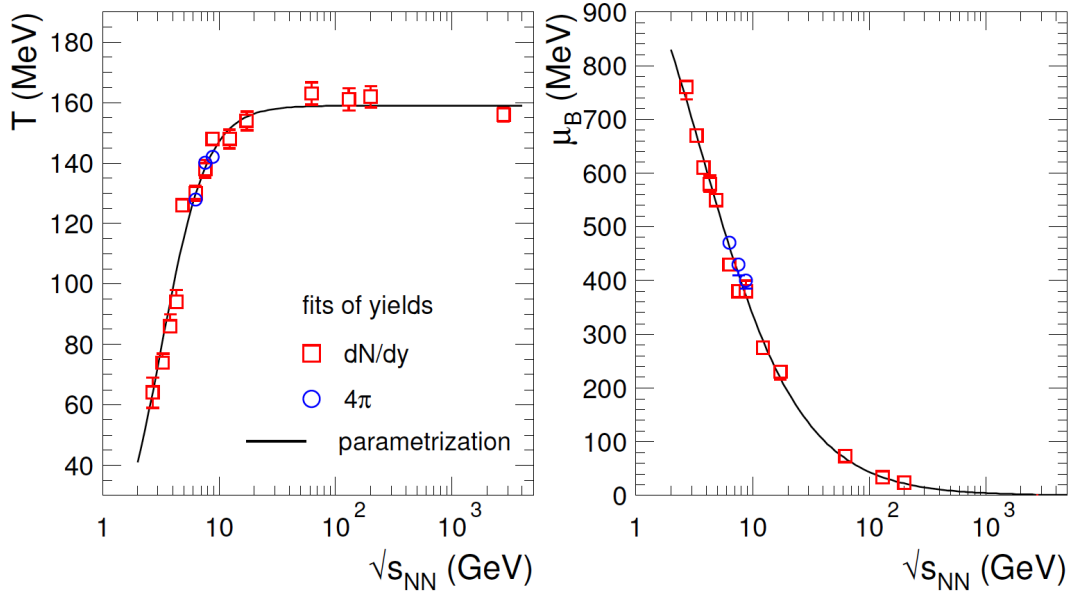


Figure 1.11: Energy dependence of the thermal parameters: T and μ_B . The red square boxes are the yields from data. The data are from mid-rapidity, $y = 0$ (where all the particles are emitted in the transverse direction). Rapidity is a measure of energy and longitudinal momentum ($y = 1/2 \ln[(E + P_L)/(E - P_L)]$). Figure taken from [34].

version of the QCD phase diagram (as shown in fig. 1.12). The thermal model fit results show an increase in T with increasing collision energy or equivalently, decreasing μ_B from about 50 MeV to about 160 MeV, where it exhibits a saturation for μ_B at approximately less than 300 MeV. Each

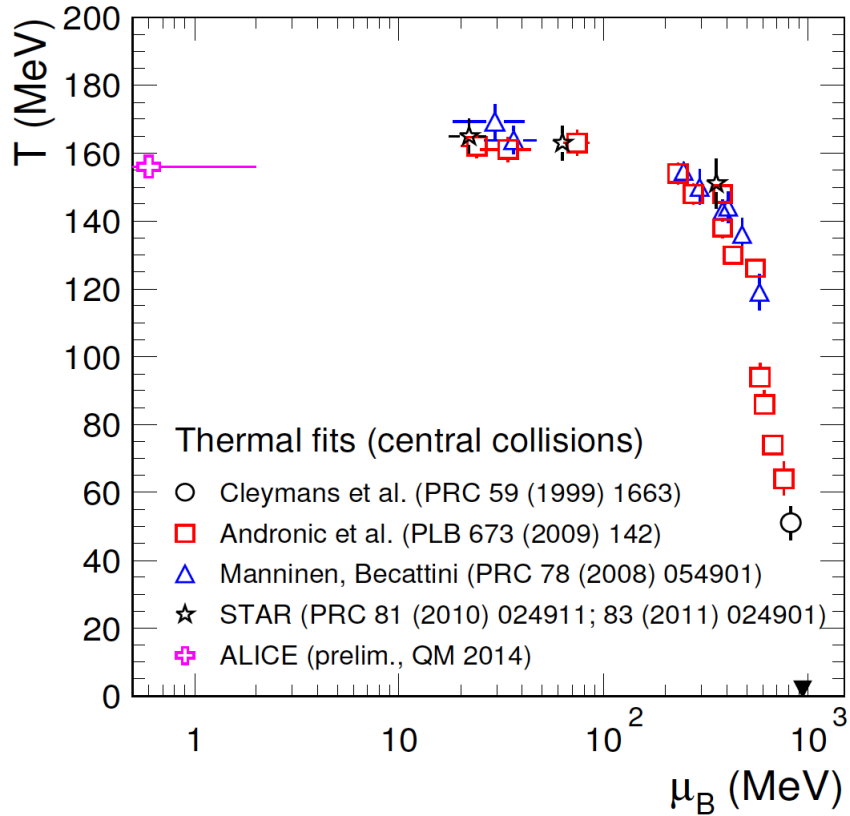


Figure 1.12: Phase diagram of strongly interacting matter. The points represents the thermal fits of hadron yields at various collision energies [35] [36] [37].

thermal model point corresponds to a fit of hadron yields in central Pb-Pb or Au-Au collisions at a given collision energy. The points are from several independent analyses. The success of the thermal model predictions in providing a freeze-out surface supported by QCD theory calculations makes this phenomenological model a very reliable tool in mapping the phase structure of strongly interacting matter.

1.3.3 QCD Equation of State (EOS)

The QCD EOS determines the dependence of the pressure of the system on the energy and baryon density and on the temperature and chemical potential—that is, $P = P(\mathcal{E}, n_B)$ and $P = P(T, \mu)$ respectively. This comes directly from the fact that in thermodynamic equilibrium the total electric charge must be zero, and strangeness is not conserved. In order to extract the expansion of the hot dense matter, the speed of sound, c_s^2 , can be defined as:

$$c_s^2 = \left. \frac{\partial P}{\partial \mathcal{E}} \right|_{s/n_B} \quad (11)$$

where the derivative of the pressure with respect to the energy is taken at constant entropy per baryon.

The EOS gives a useful picture as it depicts how gradients in the energy density profile are translated into pressure gradients. The speed of sound has predictive capabilities in the different regimes of the QCD phase diagram. At high temperatures, where $T \gg T_c$, the EOS is $\mathcal{E} = 3P$, implying that (from Eq. 11), $c_s^2 = 1/3$. This value for the speed of sound is also true for the case of low temperature and $n_B = 0$, where the pressure is dominated by weakly interacting (massless) pions. The behavior of the speed of sound as the QCD phase diagram is approached from low and high temperatures is therefore: a rise towards $c_s^2 = 1/3$, where upon approaching the crossover temperature the compressibility of matter is high and c_s^2 has a minimum for the low temperature and $n_B = 0$ regime; whereas, at high temperatures c_s^2 increases towards the perturbative value of $1/3$ —implying that a system produced with an initial energy density far above the critical density will initially accelerate rapidly and then cruise through the phase transition (see fig. 1.13).

1.3.4 Lattice QCD (LQCD)

Lattice QCD (LQCD) is based on the Euclidean path integral representation of the partition function, $Z = \exp(-\beta(H - \mu N))$, such that,

$$Z(T, \mu, V) = \int DA_\mu D_{q_f} D_{\bar{q}_f} \exp(-S_E) \quad (12)$$

where S_E is the Euclidean action:

$$S_E = - \int_0^\beta d\tau \int_V d^3x \mathcal{L}^E \quad (13)$$

and β is the inverse temperature and \mathcal{L}^E is the Euclidean Lagrangian obtained by analytically continuing the QCD Lagrangian to imaginary time, $\tau = it$. For reference, the QCD Lagrangian is:

$$\mathcal{L}_{QCD} = -\frac{1}{4} G_{\mu\nu}^a G_a^{\mu\nu} + \bar{\psi}_i (i(\gamma^\mu D_\mu)_{ij} - m\delta_{ij}) \psi_j \quad (14)$$

where $G_{\mu\nu}^a$ is the QCD gluon field strength tensor, ψ represents the quark field, D_μ is the gauge covariant derivative, m is the mass of the quarks, and γ^μ are the Dirac matrices. A chemical potential that couples with \mathcal{L}^E can be constructed as:

$$\mathcal{L}^E(\mu) = \mathcal{L}^E(0) + \mu \bar{\psi} \gamma_0 \psi \quad (15)$$

Lattice QCD comes in when the Lagrangian is discretized on an $N_\tau \times N_\sigma^3$ space-time lattice with lattice spacing a_τ and a_σ , although $a_\tau = a_\sigma = a$ is typically used in calculations. Other variables include the volume, V , with $V = L^3$, and $L = N_\sigma a_\sigma$. At finite temperature calculations, β is typically chosen to be less than L , where $\beta = N_\tau a_\tau$. The thermodynamic quantities are determined by taking suitable derivatives of the partition function (Eq. 12). For example, the energy and

baryon density can be extracted as follows:

$$\mathcal{E} = -\frac{1}{V} \frac{\partial \log Z}{\partial \beta} \Big|_{\beta\mu} \quad (16)$$

$$n_B = \frac{1}{\beta V} \frac{\partial \log Z}{\partial \mu_B} \Big|_{\beta} \quad (17)$$

In the LQCD representation, the lattice sites represent the quark fields, while the gluon fields are defined as the links connecting neighboring sites. In the case when the lattice is large enough and the sites are infinitesimally close to each other, the continuum QCD is recovered [29]. Hence, when $a \rightarrow 0$, the continuum limit has been achieved. The issue with lattice QCD is that at non-zero chemical potential, that is, with $\mu > 0$, the quarks are favored over the anti-quarks. This imbalance breaks the charge-conjugation symmetry leading to a complex determinant that is not equal to its real determinant. This is the famous ‘sign problem’ that restricts lattice QCD calculations to small μ_B and high T . In this region, the partition function is expanded in a Taylor series in μ_B/T [30], where the coefficients are the generalized susceptibilities. A detailed description of the generalized susceptibilities is presented in chapter 2.

1.3.5 Theory meets phenomenological model

As was indicated in section 1.3.3, the speed of sound squared can be extracted from the QCD equation of state. The same observable can be calculated with a hadronization model for comparison. In this case, the hadronization model is the Hadron Resonance Gas (HRG) model. HISQ and stout shown in fig. 1.13 are different kinds of simulations in LQCD. The result can be interpreted as follows: at the point where HRG calculation deviates from LQCD calculations (the black line deviates from the gray and red bands), one can infer that it is at this point that the degrees of freedom of the system changes. That is, the deviation infers moving from hadron degrees of freedom to quark and gluon degrees of freedom. One can visualize the tools as a way of looking at the same line from different sides, where the line in this case, is the hadronization line of the QCD phase diagram.

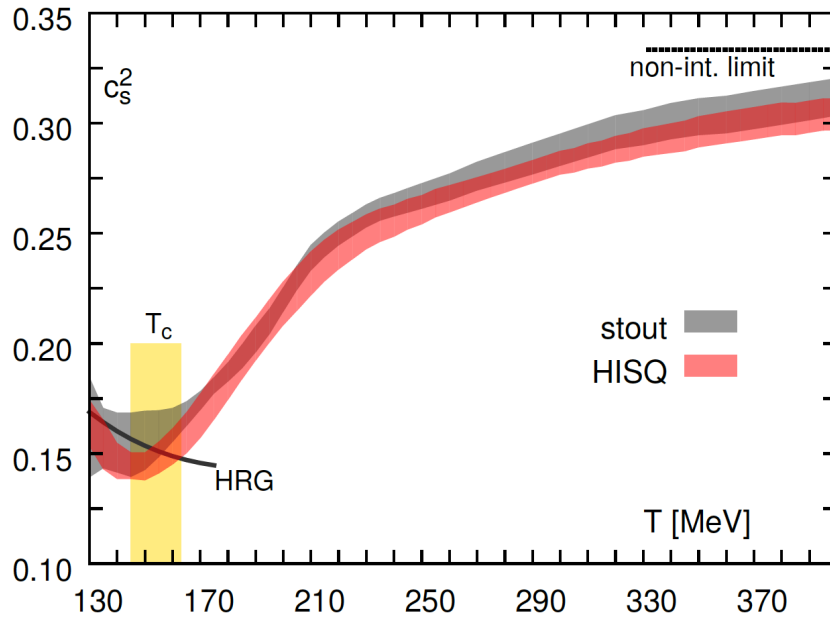


Figure 1.13: The speed of sound squared from lattice QCD (HISQ and stout) and the HRG model versus temperature. The vertical band marks the crossover region, $T_c = (154 \pm 9)$ MeV. The horizontal line to the top right corresponds to the ideal gas limit. Figure taken from [38].

2 Fluctuations of conserved quantities

There is sufficient evidence that the system created in heavy-ion collisions reaches thermalization. A claim can be made about reaching thermalization because the total abundances of produced particles in heavy-ion collisions can be described by a simple thermal model that depends on only two parameters —the temperature, T , and chemical potential, μ_B , at chemical freeze-out. In a system that thermalizes, thermal fluctuations are expected due to the fact that thermodynamics is a coarse-grained description of the system —that is, thermodynamic variables fluctuate in a finite sub-volume. The concern is not with fluctuations associated with the initial state of the collision. The initial state fluctuations exist due to inhomogeneities in the initial energy and baryon number deposition. However, if the system thermalizes and is described by fluid dynamics, then the expectation is that the fluctuations in the subsequent evolution of the collision is primarily statistical. For a volume, V , if N is the average number of particles in V , then the thermal fluctuations are of the order $1/\sqrt{N}$. However, in the vicinity of a phase change, the thermal fluctuations can become large. Experimentally, these thermal fluctuations can be accessed by measuring event-by-event distributions, where a given observable is measured on an event-by-event (or collision-by-collision) basis and its corresponding fluctuations are studied for the ensemble of events. The system created in heavy-ion collisions is a canonical ensemble where, the conserved quantum numbers: net-charge, net-strangeness, and net-baryon number are conserved. However, the detector is limited in terms of acceptance —that is, it does not detect all particles produced in the collision, hence it can be treated as a grand-canonical ensemble.

2.1 Fluctuations of conserved quantities in a thermal system

In a grand-canonical ensemble (GCE), the system is in contact with an energy and “charge” reservoir. Where, in this case, charge represents electric charge, baryon number or strangeness number. In a GCE, the charges are only conserved on average, where the average is controlled by the temperature and chemical potential. A partition function for the conserved charges, Q_i , can be

constructed as:

$$Z = \text{Tr}[\exp(-\frac{H - \sum_i \mu_i Q_i}{T})] \quad (18)$$

Fluctuations of conserved quantities can be described with susceptibilities of that quantity. The susceptibilities are defined as the derivatives of the partition function with respect to the appropriate chemical potentials.

2.1.1 Susceptibilities of conserved quantities from LQCD

Based on lattice QCD, the susceptibilities of the conserved quantities: baryon number (B), strangeness number (S), and electric charge (Q) are:

$$\chi_{n_B, n_S, n_Q}^{B,S,Q} \equiv \frac{1}{VT^3} \frac{\partial^{n_B}}{\partial(\mu_B/T)^{n_B}} \frac{\partial^{n_S}}{\partial(\mu_S/T)^{n_S}} \frac{\partial^{n_Q}}{\partial(\mu_Q/T)^{n_Q}} \ln Z \quad (19)$$

With $P = T/V \ln(Z)$, the susceptibilities can be expressed in terms of derivatives of the pressure as:

$$\chi_{n_B, n_S, n_Q}^{B,S,Q} \equiv \frac{\partial^{n_B}}{\partial(\mu_B/T)^{n_B}} \frac{\partial^{n_S}}{\partial(\mu_S/T)^{n_S}} \frac{\partial^{n_Q}}{\partial(\mu_Q/T)^{n_Q}} \left(\frac{P}{T^4} \right) \quad (20)$$

At sufficiently small μ_B , the susceptibilities control the pressure. Consequently, the pressure can be expressed in terms of a Taylor series:

$$\frac{P(T, \mu_B)}{T^4} = \frac{P(T, \mu_B = 0)}{T^4} + \sum_n c_n \left(\frac{\mu_B}{T} \right)^n \quad (21)$$

Equivalently:

$$\frac{P(T, \mu_B)}{T^4} = c_0(T) + c_2(T) \left(\frac{\mu_B}{T} \right)^2 + c_4(T) \left(\frac{\mu_B}{T} \right)^4 + c_6(T) \left(\frac{\mu_B}{T} \right)^6 + \mathcal{O}(\mu_B^8) \quad (22)$$

The expansion coefficients are given by the baryon-number susceptibilities, such that,

$$c_n = \frac{\chi_n^B}{n!} \quad (23)$$

By putting $\mu_Q = \mu_S = 0$, and using Eq. 23, Eq. 21 can be written as [39]:

$$\frac{P(T, \mu_B) - P(T, 0)}{T^4} = \frac{1}{2} \chi_2^B(T) \left(\frac{\mu_B}{T}\right)^2 \times \left[1 + \frac{1}{12} \frac{\chi_4^B(T)}{\chi_2^B(T)} \left(\frac{\mu_B}{T}\right)^2 + \frac{1}{360} \frac{\chi_6^B(T)}{\chi_2^B(T)} \left(\frac{\mu_B}{T}\right)^4 \right] + \mathcal{O}(\mu_B^8) \quad (24)$$

Only the even terms of Eq. 24 remain due to charge conjugation symmetry of QCD. From Eq. 24 it can be seen that the leading order (LO), next-to-leading order (NLO), and next-to-next-to-leading order (NNLO) are related to the baryon number susceptibilities: χ_2^B , $\frac{\chi_4^B}{\chi_2^B}$, and $\frac{\chi_6^B}{\chi_2^B}$ respectively. Those susceptibilities are defined in Eq. 19 and can be evaluated at $\mu_B = \mu_S = 0$. Results of the first two susceptibilities (χ_2^B and $\frac{\chi_4^B}{\chi_2^B}$) from the Taylor expansion of Eq. 24 can be found in fig. 2.1. The results show that at low temperatures there is agreement between LQCD calculations and HRG (thermal model) results. However, at high temperatures the two approaches deviate from each other close to the chemical freeze-out temperature. For reference, the ratio of cumulants of baryon number in the HRG model give 1 when the ratio includes cumulants of the same parity (even or odd) [42]. Otherwise, the value is $\tanh(\mu_B/T) \Big|_{\mu_Q=\mu_S=0}$.

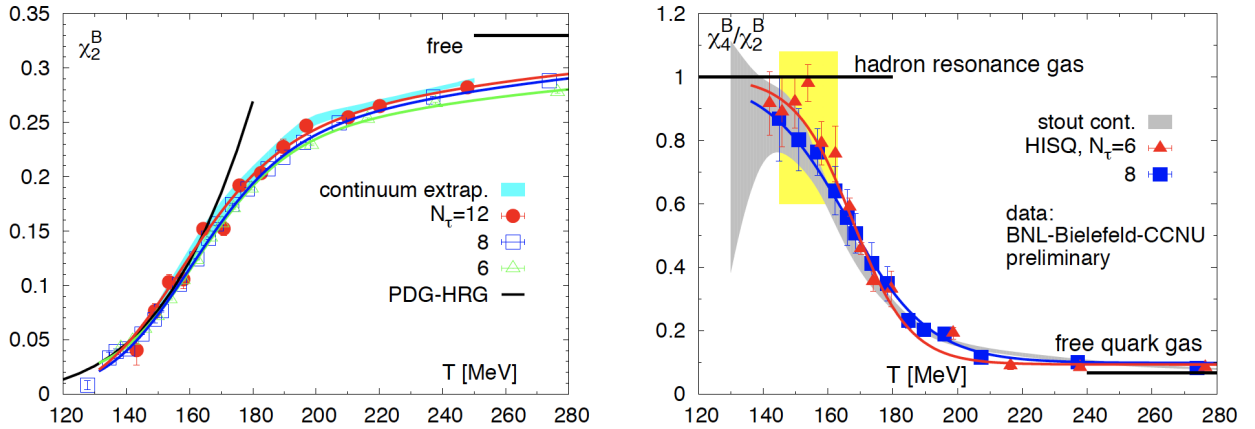


Figure 2.1: BNL-Bielefeld-CCNU collaboration results of baryon number susceptibility: χ_2^B (left) and $\frac{\chi_4^B}{\chi_2^B}$ (right) as a function of temperature computed from LQCD at $\mu_B = 0$ [39]. $N_\tau = 1/aT$ are the inverse lattice spacings and the horizontal line on the left plot is the value for a non-interacting gas. The continuum extrapolated results are for lattice spacing, a , extrapolated to $a = 0$. The yellow vertical band on the right plot marks the phase crossover region, $T_c = (154 \pm 9)$ MeV.

2.1.2 Chemical freeze-out parameters from LQCD

As stated in section 1.3.2, the hadron resonance gas (HRG) model is successful in describing chemical freeze-out conditions of heavy-ion collisions. The results from HRG have been shown to agree quite well with LQCD results at low temperatures. However, the HRG model relies on the abundance of hadrons, which is not well known in the case of higher mass resonant states. Therefore, it is more desirable to extract the freeze-out conditions by direct comparison of LQCD calculations with experimental data. The goal is to compare ratios of cumulants of conserved quantities from data and LQCD. In the LQCD sector, these are the ratios of the susceptibilities of a conserved quantity. If a selection is made on the ratio of the susceptibilities as follows: $\frac{\chi_3^B}{\chi_1^B}$ and $\frac{\chi_1^B}{\chi_2^B}$, then their Taylor expansion around $\mu_B = 0$ will read [40]:

$$\frac{\chi_3^B(T, \mu_B)}{\chi_1^B(T, \mu_B)} = \frac{\chi_4^B(T, 0) + \chi_{31}^{BQ}(T, 0)q_1(T) + \chi_{31}^{BS}(T, 0)s_1(T)}{\chi_2^B(T, 0) + \chi_{11}^{BQ}(T, 0)q_1(T) + \chi_{11}^{BS}(T, 0)s_1(T)} + \mathcal{O}(\mu_B^2) \quad (25)$$

$$\frac{\chi_1^B(T, \mu_B)}{\chi_2^B(T, \mu_B)} = \frac{\chi_2^B(T, 0) + \chi_{11}^{BQ}(T, 0)q_1(T) + \chi_{11}^{BS}(T, 0)s_1(T)}{\chi_2^B(T, 0)} \frac{\mu_B}{T} + \mathcal{O}(\mu_B^3) \quad (26)$$

The leading order in $\frac{\chi_3^B}{\chi_1^B}$ of Eq. 25 is independent of μ_B . This allows for the extraction of the chemical freeze-out temperature, T . Upon extraction of T , it can be used in Eq. 26 to extract the chemical freeze-out baryon chemical potential, μ_B . As a quick check, using the fact the ratio of cumulants of baryon number give 1 when the ratio consists of cumulants of the same parity, it indicates that $\frac{\chi_3^B}{\chi_1^B} = 1$ and $\frac{\chi_1^B}{\chi_2^B} \approx \tanh(\mu_B) \approx \mu_B$. It can be inferred that $\frac{\chi_1^B}{\chi_2^B}$ depends strongly on μ_B , while $\frac{\chi_3^B}{\chi_1^B}$ depends only mildly on μ_B . As a result, $\frac{\chi_1^B}{\chi_2^B}$ constrains the baryon chemical potential while $\frac{\chi_3^B}{\chi_1^B}$ constrains the temperature.

2.2 Fluctuations of conserved quantities in experiment

Fluctuations of net-particle multiplicities in heavy-ion collisions are sensitive observables in probing the phase structure of strongly interacting matter [41]. They have a well defined physical interpretation for a system in thermal equilibrium. In order to study the fluctuations of the system

created in heavy-ion collisions, an efficient way is to measure an observable on an event-by-event basis, then study the fluctuations over the ensemble of the events. The net number of quantities (net-charge, net-strangeness, and net-baryon number) are conserved in a closed system. The magnitude of fluctuations in a grand canonical ensemble at finite temperature are distinctly different in the quark gluon plasma and hadronic phases of the QCD phase diagram. As already stated, the event-by-event fluctuation of conserved quantities created in experiment is one of the observables used to study the properties of the QCD phase diagram. Event-by-event particle multiplicity fluctuations are characterized by the cumulants of the event-by-event multiplicity distributions. If N is the net-particle number, i.e., particle *minus* antiparticle, then the cumulants can be calculated as follows:

$$C_1 = \langle N \rangle \quad (27)$$

$$C_2 = \langle (\delta N)^2 \rangle \quad (28)$$

$$C_3 = \langle (\delta N)^3 \rangle \quad (29)$$

$$C_4 = \langle (\delta N)^4 \rangle - 3\langle (\delta N)^2 \rangle^2 \quad (30)$$

Where, $\delta N = N - \langle N \rangle$ is the deviation of N from the mean number of net-particle, C_1 . C_2 can be interpreted as the variance, hence, $C_2 = \sigma^2$. The skewness, S , and kurtosis, κ , can be extracted as follows:

$$S = \frac{C_3}{(C_2)^{\frac{3}{2}}} \quad (31)$$

$$\kappa = \frac{C_4}{(C_2)^2} \quad (32)$$

In addition, the cumulant products: $\kappa\sigma^2$ and $S\sigma$, can be expressed in terms of the ratio of cumulants. Their formulae are:

$$\kappa\sigma^2 = \frac{C_4}{C_2} \quad (33)$$

$$S\sigma = \frac{C_3}{C_2} \quad (34)$$

2.2.1 Connecting theory to experiment

A system in thermal equilibrium under a grand canonical ensemble can be characterized by its dimensionless pressure. The dimensionless pressure is related to the grand canonical QCD partition function by [39]:

$$\frac{P}{T^4} = \frac{1}{VT^3} \ln[Z(V, T, \mu_B, \mu_Q, \mu_S)] \quad (35)$$

where V and T are the volume and temperature of the system respectively. The chemical potential of baryon number, strangeness, and charge are: μ_B , μ_S , and μ_Q respectively. The susceptibilities can be extracted directly by taking derivatives of the log of the partition function. Such that,

$$\chi_{ijk}^{BQS} = \frac{\partial^{i+j+k}[P/T^4]}{\partial(\mu_B/T)^i \partial(\mu_Q/T)^j \partial(\mu_S/T)^k} \quad (36)$$

The cumulants of the conserved quantities are connected to the corresponding susceptibilities by:

$$C_{ijk}^{BQS} = \frac{\partial^{i+j+k} \ln[Z(V, T, \mu_B, \mu_Q, \mu_S)]}{\partial(\mu_B/T)^i \partial(\mu_Q/T)^j \partial(\mu_S/T)^k} \quad (37)$$

Using Eq. 36, a compact form of the relationship between cumulants and susceptibilities is:

$$C_{ijk}^{BQS} = VT^3 \chi_{ijk}^{BQS}(T, \mu_B, \mu_Q, \mu_S) \quad (38)$$

C_{ijk}^{BQS} denotes both the diagonal and off-diagonal cumulants of conserved quantities (B, Q, S) ($i, j, k = 1, 2, 3, 4 \dots n$). The list of diagonal cumulants (up to fourth order) are:

$$C_1 = VT^3 \chi_1 \quad (39)$$

$$C_2 = VT^3 \chi_2 \quad (40)$$

$$C_3 = VT^3 \chi_3 \quad (41)$$

$$C_4 = VT^3 \chi_4 \quad (42)$$

From Eq. 38, the cumulants extracted in experiment are directly related to the susceptibilities extracted in theoretical calculations, apart from a volume term. The reality is that the volume of the system created in experiment is not known. Hence, in order to compare theory to experiment, ratios of the susceptibilities can be taken to remove the volume dependence. Suitable ratios of the mean (C_1), variance (C_2), as well as with the third and fourth order cumulants can be extracted. The skewness (S) and kurtosis (κ), which are zero for a Gaussian distribution can also be extracted. These relationships are listed in Eq. 43 through Eq. 46.

$$\frac{C_2}{C_1} = \frac{\sigma^2}{M} = \frac{\chi_2}{\chi_1} \quad (43)$$

$$\frac{C_3}{C_2} = S\sigma = \frac{\chi_3}{\chi_2} \quad (44)$$

$$\frac{C_4}{C_2} = \kappa\sigma^2 = \frac{\chi_4}{\chi_2} \quad (45)$$

$$\frac{C_4}{C_3} = \frac{\kappa\sigma}{S} = \frac{\chi_4}{\chi_3} \quad (46)$$

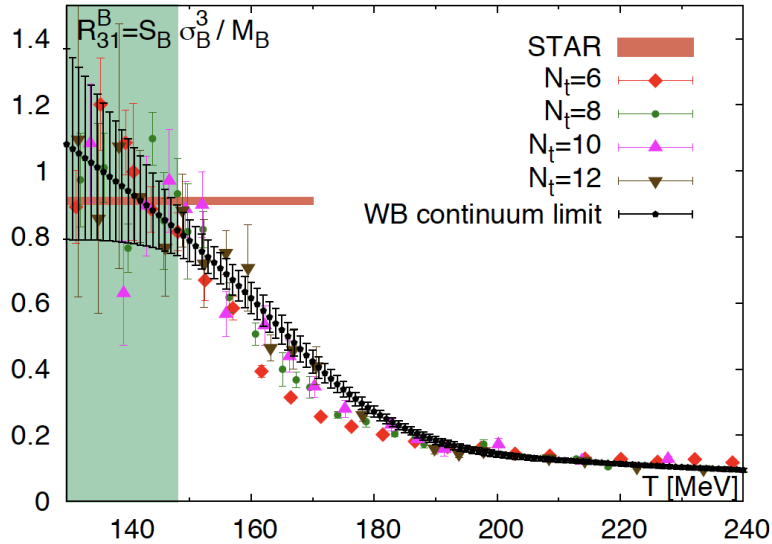


Figure 2.2: Comparison of lattice results with STAR data [43].

As stated in section 2.1.2 the susceptibility ratio: $\frac{\chi_3^B}{\chi_1^B}$ can be used to extract the chemical freeze out temperature. Fig. 2.2 shows a comparison of the cumulant ratio: $R_{31}^B = \chi_3^B/\chi_1^B = S_B\sigma_B^3/M_B$ from data collected at the STAR experiment [43] with lattice QCD calculations. The large error bars in the lattice QCD calculations allow for only an upper limit of the freeze-out temperature: $T < 148\text{MeV}$ (as can be seen in the green vertical band of fig. 2.2). However, it is this kind of measurements that tie experimental data and theoretical calculations together. It is from the comparison of the two that useful information about the QCD phase structure can be extracted.

2.2.2 Experimental limitations and considerations

Having established a link between lattice QCD and cumulants of conserved charges extracted in experiment, it is important to note some limitations in the comparison of the two. Heavy ion collision is a highly dynamical process whereas lattice QCD deals with a static system in global equilibrium. In addition, the experiments have limitations in acceptance —that is, an experiment does not detect all particles produced in the collision. The effect of limited acceptance is difficult to map onto lattice QCD calculations. As a result, a direct comparison of an experiment with lattice QCD calculations resulting in fluctuation observables is not a trivial task. The remainder of this section will discuss issues associated with experiments that need to be addressed before direct comparison with lattice QCD results.

- **Global charge conservation:** The charge in question are the electric charge, strangeness, and baryon number. Lattice QCD calculations are performed in a grand canonical ensemble, which allows for the exchange of conserved quantities with the heat bath, and thus, allows for their fluctuation. In experiment, the conserved quantities would be conserved globally with infinite acceptance. The approach done in an experiment is to try to mimic a grand canonical ensemble by analyzing a subset of the particles in the final state. However, this is not always successful as corrections due to global charge conservation are still required after extracting cumulants of the conserved charges.

- **Limited acceptance:** Detectors do not cover full phase space. As a result, not all particles that contribute to the conserved quantity under analysis are detected. Moreover, the experiments do not detect neutrons (due to its lack of electric charge), which carry baryon number and can affect the baryon number cumulants.
- **Efficiency corrections:** For particles that are actually detected in experiment, they are detected only with a probability commonly referred to as the efficiency, ε . Not only is the efficiency smaller than 1 by definition, ε fluctuates from event to event. This is because, in every event the same fraction of produced particles do not stay constant even if the number of produced particles is constant. So, in a sense, the finite detection efficiency gives rise to fluctuations which need to be removed before comparison with theoretical calculation.
- **Strangeness quantum number considerations:** The measured Λ carries 20% of the strangeness, while in lattice QCD calculations such limitation is not present. This underpins the issue of attempting to compare a quantum number in theoretical calculations to net-particle multiplicities in experiment. In addition, it is a required step to remove secondary Λ contributions from Ξ and Ω decays prior to the net- Λ fluctuation measurement.

2.3 Dissertation research motivation

As previously discussed, the conserved quantities (net-charge, net-strangeness and net-baryon number) are not directly accessible in experiment. A proxy for net-conserved quantity in theory is net-particle multiplicity in experiment. For example, in experiment, net-pion, net-kaon, and net-proton are proxies for net-charge, net-strangeness and net-baryon number respectively. It is inferred that based on the density of particles produced in the collision, a particle consisting of a majority of a particular conserved quantity should approximately represent that conserved quantity. The pions are abundantly produced in heavy-ion collisions at the ALICE experiment and because they are electrically charged, they stand as proxies for the net-charge fluctuation measurement. Next on the list in order of decreasing abundance of particles produced in the collision, are the kaons. They are also electrically charged, but since they carry strangeness they are used for the net-strangeness fluctuation measurement. The net-protons are next on the list and since they are baryons, they are the proxies for net-baryon fluctuation measurement. After the proton is the lambda particle. The lambda particle carries strangeness and baryon number. The flavors of quarks found in a lambda particle (Λ) are uds and for the anti-lambda particle ($\bar{\Lambda}$), they are $\bar{u}\bar{d}\bar{s}$. In terms of particle yield, the Λ is produced at about the same amount as the proton. The Λ is $\approx 20\%$ of strange particles produced in the collision. Hence a net-lambda ($\Lambda - \bar{\Lambda}$) fluctuation measurement can be studied to increase the coverage of the net-strangeness and net-baryon fluctuation measurements. For reference, fig. 2.3 shows the rapidity density of particles produced at the ALICE experiment. The horizontal lines are thermal fits to the yield.

The study of net-lambda fluctuation measurements can be taken further to inquire which quark flavor within the lambda particle precipitates freeze-out. The lambda consists of two light quarks: ud and one heavier quark: s . Theoretical calculations have direct access to quark degrees of freedom, therefore the quarks can be studied independently to extract a freeze-out temperature. Fig. 2.4 show results for lattice calculations of the second order susceptibility and the ratio of the fourth order to second order susceptibilities for light and strange quarks plotted against temperature. The results show different hadronization temperatures, with a preference for higher hadronization

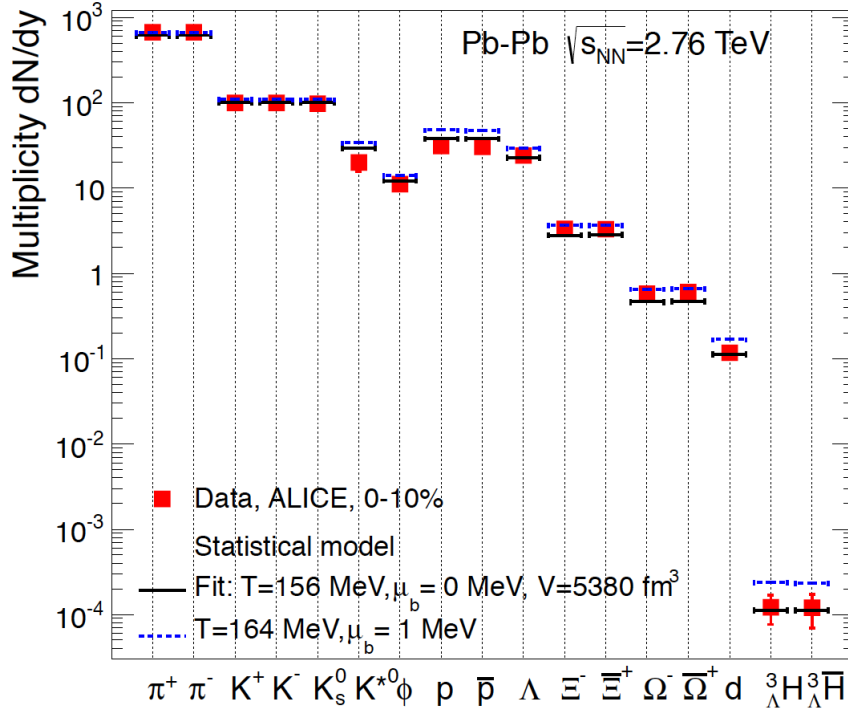


Figure 2.3: Thermal fits of the integrated hadron yields in Pb-Pb collisions at $\sqrt{s_{NN}} = 2.76$ TeV measured at ALICE. Figure taken from [44].

temperature (≈ 160 MeV) for the strange quarks. Given that the Λ particle consists of both light and strange quarks, the freeze-out temperature extracted with net- Λ fluctuation measurements will shed light on the dependence of quark flavors on chemical freeze-out. This is the phenomenon of sequential hadronization, which implies that particles formed in the collision do not hadronize all at once, rather they do so sequentially base on their quark content.

Net- Λ fluctuation measurements have already been carried out at the STAR experiment [46]. The STAR experiment collides Au-Au nuclei and is able to fine tune the colliding energies for varying values of center of mass energies. It was previously alluded that ratios of cumulants of net-particle multiplicities can be directly compared to ratios of susceptibilities of conserved quantities to extract a freeze-out (FO) temperature and baryon chemical potential. A reference was also made to HRG, a statistical hadronization model, that can be used to predict freeze-out conditions of the

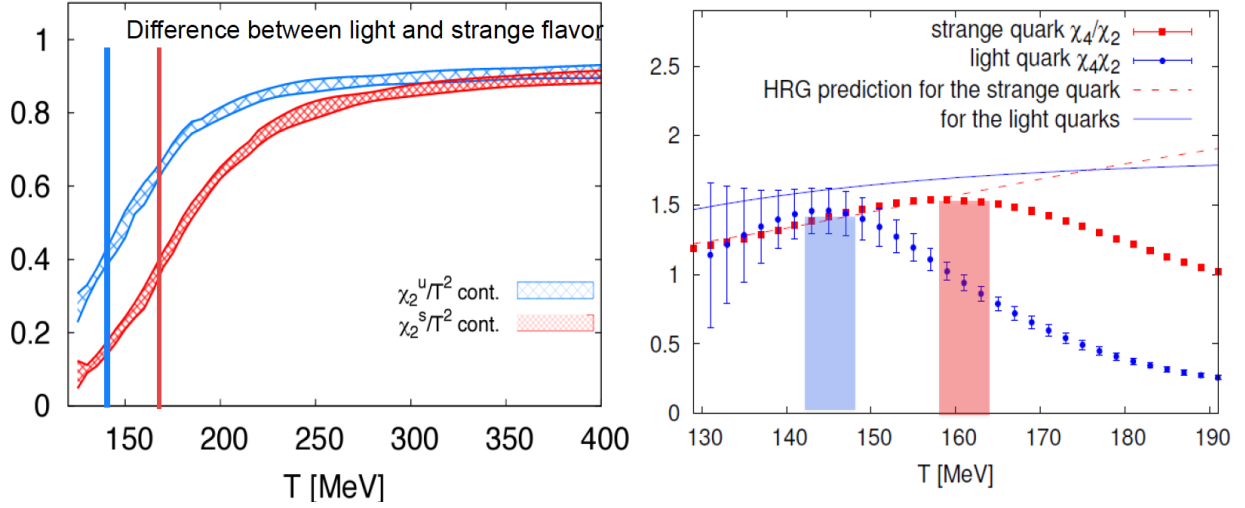


Figure 2.4: Continuum extrapolated lattice calculations on flavor specific susceptibilities. Left figure shows a comparison of the second order susceptibility of the light quark, χ_2^u , to the second order susceptibility of the strange quark, χ_2^s . Right plot shows a comparison of the ratio of the fourth order to second order susceptibilities for light and strange quarks $\frac{\chi_4}{\chi_2}$. Results are also shown for the respective HRG predictions. Figure taken from [45].

particles produced in heavy-ion collisions. The cumulant ratios can also be fit with the HRG model to map out a FO surface. A FO surface can be determined on the basis of the assumption that the lambda FO is like the kaon FO or that the lambda FO is like the charge/proton FO, so as to test for quark flavor dependence on chemical freeze-out. These results are depicted in fig. 2.5. It shows that for the lower cumulants ($\frac{C_2}{C_1}$) there might be a preference for the kaon FO conditions. This may imply that the lambda freeze-out is precipitated by its strangeness quantum number, rather than its baryon number. The higher cumulant measurements ($\frac{C_3}{C_2}$) appears to say the opposite—that is, the lambda FO might be closer to the charge/proton FO.

Net- Λ higher order even cumulants at the ALICE experiment can be used to investigate the existence of different FO surfaces based on light or strange quarks. This provides an additional motivation to study net- Λ fluctuation measurements at the ALICE experiment.

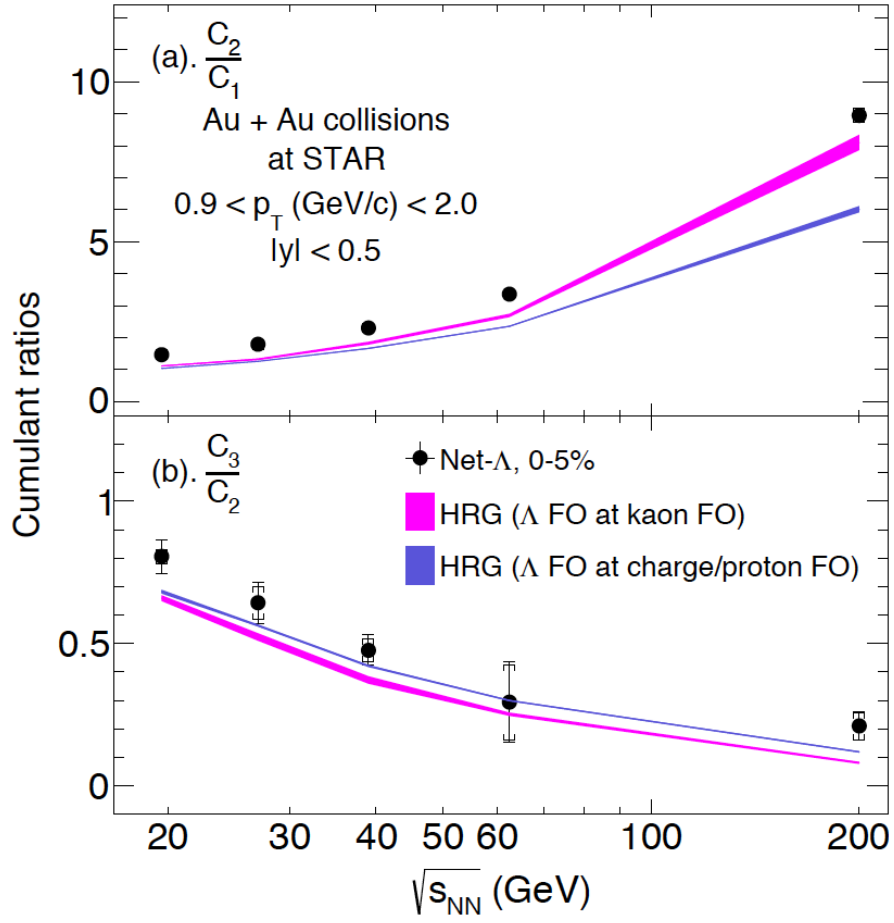


Figure 2.5: Predictions of net- Λ FO surface based on comparison of net- Λ cumulant ratios from the STAR experiment to HRG kaon and charge/proton FO. Figure taken from [46].

3 The ALICE experiment at the Large Hadron Collider (LHC)

The LHC is an accelerator based experiment housed in the CERN accelerator complex (see fig. 3.1). It houses four main active experiments: ALICE, ATLAS, CMS, and LHCb. Situated in the French-Swiss border, the LHC is 27 kilometer in circumference with mean depth of 100 meters.

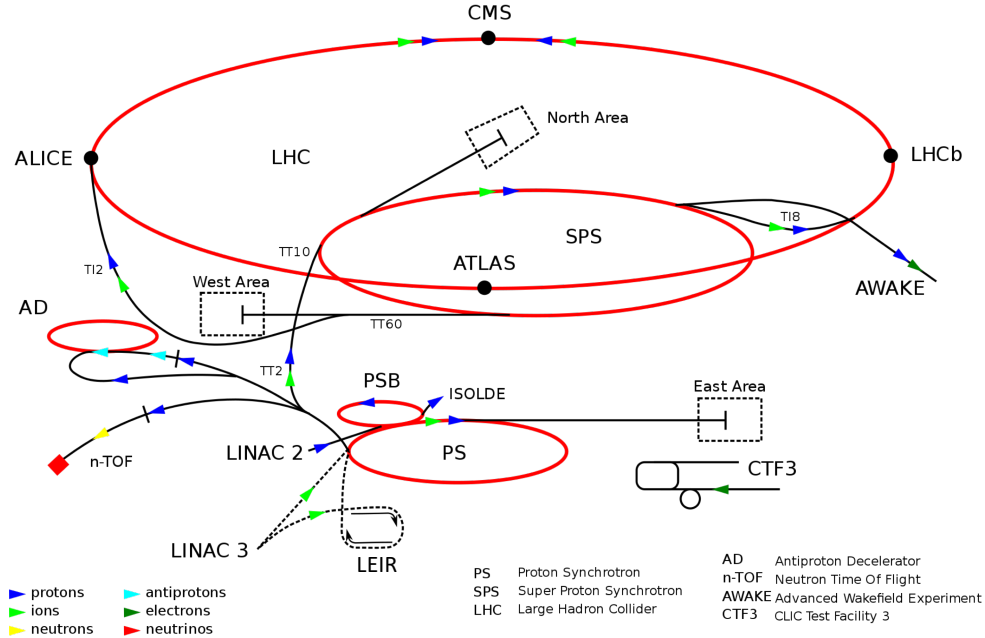


Figure 3.1: CERN accelerator complex.

Due to the LHC geometry and optimal magnetic field, the maximum design value of center of mass energy for pp and Pb-Pb collisions are 14 TeV and 5.5 TeV respectively. The center of mass energy, \sqrt{s} , is the total energy in the center of mass frame. That is, for two colliding particles, $s = (E_1 + E_2)^2 = 2E^2$, for the case where $E_1 = E_2$. A tera electron volt (TeV) is equal to 10^{12} eV, where $1\text{eV} = 1.602 \times 10^{-19}$ joules. The energy (7 TeV) to which the proton is accelerated results in a speed of 99.9999991 % the speed of light [51]. Note that in the case of Pb-Pb collisions, the center of mass energy quoted is the energy per nucleon ($\sqrt{s}_{NN} = 2.56$ TeV). The accelerator complex accelerates both proton and lead ions. Since the analysis of this dissertation is done with

lead ion collisions, a brief description of how they are accelerated follows.

The lead ions come from a highly purified lead sample that has been heated to a temperature of 800°C. The vapor is ionized by an electric current to produce several charge states of lead ions. Pb^{29+} is chosen, accelerated to 4.2 MeV/u (energy per nucleon), and passed through a carbon foil, which strips most of them to Pb^{54+} . They begin the next phase of acceleration at the Low Energy Ion Ring (LEIR), then to Proton Synchrotron (PS), and then passed through another foil, which strips them to Pb^{82+} before passing to the Super Proton Synchrotron (SPS). The SPS accelerates the lead ion to 177 MeV/u before passing it to the LHC, which accelerates it to 2.56 TeV/u [51].

3.1 A Large Ion Collider Experiment (ALICE)

ALICE (see fig. 3.2) is a detector specialized in measuring and analyzing lead-ion collisions. Its primary goal is to study the properties of the quark gluon plasma, which is the strong interaction sector of the Standard Model. Due to the fact that ALICE was designed for lead ion collisions, its primary design constraint is to cope with the extreme particle multiplicity anticipated in central Pb-Pb collisions. Its 18 different detector systems are optimized to provide high momentum resolution as well as excellent Particle Identification (PID) over a broad range of momentum [47]. The detector was built by a collaboration of over 1000 physicists and engineers from 105 institutions in 30 countries. Its overall dimensions are $16 \times 16 \times 26 \text{ m}^3$ and it weighs 10,000 tonnes. ALICE can be divided into two parts —the central barrel part and a forward muon spectrometer. The former is embedded in a large 0.5T solenoid magnet, covering polar angles from 45° to 135° , and specializing in measuring hadrons, electrons, and photons. From inside out, the subdetectors within the central barrel part are: the Inner Tracking System (ITS), the Time Projection Chamber (TPC), Time of Flight (TOF), Ring Imaging Cherenkov (HMPID), Transition Radiation (TRD) detectors, and two electromagnetic calorimeters (PHOS and EMCal). All detectors except HMPID, PHOS, and EMCal cover the full azimuth. The subdetectors within the central barrel are designed for particle identification and vertexing. The forward muon arm at 2° - 9° consists of a complex arrangement of absorbers, namely: the dipole magnet, fourteen planes of tracking, and triggering chambers.

Several small detectors, namely the Zero Degree Calorimeter (ZDC), Photon Multiplicity Detector (PMD), Forward Multiplicity Detector (FMD), Time Zero (T0), and VZERO (V0) are designed for global event characterization and triggering. The subdetectors used in the analysis of the data presented in this dissertation are the Time Projection Chamber, which is a particle identification detector and the VZERO detectors, which give an estimate of the event class. As a result, these subdetectors have their dedicated sections. A summary of the ALICE detector coordinate system precedes a description of the two subdetectors.

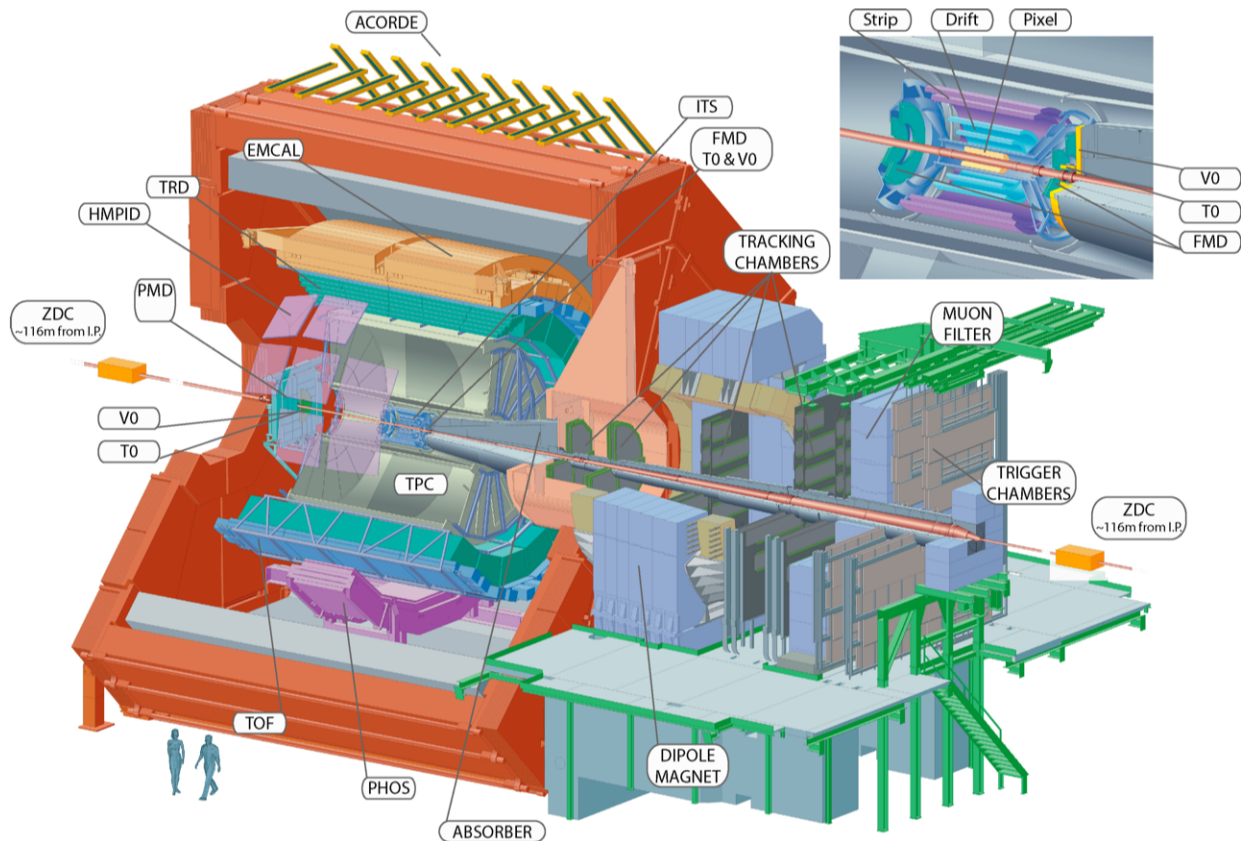


Figure 3.2: The ALICE experiment. Figure taken from [48].

3.2 ALICE Coordinate System

The ALICE coordinate system is a right-handed orthogonal Cartesian system with point of origin $x, y, z = 0$ at the beams interaction point (IP) [52]. As shown in fig. 3.3, the positive x-axis is perpendicular to the beam direction and points towards the Salève mountain. The positive y-axis is perpendicular to both the x and z axes and points upwards. The z-axis lies along the beam line with its positive direction towards side A (and the town of Bellegarde). The azimuthal angle, ϕ , increases counter-clockwise from x($\phi = 0$) to y ($\phi = \pi/2$) when looking from the side A of the detector. The polar angle, θ , increases from z($\theta = 0$) to x,y plane ($\theta = \pi/2$) and finally to -z($\theta = \pi$).

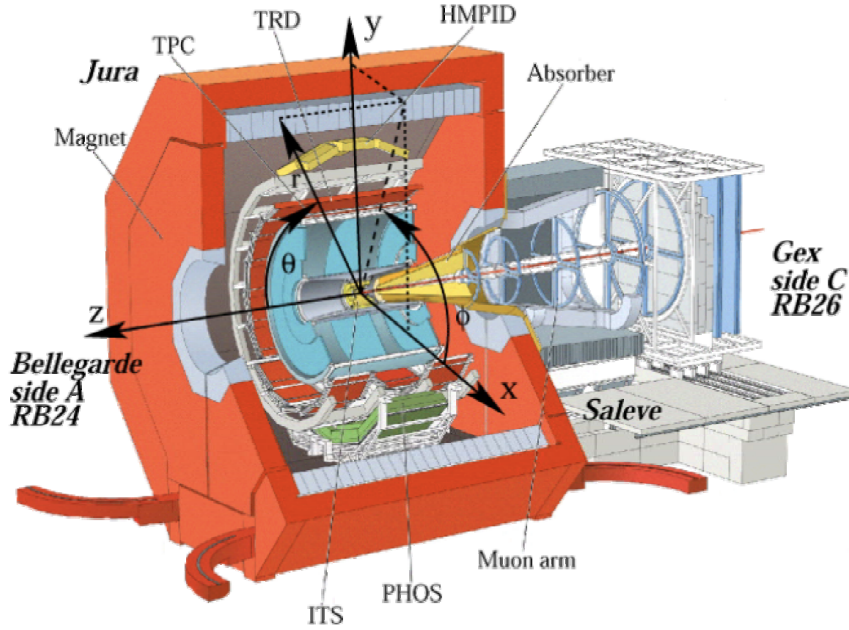


Figure 3.3: A description of ALICE coordinate system axis, angles and detector sides. Figure taken from [52].

The polar angle is associated with the pseudorapidity, η , referred to throughout this dissertation.

It is defined as:

$$\eta \equiv -\ln \left[\tan \left(\frac{\theta}{2} \right) \right] \quad (47)$$

3.3 ALICE Time Projection Chamber (TPC)

The Time Projection Chamber (TPC) is the main tracking detector of the central barrel. Together with the other central barrel detectors, it is optimized to provide charged particle momentum measurements with good two-track separation, particle identification, and vertex determination [49]. The TPC measures particles in high multiplicity environment through the principle of ionization energy loss. This is mathematically referred to as: dE/dx , i.e., the mean deposited energy per unit path length for a charged particle traversing the gas volume within the TPC. The phase space covered by the TPC in pseudo rapidity is $|\eta| < 0.9$ for tracks with full radial track length, i.e., tracks with matches in the ITS, TRD, and TOF detectors. The TPC covers full azimuth and large transverse momentum (p_T) of 0.1 GeV/c to 100 GeV/c with good momentum resolution. A distribution of the momentum resolution in different (p_T) ranges is shown in fig. 3.4. The figure shows a normalized resolution of 20 % at the highest momentum range (100 GeV/c) in Pb-Pb collisions at $\sqrt{s_{NN}} = 2.76$ TeV.

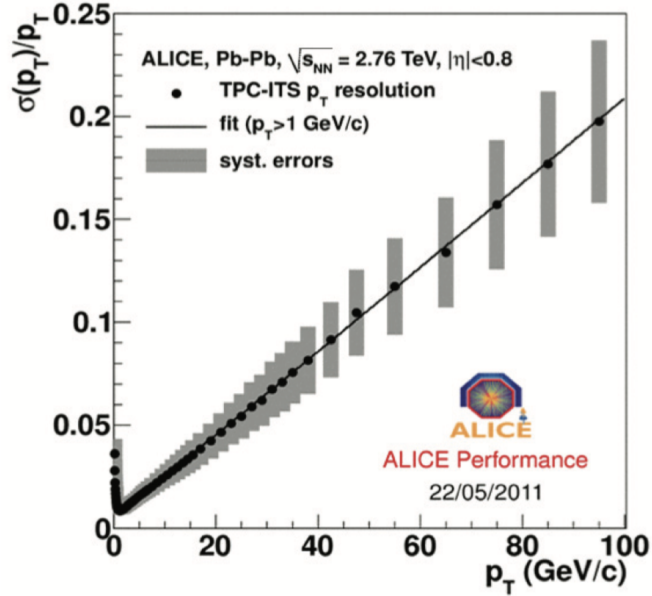


Figure 3.4: Transverse momentum resolution in the central rapidity region ($|\eta| < 0.8$) for TPC tracks combined with hits in the ALICE Inner Tracking System (ITS). Figure taken from [50].

3.3.1 TPC layout

The TPC is cylindrical in shape with an active volume of inner radius of about 85 cm, and an outer radius of about 250 cm, and an overall length along the beam direction of 500 cm (as pictured in fig. 3.5) [53].

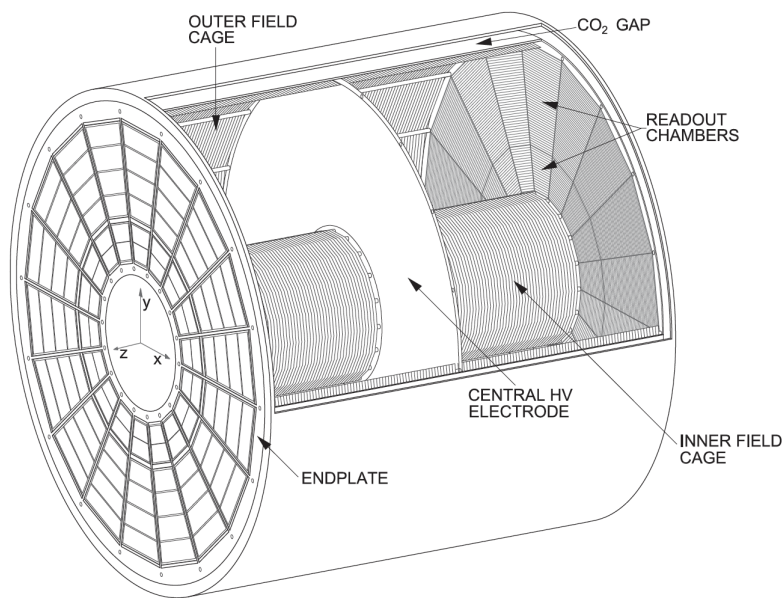


Figure 3.5: 3D view of the Time Projection Chamber. Figure taken from [54].

The large cylindrical field cage is filled with Ne/CO₂/N₂ in the following proportion: 90/10/5 with volume of 90 m³ (based on RUN 1 data taking). RUN 1 occurred from 2009-2013 during the first period of data taking at the LHC. Due to the Ne/CO₂/N₂ gas mixture, the field cage is operated at high voltage gradients of about 400 V/cm, with a voltage of 100 kV at the central electrode, which results in a maximum drift time of about 90 μ s. Surrounding the field cage is an insulating gas envelope of CO₂ in containment vessels. The combination of the field cage and the containment volumes are constructed from two concentric cylinders, which are sealed at the ends by the end plates on either side. The readout chambers are located by the end plates and they have an overall active area of 32.5 m² [54]. Their design is based on the Multi-Wire Proportional Chamber (MWPC) technique with cathode pad readout. Due to the fact that the track density

is radially dependent, the chambers are segmented radially into two readout chambers, namely the inner (IROC) and outer readout (OROC) chambers with slightly different wire geometry. The IROC have a radial range of 84.8 cm to 132 cm while the OROC have a radial range of 134.6 cm to 246.6 cm. To ensure the necessary dE/dx position and two-track resolution, there are about 560,000 readout pads of different sizes in the IROCs and OROCs. The IROCs consist of readout pads of size: $4 \times 7.5 \text{ mm}^2$ while the OROCs consist of readout pads of size: $6 \times 10 \text{ mm}^2$ and $6 \times 15 \text{ mm}^2$. The current detected by about 560,000 readout pads is read by the front-end electronics. The current signal is characterized by a fast rise time ($<1 \text{ ns}$) and a long tail of the order of $50 \mu\text{s}$. The signal tail is due to the motion of positive ions and is associated with pile-up effects, which sets the limit on the track density at which a MWPC can be operated. The front-end card (FEC) consists of 128 channels. In each channel, the current signal deposited by the pads of the chambers goes through the following pathway: a charge sensitive amplifier/shaper, a 10-bit 25 MHz low-power ADC, and a shortening filter. The shortening filter consists of a series of steps that include: tail cancellation, baseline subtraction and zero-suppression circuits, and a multiple-event buffer. One row of FECs (up to 25) are controlled by a Readout Control Unit (RCU) [56], which interfaces the FECs to the Data Acquisition (DAQ) System, Trigger (responsible for measuring global event characteristics), and the Detector Control System (DCS). A summary of the components of the TPC and their geometry are summarized in table 3.1.

TPC parameter	Parameter value
Pseudorapidity coverage	$-0.9 < \eta < 0.9$ for full radial track length
Azimuthal coverage	360°
Radial position of active volume	$848 \text{ mm} < r < 2466 \text{ mm}$
Length of active volume	$2 \times 2500 \text{ mm}$
segmentation in ϕ	18 sectors, 20°
segmentation in r	2 chambers per sector
Total number of readout chambers	$2 \times 2 \times 18 = 72$
IROC geometry	trapezoidal, $848 < r < 1321 \text{ mm}$ active area
pad size	$4 \times 7.5 \text{ mm}$ ($\phi \times r$)
pad rows	63
total pads	5504
OROC geometry	trapezoidal, $1346 < r < 2466 \text{ mm}$ active area
pad size	$6 \times 10 \text{ mm}$ and $6 \times 15 \text{ mm}^2$ ($\phi \times r$)
pad rows	$64 + 32 = 96$ (small and large pads)
total pads	$5952 + 4032 = 9984$ (small and large pads)
Detector gas	Ne/CO ₂ /N ₂ 90/10/5
Gas volume	90 m^3
Drift length	$2 \times 2500 \text{ mm}$
Drift field	400 V/cm
Drift velocity	$2.7 \text{ cm}/\mu\text{s}$
Maximum drift time	$92 \mu\text{s}$
Drift voltage	100 kV
IROC anode voltage	1350 V
OROC anode voltage	1570 V
Material budget	$X/X_0 = 3.5\%$ near $\eta = 0$
Front-End Cards (FEC)	$121 \text{ per sector} \times 36 = 4356$
Readout Control Unit (RCU) scheme	6 per sector, 18 to 25 FEC per RCU
Total RCUs	216
Total pads — readout channels	557568
Position resolution (σ) in $r\phi$	1100 to 800 μm inner / outer radii
Position resolution (σ) in z	1250 to 1100 μm
dE/dx resolution, isolated tracks	5.0 %
dE/dx resolution, $dN/dy = 8000$	6.8 %

Table 3.1: Time Projection Chamber parameters. Table adapted from [53].

3.3.2 TPC working principle

The TPC is filled with gas, which is ionized by charged particles produced in the collision. The ionized electrons drift to both end plates due to the applied electric field. The readout measures the 2D position (x,y) as a function of time. Since the drift velocity and the time is known, a third axis, (z) , can be constructed to extract 3D tracking. What is seen in the xy plane is a momentum-dependent curved track (due to an applied magnetic field along the z -direction). The readout chambers employ a scheme of wires where the charged particles go through. These wires include a grid of anode wires above the pad plane, a cathode-wire grid, and a gating grid. All wires run in the azimuthal direction perpendicular to the beam axis.

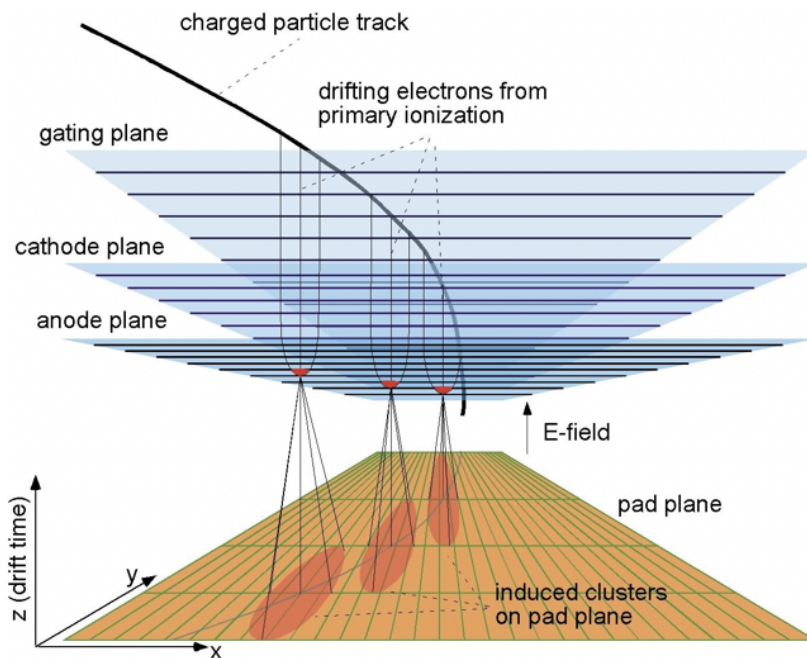


Figure 3.6: Charge particle track drifting to readout. Figure taken from [57].

Fig. 3.6 shows a schematic of the charge particle track pathway as it passes through the readout chamber. The signal amplification is provided through avalanche effects in the vicinity of the anode wires. The cathode plane separates the drift volume from the amplification region. A large number

of ions produced in the amplification avalanche are collected at the cathode wires. The cathode pad plane formed from the 557,568 pads provides the readout of the signal. The signal is passed to Front End cards for post processing. The control of the signal avalanche is done by the gating grid. The gating grid has an open mode and a closed mode. In the open gate mode, all gating grid wires are held at the same potential, U_G , and they admit electrons from the drift volume into the amplification region. In the closed mode, the gating grid is biased with a bipolar field, $U_G \pm \Delta U$, which prevents electrons from the drift volume from getting into the amplification region. In addition, the closed gate stops ions created in the avalanche processes of previous events from drifting back into the drift volume. The ion leakage from the amplification region is held at $< 10^{-4}$ so that the ion charge density is below the density created by primary ionization.

3.3.3 TPC principle of particle identification

The TPC simultaneously measures the particle's momentum and its specific ionization loss, dE/dx , in the TPC gas. This measurement provides particle identification over a wide momentum range. The dE/dx information for a given track must be extracted from the n_{cl} clusters ($50 < n_{cl} < 160$), which are assigned to the track [54]. Q_{max} and Q_{tot} , respectively, are the maximal charge and total charge of each cluster. If the Q_{tot} is chosen, the TPC signal, $\langle Q \rangle_\eta$, is defined as:

$$\langle Q \rangle_\eta = \frac{1}{m} \sum_{i=1}^m Q_i \quad (48)$$

for $i = 1, \dots, n - 1$ and $m = [\eta n]$. The choice of truncated mean is chosen because the average energy loss is not a good estimator due to the long tail towards higher energy losses in the straggling function. The values of the truncated mean, $\langle Q \rangle_\eta$, follow an almost perfect Gaussian distribution, where the dE/dx resolution, $\sigma_{dE/dx}$, is given by the variance of the Gaussian distribution of $\langle Q \rangle_\eta$. The energy loss is described by the Bethe-Bloch function:

$$\left\langle \frac{dE}{dx} \right\rangle = \frac{4\pi N e^4 Z^2}{m c^2 \beta^2} \left(\ln \frac{2 m c^2 \beta^2 \gamma^2}{I} - \beta^2 - \frac{\delta(\beta)}{2} \right) \quad (49)$$

where mc^2 is the rest energy of the electron, Z is the charge of the projectile, N is the number density of electrons in the traversed matter, e is the elementary charge, β is the velocity of the projectile and I is the mean excitation energy of the atom [54].

The ionization energy loss first falls $\propto 1/\beta^2$, then reaches a minimum at $\beta\gamma \approx 4$. It rises again due to the γ^2 term. This rise is canceled by density effect in the δ parameter. The rise from minimum is due to contribution of more distant particles due to the relativistic expansion of the transverse electric field. The relative ionization plateaus due to fact that the polarization of the medium screens more distant atoms. A pictorial representation of these effects can be found in fig. 3.7.

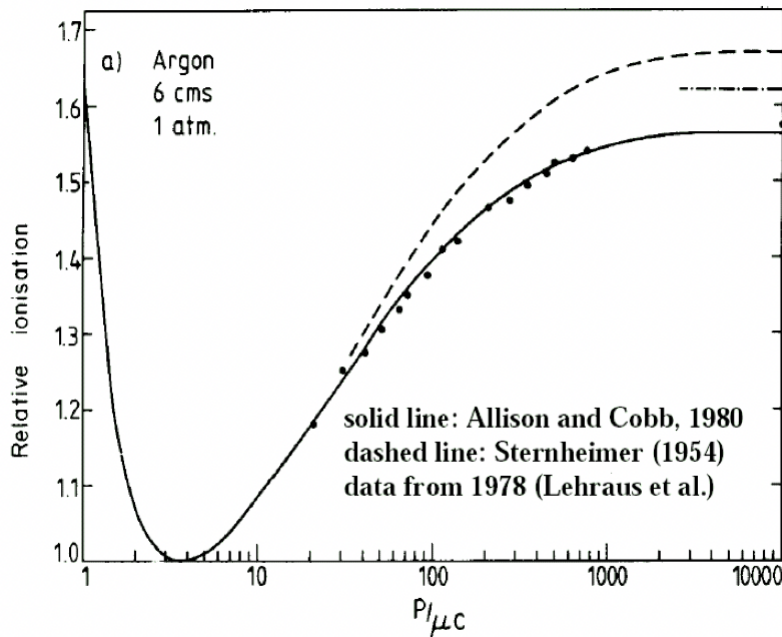


Figure 3.7: Values of ionization in argon at normal density (relative to $\beta\gamma \approx 4$). Note, $\beta\gamma = P/\mu c$, where $\beta = v/c$, $\gamma = (1 - \beta^2)^{-1/2}$, μ , P = mass, momentum of the particle respectively. The data are the points from Lehraus et al (1978), and the dashed line are model predictions from Sternheimer. The solid line is the most probable energy loss in 4.5 cm of pure argon with the PAI model. Figure taken from [58].

The Bethe-Bloch function is a parameterization on the ionization energy loss data. The particle identification is done by considering the difference between the specific ionization energy loss measured by the detector and the corresponding value predicted by the Bethe-Bloch parameterization. This difference is quantified in n_σ , described as:

$$n_\sigma = \frac{(dE/dx)_{measured} - (dE/dx)_{Bethe-Bloch}}{\sigma_{TPC}} \quad (50)$$

Tighter cuts on the n_σ imply a more precise identification of the particle under consideration. The specific ionization energy loss in the TPC as a function of momentum for negatively charged particles: e^- , π^- , K^- , \bar{p} , \bar{d} , \bar{t} , ${}^3\overline{He}$, ${}^4\overline{He}$, as well as the corresponding positively charged particles can be extracted. The e^- and π^- are Minimum Ionizing Particles (MIPs). The specific ionization energy loss of the negative particles mentioned are shown in fig. 3.8.

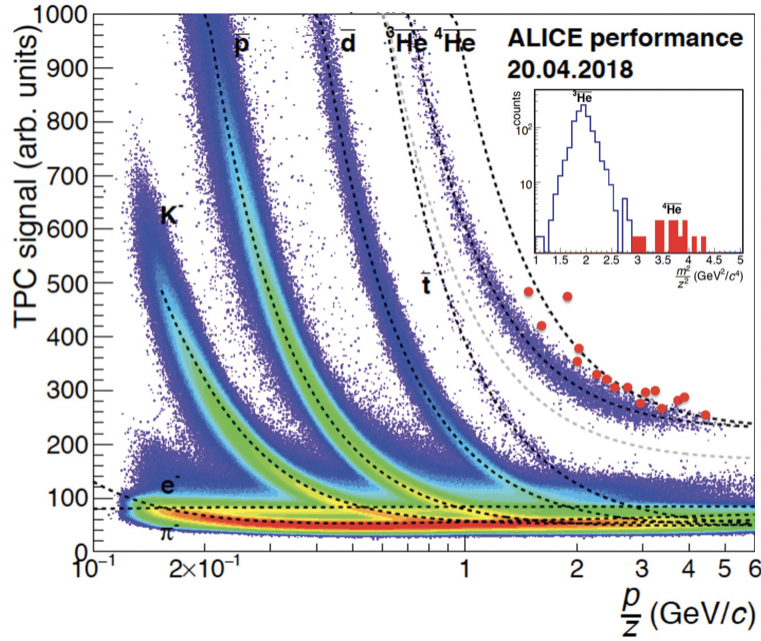


Figure 3.8: Specific ionization energy loss of the negative tracks in the TPC as a function of rigidity in Pb-Pb collisions at $\sqrt{s_{NN}} = 5.02$ TeV. The dashed lines are the parameterization of the Bethe-Bloch function. The inlet shows the mass of ${}^3\overline{He}$ and ${}^4\overline{He}$ after combining TPC and time-of-flight (TOF) measurements. Figure taken from [55].

3.4 V0 particle identification

The track of a weakly decaying neutral hadron into two electrically charged daughters will have a characteristic V0 shape. The V0 is associated with a secondary vertex some distance away from the primary vertex where the V0 originates. The V0 can be reconstructed from its secondary vertex and charged daughters by applying so-called topological cuts. The topological variables are distances in space. Limits on the distances can be placed to reconstruct the desired V0. In the case of the Λ and the $\bar{\Lambda}$, its daughters are p, π^- and \bar{p}, π^+ respectively. The Λ particle has two main decay channels, which are [59]:

$$\Lambda \rightarrow p + \pi^- \quad BR : 63.9 \pm 0.5\% \quad (51)$$

$$\Lambda \rightarrow n + \pi^0 \quad BR : 35.8 \pm 0.5\% \quad (52)$$

A schematic of the Λ charged mode (Eq. 51), used in this analysis is shown in fig. 3.9. A brief description of the Distance of Closest Approach (DCA) topological variables used in reconstructing the Λ particle is summarized in table 3.2. Not used in the analysis is the Λ decay length, $L = c\tau = 7.86$ cm. L is the distance it takes for 50 % of the lambdas to decay, assuming they travel at the speed of light. Other choices of cuts used in reconstructing the Λ and $\bar{\Lambda}$ particle are the V0 radius, and its cosine of pointing angle, which is the angle between the V0 momentum and the V0 line of flight. The maximum value of the cosine of this angle is 1, indicating that the V0 momentum overlaps completely with the line of flight.

Relevant to the reconstruction of weakly decaying mothers from their daughters is the invariant mass. The invariant mass of a V0 candidate is determined from the V0 daughters four-momenta (E, \vec{p}) as:

$$m_{v0} = \sqrt{(E_1 + E_2)^2 - (\vec{p}_1 + \vec{p}_2)^2} \quad (53)$$

where \vec{p}_1 and \vec{p}_2 are the momenta of daughter particles and $E_i = \sqrt{m_i^2 + p_i^2}$ is the energy of daughter particle $i = 1, 2$. The mass of the Λ and $\bar{\Lambda}$ particle is 1115.638 ± 0.006 MeV/ c^2 [59].

Topological variable	Purpose of topological variable
DCA_{V0-PV}	Requires that V0 comes from PV within uncertainties
$DCA_{p-PV} / DCA_{\pi-PV}$	Remove tracks from the PV not belonging to V0
$DCA_{p-\pi}$	To find daughters from the same V0

Table 3.2: A description of topological variables for Λ and $\bar{\Lambda}$ reconstruction.

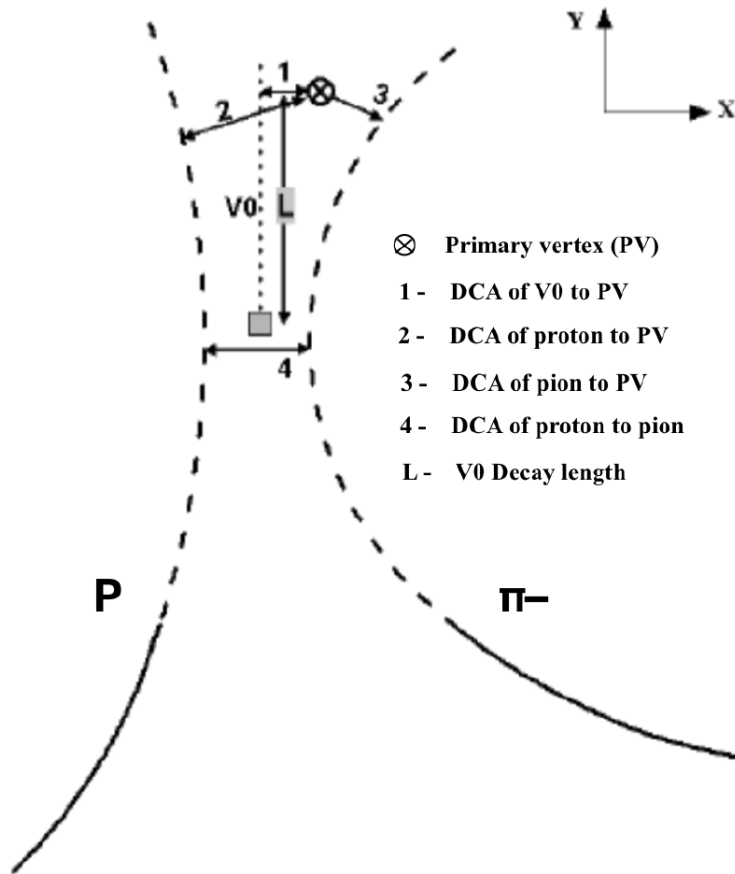


Figure 3.9: A schematic of the Λ decay topology and its Distance of Closest Approach (DCA) choices.

3.5 VZERO Detector

The VZERO detector (not to be confused with the V0 topology), is a pair of ring-segmented scintillator detectors oriented around and perpendicular to the beam axis. These are asymmetrically spaced from the interaction point (I.P.). VZERO-A is located in the positive pseudorapidity direction: $2.8 < \eta < 5.1$ while VZERO-C is in the negative pseudorapidity direction: $-3.7 < \eta < 1.7$.

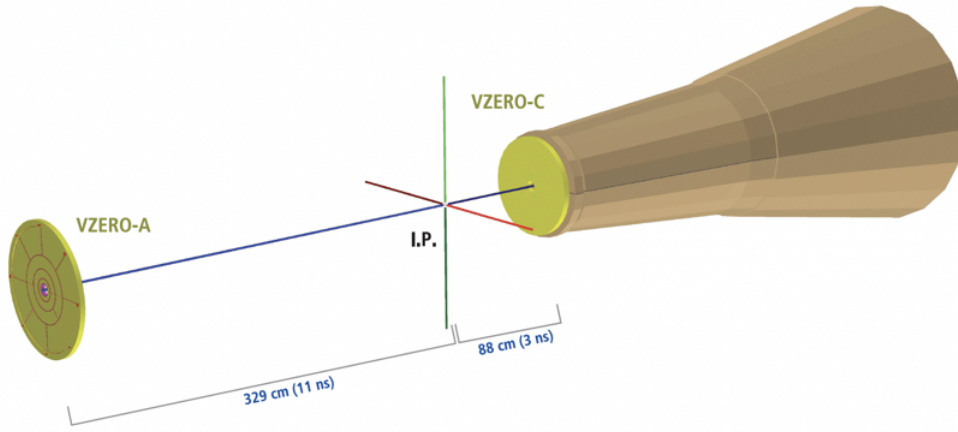


Figure 3.10: A schematic of the VZERO detectors and their distances from the interaction point.

The atoms of the scintillating material are ionized, which release surplus energy by emitting scintillation photons. The number of emitted photons is proportional to energy deposit of the charged particle. The photons go through photo multiplier tubes that amplifies their signal, which is read out by the VZERO front-end electronics. A schematic of the pair of scintillating detectors and their distance from the interaction point is shown in fig. 3.10. The VZERO works on the basic principle that all charged particles give the same average response because they travel at the same $\beta = \frac{v}{c} \approx 1$, which gives a total signal that is correlated with the number of particles (multiplicities) in the detector. The VZERO response amplitude is fitted with a Monte-Carlo simulation of the Glauber Model in order to extract centrality to each Pb-Pb event.

3.5.1 Centrality determination

The collision overlap volume between the two nuclei is related to its transverse distance called the impact parameter, b . During the collision, the number of nucleons of the two Lorentz contracted colliding ions that undergo at least one inelastic collision are called participants, while the non-interacting nucleons are called spectators. The impact parameter measures the degree of overlap in the colliding ions. It is a 2D vector perpendicular to the axis that goes through the center of the two colliding ions. Therefore, as the impact parameter increases, the degree of overlap decreases. Similarly, collisions with the largest collision volume have the smallest impact parameter and highest density. The centrality can be qualitatively inferred from the impact parameter—that is, the most central collisions have the smallest value of the impact parameter and most peripheral collisions have the largest value of the impact parameter.

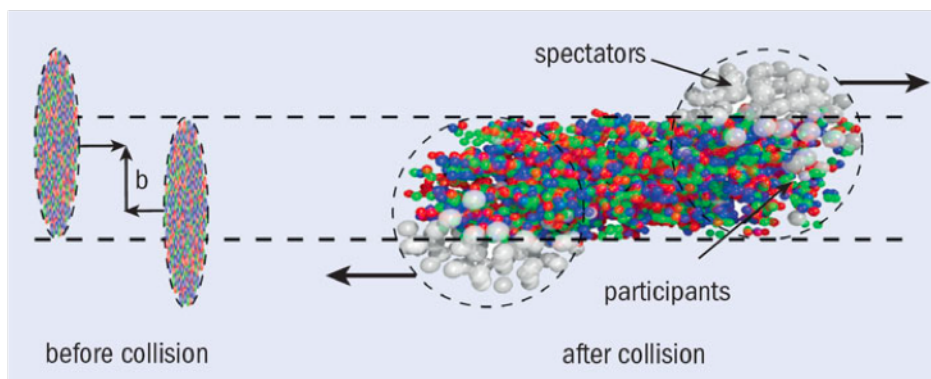


Figure 3.11: A schematic of the two Lorentz contracted ions before and after the collision. The degree of overlap is the impact parameter, b . Figure taken from [60].

Fig. 3.11 shows a schematic of the Lorentz contracted ions before collision and after the collision. It is from the matching of the VZERO amplitude (multiplicities) with the Glauber Model, which is associated with the collision geometry, that the centrality profiles can be quantitatively extracted. The Glauber Model describes the collision geometry by a nuclear density profile, commonly known as the nuclear thickness function, T_{AA} [61]. The nuclear thickness function is extracted by scaling

the number of binary nucleon-nucleon collisions, N_{coll} , to the inelastic nucleon-nucleon cross section, σ_{NN}^{inel} . The centrality bins are defined by integrating from high to low VZERO amplitude, which are expressed as the percentile of the overall hadronic cross section. So that for 0-5 % centrality, its centrality bin contains 5 % of all events with the largest multiplicity. And correspondingly, the 90-100 % centrality bin consists of 10 % of all events with the smallest multiplicity. The data of the VZERO multiplicities fitted with a functional form extracted from the simulation of the Glauber Model for Pb-Pb collision at $\sqrt{s_{NN}} = 5.02$ TeV is shown in fig. 3.12.

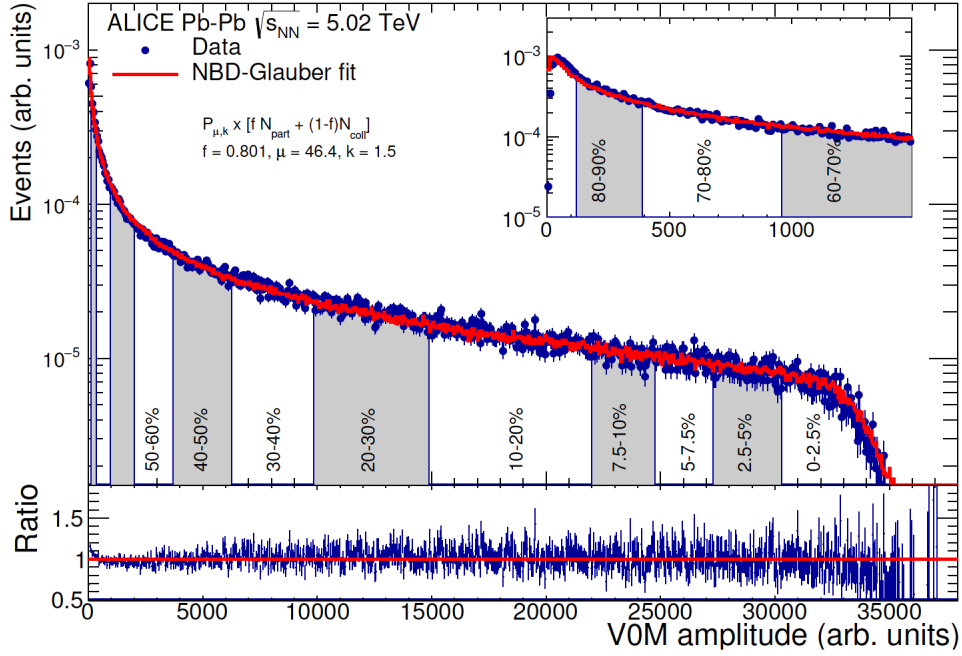


Figure 3.12: Distribution of the sum of the amplitudes in the VZERO scintillators with NBD-Glauber fit shown as the red line. The centrality classes are within the vertical lines. The insert is the distribution for the more peripheral centralities. The ratio plot is the ratio of the NBD-Glauber fit to the data. Figure taken from [61].

Centrality	$dN_{ch}/d\eta$	$\langle N_{part} \rangle$
0 - 2.5 %	2035 ± 52	398 ± 2
2.5 - 5.0 %	1850 ± 55	372 ± 3
5.0 - 7.5 %	1666 ± 48	346 ± 4
7.5 - 10 %	1505 ± 44	320 ± 4
10 - 20 %	1180 ± 31	263 ± 4
20 - 30 %	786 ± 20	188 ± 3
30 - 40 %	512 ± 15	131 ± 2
40 - 50 %	318 ± 12	86.3 ± 1.7
50 - 60 %	183 ± 8	53.6 ± 1.2
60 - 70 %	96.3 ± 5.8	30.4 ± 0.8
70 - 80 %	44.9 ± 3.4	15.6 ± 0.5

Table 3.3: Centrality classes from $dN_{ch}/d\eta$ measured in Pb-Pb collisions at $\sqrt{s_{NN}} = 5.02$ TeV at $\eta < 0.5$. $\langle N_{part} \rangle$ is obtained with the Glauber model. Table adapted from [62].

3.6 Pseudorapidity density of charged particles

The corresponding pseudorapidity density of charged particles, $dN_{ch}/d\eta$, at mid-rapidity in Pb-Pb collisions at $\sqrt{s_{NN}} = 5.02$ TeV is summarized in table 3.3. For the analysis of the data from the Pb-Pb collisions at center of mass energy of 5.02 TeV presented in this dissertation, the first four centrality classes are combined into 1 centrality class. So that the centrality classes used in this analysis are: 0-10%, 10-20%, 20-30%, 30-40%, 40-50%, 50-60%, 60-70%, and 70-80%. The $\langle N_{part} \rangle$ shown in table 3.3 is a geometric property of the collision simulated with an NBD-Glauber fit. Its mean value is obtained from a Glauber Monte Carlo calculation.

4 Statistical distributions, errors, and extraneous fluctuations

There are a few things to consider when determining the distribution that best describes the data. Some relevant characteristics of the data to consider are: if it is symmetric, discrete, and the likelihood of occurrence. The data is the multiplicity of Λ and $\bar{\Lambda}$ produced event-by-event at $\sqrt{s_{NN}} = 5.02$ TeV. The goal is to measure, event-by-event, the net- Λ multiplicity distribution and to characterize that distribution by a probability distribution. The probability distributions are the Poisson distribution and the Negative Binomial distribution. In these distributions, the first two moments of the particle and anti-particle distributions are directly related to the net-particle's second central moment. The statistical errors in the moments are estimated by dividing the data into subgroups in a so-called subgroup method. Details of the statistical error estimation are found in section 4.3.

4.1 The Poisson distribution

The Poisson distribution is a discrete probability distribution that expresses the probability of a given number of occurrences in a fixed interval of time, given that the mean rate of occurrence is known and that the likelihood of occurrence is not dependent on the time since the last occurrence. In particular, the average number of one kind of particle in one event to the next is known, and its occurrence in one event is not affected by the occurrence in the next event. However, there is expectation that the number of one kind of particle in one event to the next will fluctuate around its mean due to limitations caused by experimental acceptance.

Within Poisson statistics, if the average number of one kind of particle from one event to the next is λ , then for the number of occurrences: $k = 0, 1, 2, \dots$, its probability mass function is given by:

$$P_{PD}(k) = \frac{\lambda^k}{k!} \exp(-\lambda) \quad (54)$$

A Poisson distribution can be completely described by its mean, λ . As a result, the cumulants within a Poisson distribution are: $C_n = \lambda$. For two Poisson distributions with mean, λ , for the

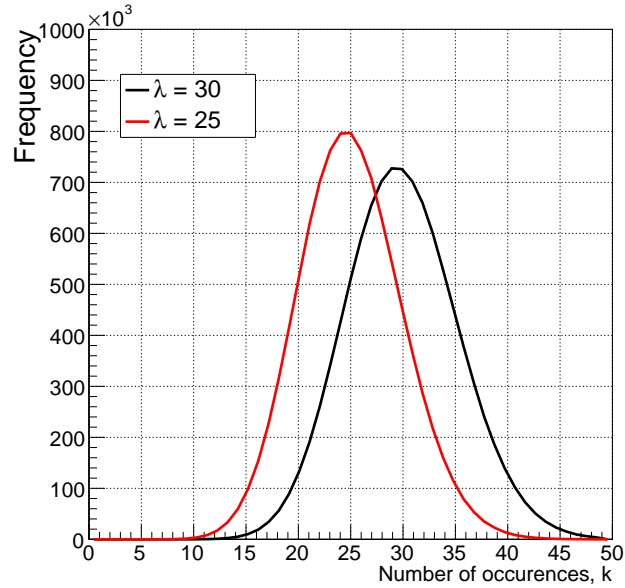


Figure 4.1: Poisson probability distributions as a function of the number of occurrences. λ is the mean number of occurrences, which is also equal to the variance.

particle, and mean, $\bar{\lambda}$, for the anti-particle, the net distribution (also called a Skellam) are: $\lambda - \bar{\lambda}$ for the odd cumulants and $\lambda + \bar{\lambda}$ for the even cumulants. Fig 4.1 shows two Poisson distributions with mean 25 and 30. The figure shows that the mean of a Poisson distribution is equal to its variance.

4.2 Negative Binomial distribution

The Negative Binomial distribution (NBD) is also a discrete probability distribution and it very closely resembles the Poisson distribution. In fact, the NBD converges on the Poisson distribution when the sample size is sufficiently large (see fig. 4.2). The NBD gives the probability for n failures and $k-1$ successes in any order before the k 'th success in a Bernoulli experiment with a success probability p . A Bernoulli experiment is Boolean in nature, that is, it takes the value 1 with probability p , and the value 0, with probability $q = 1 - p$.

The NBD becomes a Poisson distribution for $\frac{1}{k} \rightarrow 0$, i.e., for increasing k . The NBD is defined as:

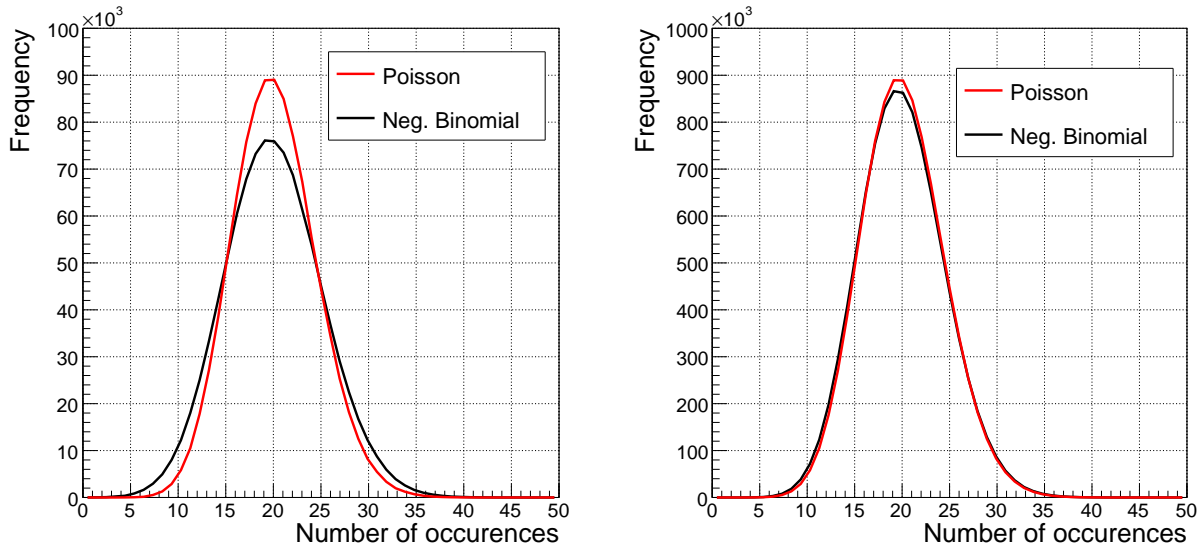


Figure 4.2: Comparison of Poisson and Negative Binomial distributions both centered at 20. The sample size of the left plot is small so the NBD (black line) is more spread out than the Poisson (red line). As the sample size gets larger, the NBD converges on the Poisson (as seen in the right plot).

$$P_{p,k}^{NBD}(n) = \binom{n+k-1}{n} (1-p)^n p^k \quad (55)$$

The mean of the distribution $\langle n \rangle$ is related to p by $p^{-1} = 1 + \langle n \rangle / k$. This leads to the form of NBD that is commonly used to describe multiplicity distributions [63]:

$$P_{p,k}^{NBD}(n) = \binom{n+k-1}{n} \left(\frac{\langle n \rangle / k}{1 + \langle n \rangle / k} \right)^n \frac{1}{(1 + \langle n \rangle / k)^k} \quad (56)$$

However, it is the cumulants or central moments of the multiplicity distributions that are of concern. The cumulants of the NBD distribution can be described by its mean, λ , and variance, σ^2 . If two parameters: α and β are defined as [64]:

$$\alpha = \frac{\lambda}{\sigma^2} \quad (57)$$

$$\beta = \frac{\lambda\alpha}{1 - \alpha} \quad (58)$$

then the cumulants, C_1 and C_2 are:

$$C_1 = \frac{\beta(1 - \alpha)}{\alpha} \quad (59)$$

$$C_2 = \frac{\beta(1 - \alpha)}{\alpha^2} \quad (60)$$

For NBD, the variance is larger than the mean and the cumulants of the net distribution are $C_n - C_{\bar{n}}$ and $C_n + C_{\bar{n}}$ for odd and even cumulants respectively. This is unlike the Poisson distribution, where the mean is equal to the variance. For this dissertation, the Poisson distribution is used to describe the Λ and $\bar{\Lambda}$ multiplicity distributions.

4.3 Statistical errors

The determination of the statistical errors can be acquired through several methods. It can be estimated through bootstrap method, delta theorem method [65], analytically or via the sub-sample method. In estimating the statistical errors in this analysis, the sub-sample method is used. The idea of sub-sampling is to estimate the characteristics of the whole data set with a subset of the data. In estimating the statistical errors of the cumulants with the sub-sample method, the whole data set is divided into number of sub-samples, “ k ”. For each sub-sample, the cumulants are calculated. Let κ_n^i be the n^{th} cumulant of i^{th} sub-sample. The final value of n^{th} cumulant (κ_n) and its statistical error ($\delta\kappa_n$) are estimated as follows:

$$\kappa_n = \frac{\sum_{i=1}^k \kappa_n^i}{k}, \quad (61)$$

$$\sigma(\kappa_n) = \sqrt{\frac{\sum_{i=1}^k (\kappa_n^i - \kappa_n)^2}{k - 1}}, \quad (62)$$

$$\delta\kappa_n = \frac{\sigma(\kappa_n)}{\sqrt{k}} \quad (63)$$

The advantage of using sub-sampling is that there is lower computation cost and faster data collection than performing calculations in the whole data set. For the estimation of the statistical errors of the cumulants in this analysis, 30 sub-samples are used. The data set is on average, 60 million events. Sampling with different values of k showed that estimating the errors on the cumulants was most stable with 30 sub-samples in the different centrality classes (see fig. 4.3). The procedure involves dividing the total number of events into 30 sub-samples randomly, then calculating the respective cumulants in each 1 % centrality bin (the centrality ranges from 1-80 %). As a result, there are 30×80 cumulant errors in each κ_n calculation (Eq. 62) used to evaluate the total error of Eq. 63.

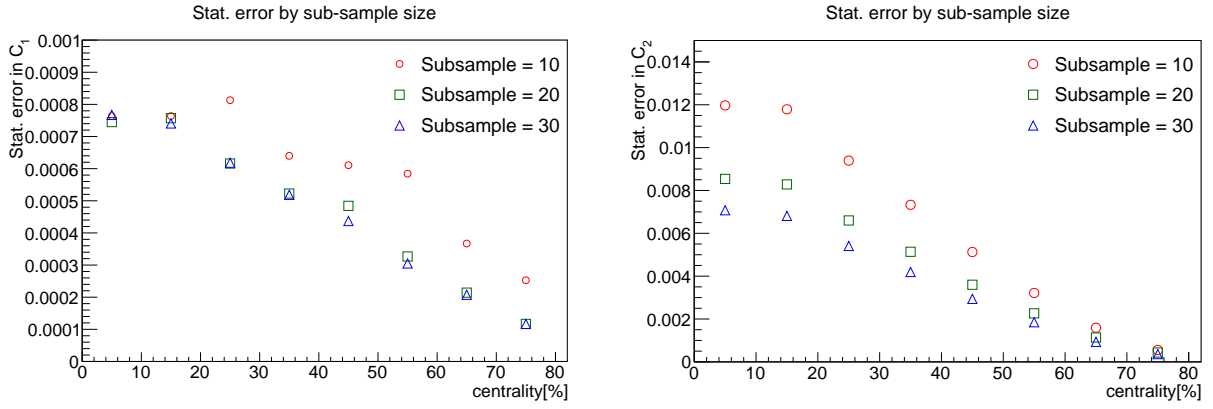


Figure 4.3: Error estimation on κ_n with subsampling method. Note that κ_n and C_n are used interchangeably throughout this dissertation. Shown here are error estimates of the mean (left) and variance (right) of the raw net- Λ multiplicity distribution.

4.4 Induced extraneous fluctuations and conservation laws

There are some effects that can cloud the meaning inferred from the results of the cumulants. On the one hand, calculating the cumulants within centrality classes can induce so-called volume fluctuation effects because centrality is defined by a variable that itself fluctuates. On the other hand, the cumulants can deviate from purely statistical behavior that may lead to interpreting the results as dynamical fluctuations. There are many reasons for the cumulants to deviate from purely statistical behavior, but one important reason is due to the fact that the cumulants are calculated in limited acceptance. The deviation of the cumulants from statistical behavior due to limited acceptance is embodied in the so-called quantum number conservation laws.

4.4.1 Volume fluctuation effects

Since the cumulants are calculated in centrality classes, it is important to check how the centrality binning affects the results. The reality is that the impact parameter, b , from which centrality is determined, fluctuates. This could potentially mask the real fluctuations to be extracted. The effect of extraneous fluctuation due to the impact parameter is called volume fluctuation. The fluctuation of the number of participants within the Wounded Nucleon Model, i.e., the volume fluctuations are typically addressed by performing the analysis in narrow centrality classes. The results are merged afterward in a Centrality Bin Width Correction (CBWC) procedure. In the CBWC procedure, the cumulants are calculated in a narrow centrality bin then the result of the cumulants in the wide centrality bin takes the weighted average. The weight is the total number of events in the narrow centrality bin divided by the total events in the wide centrality bin. The general formula for CBWC is as follows: [66].

$$m_n = \frac{\sum_r n_r m_{n,r}}{\sum_r n_r} \quad (64)$$

where, r is the number of bins within the centrality range under consideration, n_r is the number of events in the r^{th} bin and $m_{n,r}$ is the n^{th} moment measured in r^{th} centrality bin.

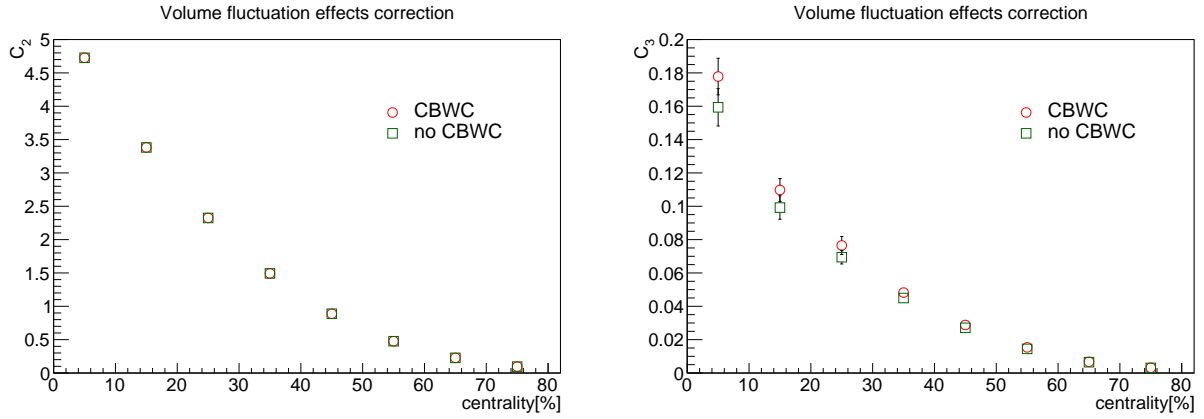


Figure 4.4: Centrality bin width correction (CBWC) of raw C_n of the net- Λ multiplicity distribution. Shown here are with and without CBWC of C_2 (left) and C_3 (right).

The effect of extraneous fluctuations scales with the average net-particle numbers and depends on the probability distribution of the number of participants, which is not known. Experimentally, only the mean number of participants, i.e., its average value over many events can be determined. However, for ultra-relativistic energies, the mean number of produced net-particles vanishes. This implies that the contribution from volume fluctuations in net-particle cumulants is negligible. However, the effects of a volume fluctuations correction become more apparent in the higher cumulants (see fig. 4.4).

4.4.2 Conservation laws

The correlation length in nuclear physics is typically of order $\delta\eta \approx 1$ [67]. Note that the kinematic pseudorapidity correlation length is different from the spatial correlation length, ξ , of the system. The correlation found in fluctuation measurements is linked to dynamical fluctuations. However, such physical correlations can be due to resonance decays or global conservation laws. If an acceptance is chosen, for example, $\delta\eta \leq 0.4$, the smaller acceptance destroys the underlying correlations linked to the main physics under investigation. This ultimately leads to a trivial Poisson multiplicity distribution, thereby eliminating the true fluctuations. The other extreme of choosing a pseudorapidity coverage that is much larger than the natural correlation of the system is that it leads to a sizable contribution to the correlation term as a result of conservation laws. An acceptance threshold can be investigated using models to determine where global conservation laws start to modify the fluctuation measurements.

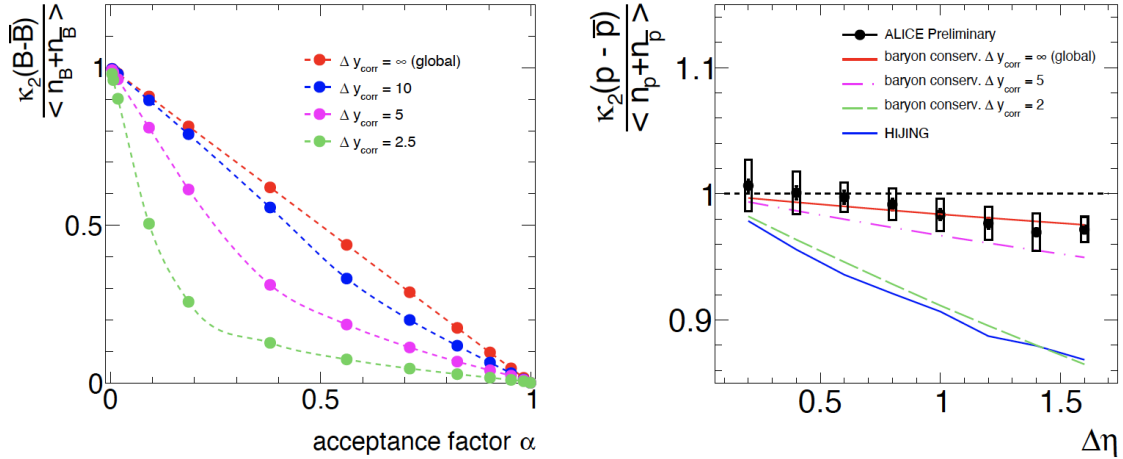


Figure 4.5: Net-protons measured at ALICE compared to models incorporating baryon number conservation. The left panel shows the normalized values of κ_2 of net-baryons for different values of Δy_{corr} , where $\Delta y_{corr} = 2|y_B - y_{\bar{B}}|$. The right panel is the model plotted on the ALICE net-proton fluctuation measurement. Figure taken from [68].

The effect of global and local baryon number conservation laws have been demonstrated in a model [68] [69] in order to describe the pseudorapidity dependence of the second cumulant (κ_2)

of the net-protons measured at ALICE [70] (see fig. 4.5). Shown on the left are the values of κ_2 normalized by the mean number of baryon and anti-baryon versus the acceptance factor, α , in different rapidity windows, Δy_{corr} . Where,

$$\alpha = \frac{\langle n_p \rangle}{N_B^{4\pi}} \quad (65)$$

$$\frac{\kappa_2(p - \bar{p})}{k_2(Skellam)} = 1 - \alpha \quad (66)$$

$$k_2(Skellam) = \langle n_p + n_{\bar{p}} \rangle \quad (67)$$

Eq. 65 is the ratio of the mean number of protons inside the acceptance to the mean number of baryons in the full phase space. Eq. 66 is 1 when $\alpha \rightarrow 0$ and equal to 0 when $\alpha \rightarrow 1$. The two extremes are fluctuation due to Poisson statistics when α is small and no fluctuation when α is very large. Note that the underlying assumption is that the multiplicity distribution follows Poisson statistics, hence it is only defined by its mean. This implies that the ratio of the variance to the mean of a Poisson distribution should be 1. A deviation from unity can be due to the correlation term based on the observation that the variance can be expanded as:

$$\kappa_2(p - \bar{p}) = \kappa_2(p) + \kappa_2(\bar{p}) - 2cov(p, \bar{p}) \quad (68)$$

Where, $cov(p, \bar{p})$ is the correlation term, and is equal to:

$$cov(p, \bar{p}) = \langle N_p N_{\bar{p}} \rangle - \langle N_p \rangle \langle N_{\bar{p}} \rangle \quad (69)$$

The results of the model calculations compared to the experimental data of the net-proton fluctuation measurements at ALICE (right plot of fig. 4.5) show that the subtle correlation present in the κ_2 measurement is due to global baryon number conservation. This is seen directly from the fact that the global baryon number conservation model (red line) matches the $\kappa_2(p - \bar{p})/\kappa_2(Skellam)$ measurement.

5 Analysis Method

Before arriving at the results, there are several procedures involved in analyzing the data. They include —statistical error estimation (see section 4.3), correcting the data for: background, secondaries, and efficiency losses, and testing the correction procedure. The systematic uncertainties are also estimated. A detailed description of these analysis procedures is discussed in this chapter. However, the list of selections used to extract the Λ and $\bar{\Lambda}$ multiplicities precedes the analysis techniques.

5.1 Selections

The type of data and events selected for analysis, the track selections from the TPC, as well as the topological cuts applied on the V0 candidates to extract the Λ and $\bar{\Lambda}$ multiplicity distribution are discussed in this section. The data selection describes what year the data was collected and under which conditions. The event selection describes the subset of events chosen for analysis after some basic cuts. The track selections section lists cuts applied to the tracks from the TPC, and the V0 selection lists topological cuts applied on the V0 candidates.

5.1.1 Data and event selection

The results presented in this dissertation are obtained for the Pb-Pb collision data recorded in 2015 at $\sqrt{s_{NN}} = 5.02$ TeV. There are over 70 million recorded events at this center of mass energy in the minimum bias trigger —that is, events selected with bias as small as possible. A list of the event selection criteria chosen for this analysis is as follows:

- Pile-up event rejection, (done with default cuts in the AliEventCuts class).
- Minimum-bias trigger selection, (done with AliVEvent::kINT7 requested with physics selection).
- Only events whose primary vertex lies within $|z| < 10$ cm are accepted (see left panel of fig. 5.1).

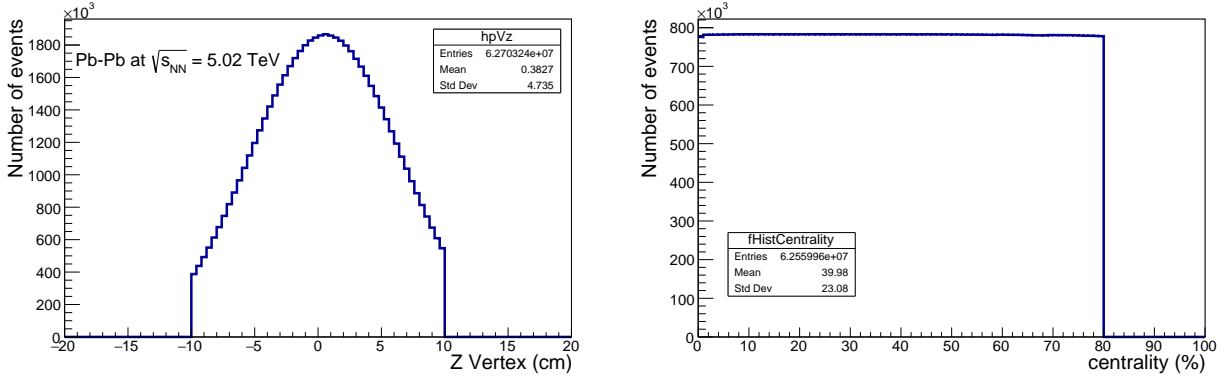


Figure 5.1: Distribution of the vertex Z position with vertex cut at $|z| < 10$ cm (left). Centrality distribution of the selected events (right).

For the event multiplicity selection, the estimator is based on the sum of amplitudes from the VZERO-A and VZERO-C, which are proportional to charge particle counts in the $2.8 < \eta < 5.1$ and $-3.7 < \eta < 1.7$ ranges, respectively. The multiplicity classes used for this analysis are: [0-10], [10-20], [20-30], [30-40], [40-50], [50-60], [60-70], and [70-80]. The right panel of fig. 5.1 shows the centrality distribution of the selected events, which is about 62 million events selected for analysis.

5.1.2 Track selection

In reconstructing the Λ and $\bar{\Lambda}$ particles, it is important to select quality daughter tracks. The selections on the daughter tracks can be found in table 5.1. An explanation of the various selections in table 5.1 (with both daughters within the pseudorapidity interval: $|\eta| < 0.8$), is as follows:

- **TPC dE/dx :** The energy loss measurement from the TPC is used to identify charged tracks. A V0 candidate is chosen if its daughter tracks are within 3σ from the expected energy loss for the correct particle species.
- **Daughter Track $N_{crossedrows}$:** The V0 daughter tracks are required to use information from at least 80 crossed rows in the TPC.
- **Daughter Track $N_{crossedrows}/N_{findable}$:** The V0 daughter tracks are required to have crossed

Selection	Λ and $\bar{\Lambda}$
Daughter Track Pseudorapidity Interval	$ \eta < 0.8$
TPC dE/dx Selection	$ n\sigma < 3$
Daughter Track $N_{crossedrows}$	> 80
Daughter Track $N_{crossedrows}/N_{findable}$	> 0.8

Table 5.1: A summary of daughter tracks selection for Λ and $\bar{\Lambda}$.

rows to findable clusters ratio of at least 0.8.

The plots of fig. 5.2 show the TPC signal for the positively and negatively charged tracks. At this point, no selection has been made specifically for protons and pions. The flat red curve as a function of momentum in the TPC dE/dx plots are the pions or electrons. The pions are produced in large numbers and are minimum ionizing particles (MIPs) like the electrons. The number of TPC track crossed rows is plotted in fig. 5.3. An $n\sigma$ cut of < 3 is applied on the selections for p , π^+ , \bar{p} , π^- from the TPC dE/dx positively and negatively charged tracks. These plots are presented in fig. 5.4. The number of pions within the $n\sigma$ cut is larger than that of protons. This is expected because the number of pions measured are larger than the number of protons measured with the ALICE TPC.

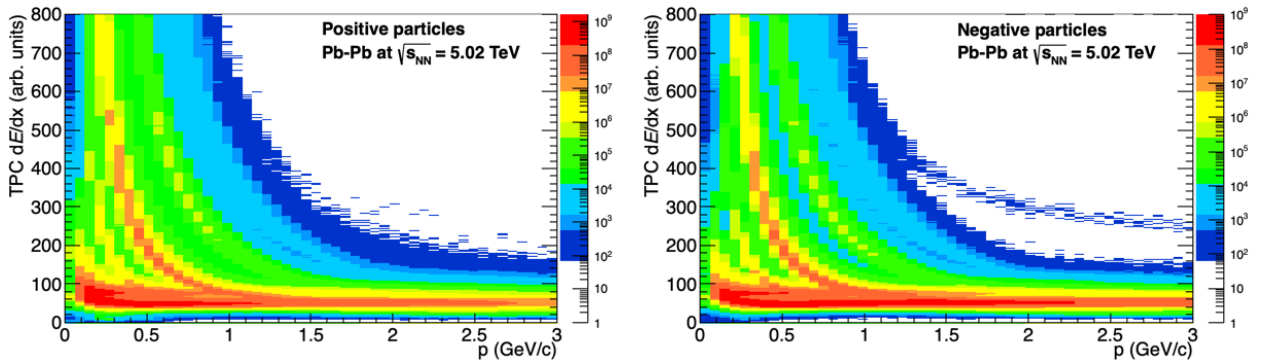


Figure 5.2: TPC dE/dx as a function of momentum in Pb-Pb collisions for the positive (left) and negative (right) tracks.

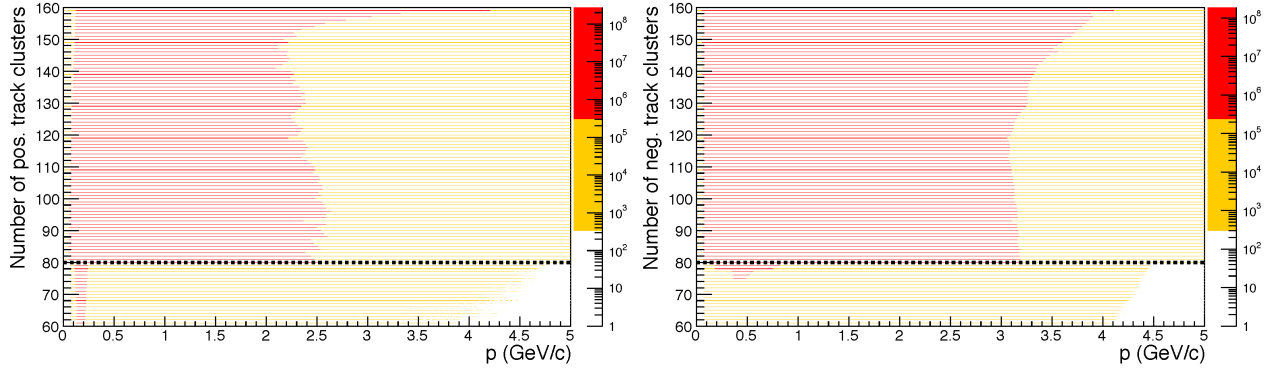


Figure 5.3: Number of positive (left) and negative (right) daughter track crossed rows from the TPC as function of daughter track transverse momentum. The horizontal dashed line indicates a selection for greater than 80 track clusters.

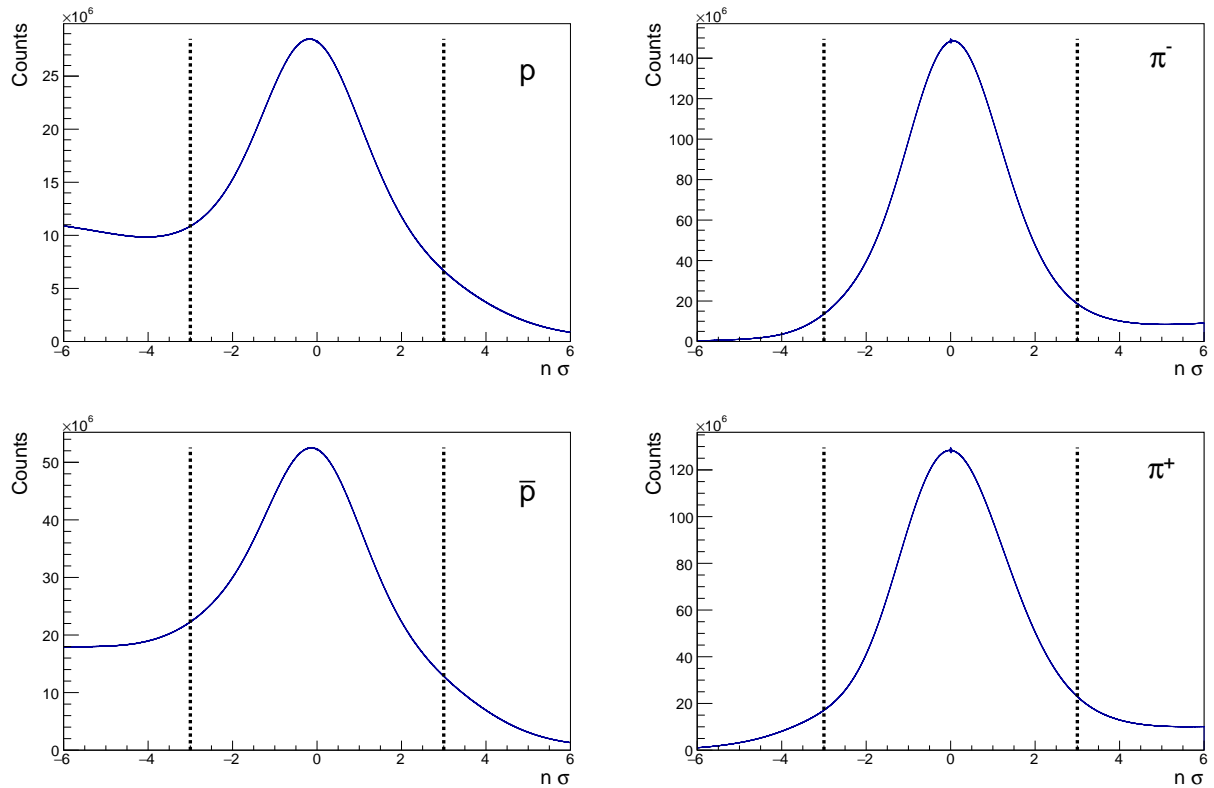


Figure 5.4: TPC dE/dx selection of $|n\sigma| < 3$ on daughter tracks for Λ (p and π^-) and for $\bar{\Lambda}$ (\bar{p} and π^+).

Topological Variable	Λ	$\bar{\Lambda}$
V0 transv. decay radius	> 5.0 cm	> 5.0 cm
DCA Neg. Track to PV	> 0.25 cm	> 0.1 cm
DCA Pos. Track to PV	> 0.1 cm	> 0.25 cm
V0 Cos of Pointing Angle	> 0.99	> 0.99
DCA V0 Daughters	$< 0.8\sigma$	$< 0.8\sigma$
DCA V0 to PV	< 0.25 cm	< 0.25 cm

Table 5.2: Topological selections for Λ and $\bar{\Lambda}$ reconstruction.

5.1.3 V0 selection

An additional set of geometrical requirements is applied on the Λ and $\bar{\Lambda}$ candidates to ensure that the tracks are configured in space in a manner that is consistent with the expected V0 decay topology. These are the so-called topological selections and are shown in table 5.2. An explanation of these types of selection were discussed in section 3.4. A plot of the V0 cosine of pointing angle and different topological variables for the Λ and $\bar{\Lambda}$ candidates are shown in figures 5.5 and 5.6 - 5.8 respectively. The maximum value of cosine of pointing angle is 1 and it is the angle between the V0 line of flight and momentum.

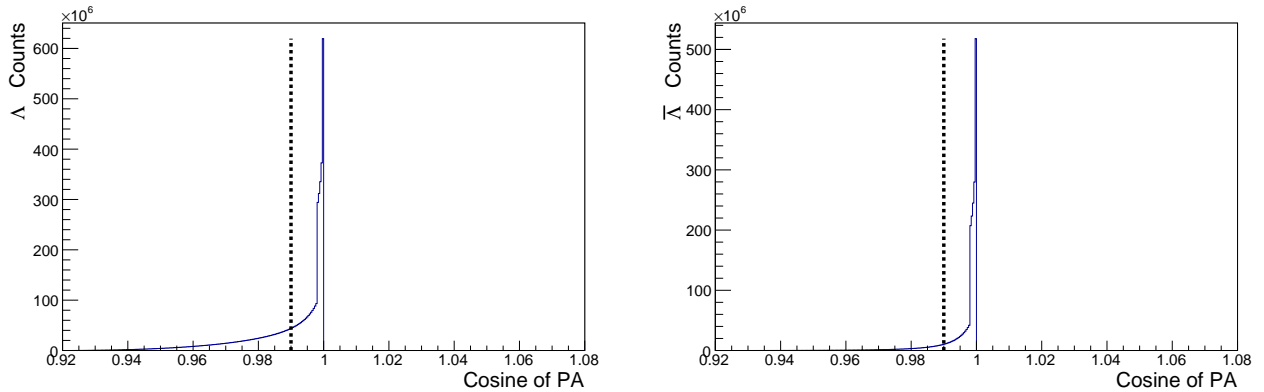


Figure 5.5: Cosine of pointing angle selection of > 0.99 for Λ (left) and $\bar{\Lambda}$ (right).

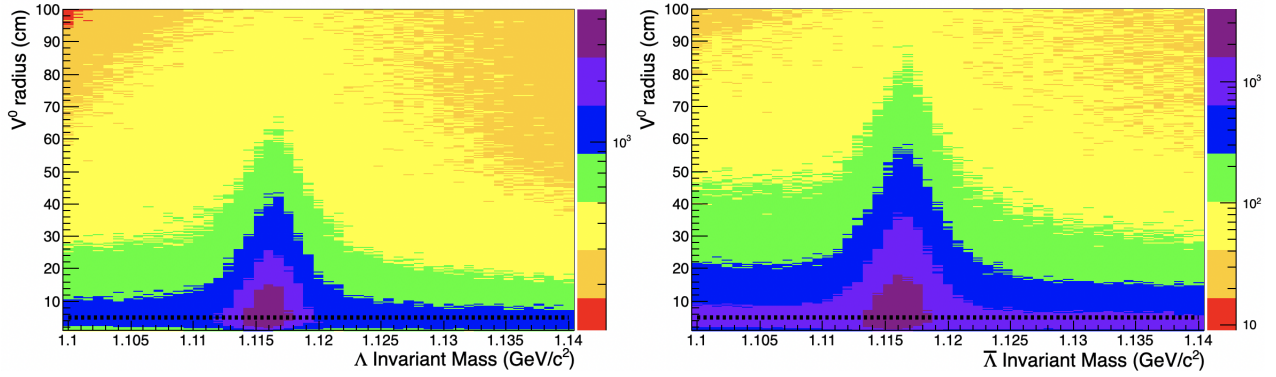


Figure 5.6: The V^0 radius versus Λ (left) and $\bar{\Lambda}$ (right) invariant mass. A selection of greater than 5 cm is chosen to reconstruct the Λ and $\bar{\Lambda}$ candidates.

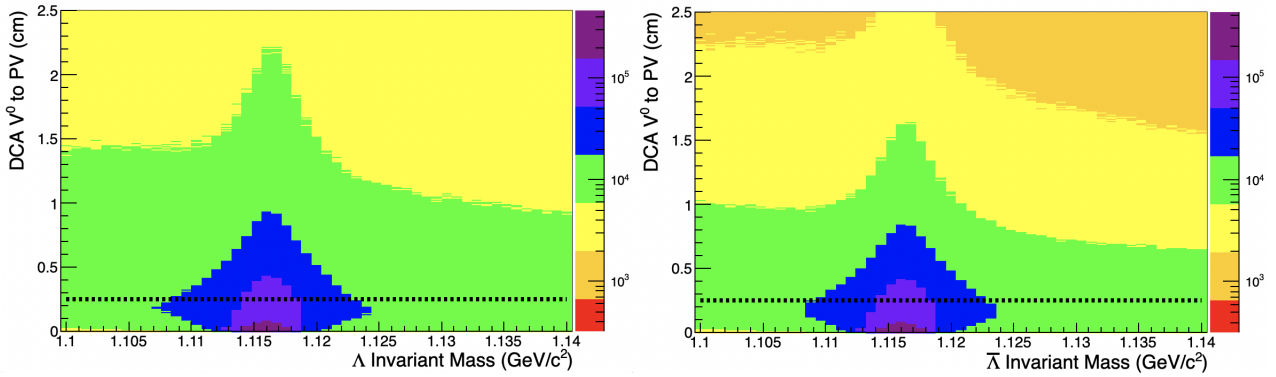


Figure 5.7: Distance of closest approach of the V^0 to the primary vertex versus Λ (left) and $\bar{\Lambda}$ (right) invariant mass. A selection of less than 0.25 cm is chosen to reconstruct the Λ and $\bar{\Lambda}$ candidates.

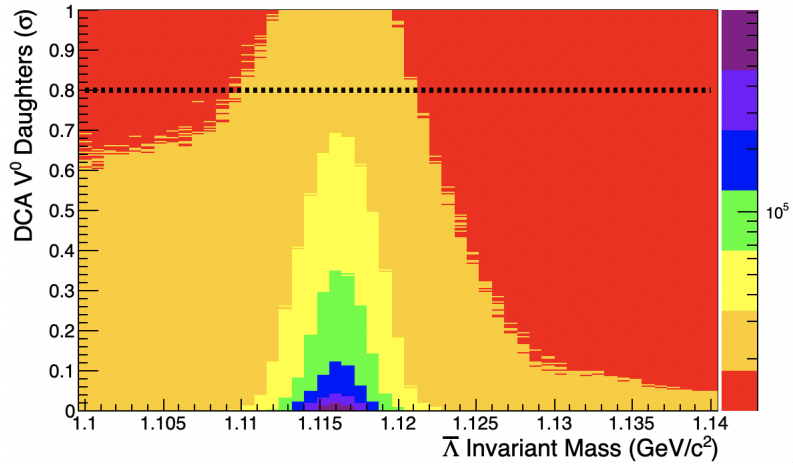
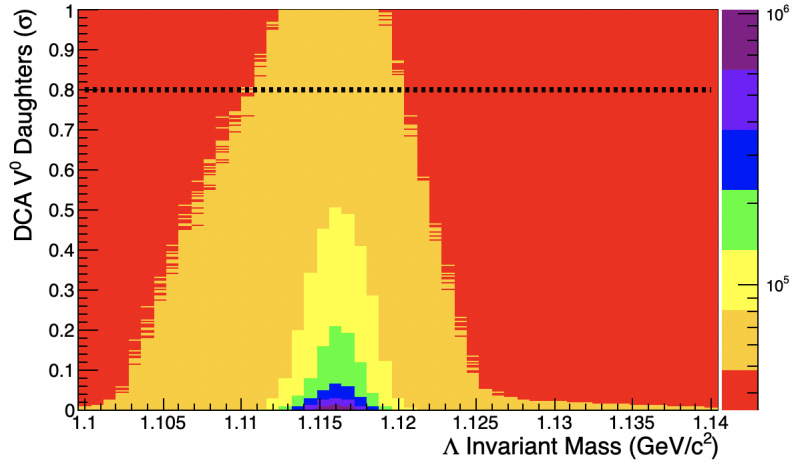


Figure 5.8: Distance of closest approach of the V0 daughters versus Λ (top figure) and $\bar{\Lambda}$ (bottom figure) invariant mass. A selection of less than 0.8σ is chosen to reconstruct the Λ and $\bar{\Lambda}$ candidates.

5.2 Λ and $\bar{\Lambda}$ invariant masses

Signal extraction for Λ and $\bar{\Lambda}$ is performed in p_T intervals: 1.0-2.0 GeV/c with step 0.1 GeV/c, and 2.0-4.0 GeV/c with step 0.2 GeV/c. Using the set of cuts in tables 5.1 and 5.2, the signal was extracted in the following centrality classes: 0-10%, 10-20%, 20-30%, 30-40%, 40-50%, 50-60%, 60-70%, 70-80%. A pseudorapidity cut of $|\eta| < 0.5$ was also applied to the reconstructed Λ and $\bar{\Lambda}$. Fig. 5.9 shows a cut on the pseudorapidity coverage of the Λ and $\bar{\Lambda}$ used for the analysis.

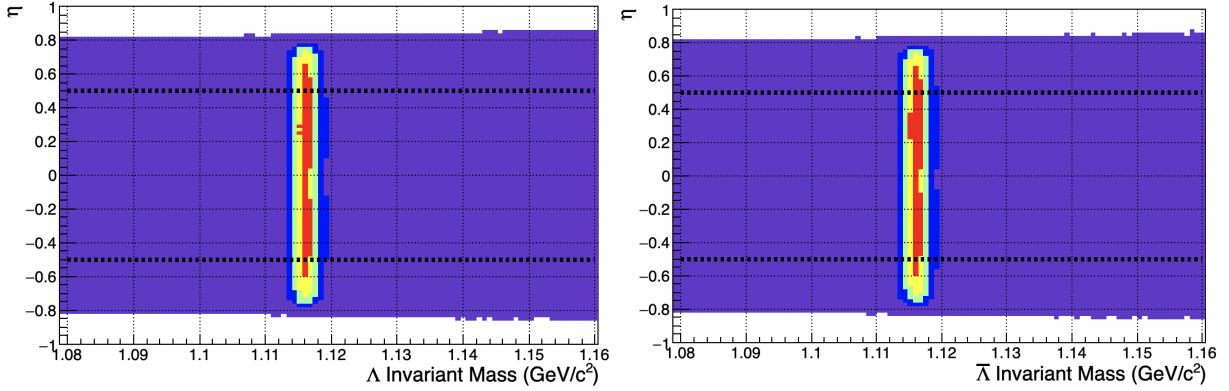


Figure 5.9: Pseudorapidity coverage as a function of invariant mass of Λ (left) and $\bar{\Lambda}$ (right) after track and V0 selections (found in tables 5.1 and 5.2).

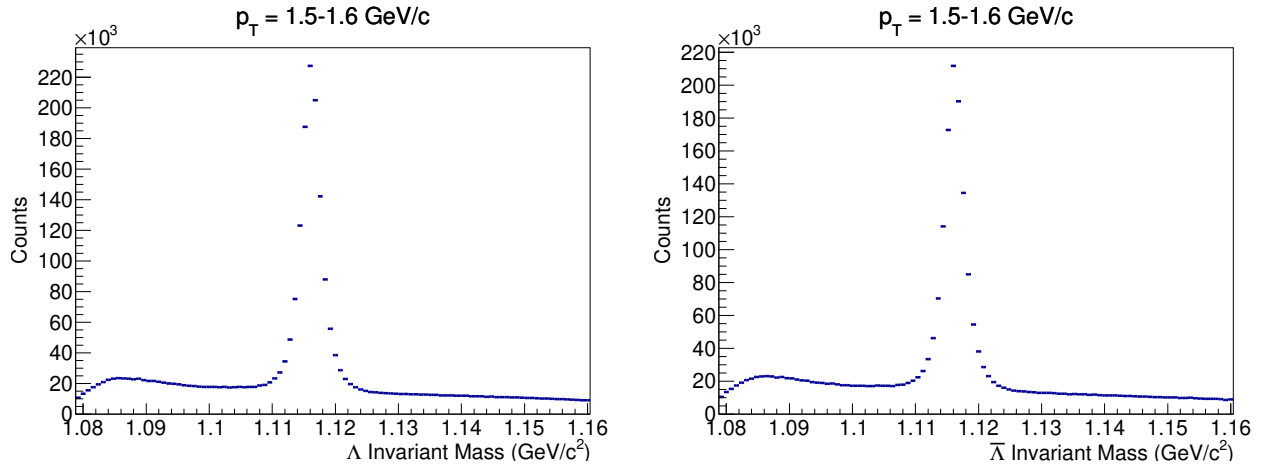


Figure 5.10: Λ (left) and $\bar{\Lambda}$ (right) invariant mass distributions in $1.5 < p_T < 1.6$ [GeV/c] and 0-10 % centrality class.

Fig. 5.10 shows the projected 1D plot of the invariant mass distributions of Λ and $\bar{\Lambda}$ in $1.5 < p_T < 1.6$ [GeV/c] and 0-10 % centrality class.

5.2.1 Background estimation and signal extraction

For each p_T bin in each 10 % centrality bin, the signal was extracted and fitted with a 1st degree polynomial function to estimate the background underneath the invariant mass peak. Fig. 5.11 shows the linear fits of the invariant mass distributions of Λ and $\bar{\Lambda}$ in $1.5 < p_T < 1.6$ [GeV/c] and 0-10 % centrality class. The signal range in which cumulants are calculated lies within: $1.11 < \text{inv. mass} < 1.122$ GeV/c². Fits of the Λ and $\bar{\Lambda}$ invariant masses in the complete p_T range are presented in the appendix.

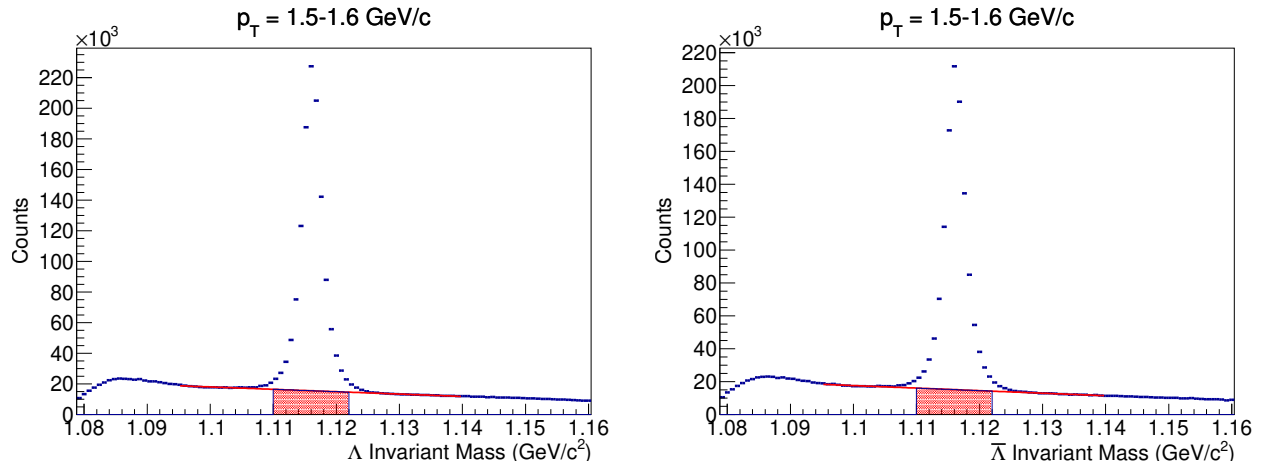


Figure 5.11: Linear fits to Λ (left) and $\bar{\Lambda}$ (right) invariant mass distributions in $1.5 < p_T < 1.6$ [GeV/c] and 0-10 % centrality class.

Centrality	Λ (B+S)	Λ (B)	$B_{frac}(\Lambda)$	$\bar{\Lambda}$ (B+S)	$\bar{\Lambda}$ (B)	$B_{frac}(\bar{\Lambda})$
0-10%	2.21947e+07	2.82415e+06	0.127244	2.09665e+07	2.75222e+06	0.131268
10-20%	1.54987e+07	1.45663e+06	0.093984	1.4645e+07	1.4311e+06	0.0977199
20-30%	1.04619e+07	773593	0.0739441	9.88444e+06	761283	0.0770183
30-40%	6.66562e+06	408200	0.0612396	6.29485e+06	400326	0.0635957
40-50%	3.92308e+06	207845	0.0529802	3.70556e+06	206758	0.0557968
50-60%	2.08389e+06	103161	0.0495039	1.96697e+06	100259	0.0509712
60-70%	983872	51471	0.0523149	925787	50211	0.0542361
70-80%	409419	27544	0.0672772	386726	26147	0.0676116

Table 5.3: Background (B) counts per centrality class within signal range (B+S) for Λ and $\bar{\Lambda}$ in $1.11 < \text{inv. mass} < 1.122$ [GeV/ c^2] and $1.0 < p_T < 4.0$ [GeV/ c].

The fraction of background to the signal region containing both background (B) and the signal (S) is calculated as: $B_{frac} = \frac{B}{B+S}$.

Fig. 5.12 shows a plot of B_{frac} for Λ and $\bar{\Lambda}$. Table 5.3 shows the p_T integrated value in 10% centrality classes for 0 to 80%. From table 5.3 it can be seen that contribution to the background due to fake pairs decreases with decreasing centrality.

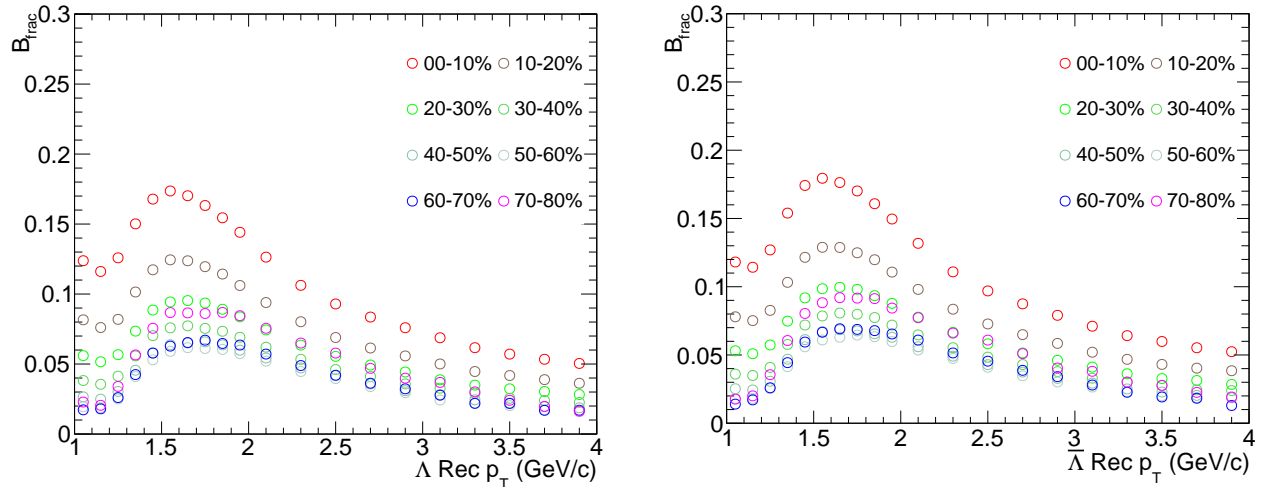


Figure 5.12: Λ (left) and $\bar{\Lambda}$ (right) background fraction versus p_T in 10% centrality classes for 0-80%.

5.2.2 Raw and background corrected Λ and $\bar{\Lambda}$ multiplicities

The raw Λ , $\bar{\Lambda}$, and $\Lambda\bar{\Lambda}$ counts per event in $1.11 < inv.mass < 1.122$ [GeV/ c^2] and $1.0 < p_T < 4.0$ [GeV/ c], as well a background corrected version are shown in fig. 5.13. The background removed multiplicities are corrected by dividing the background plus signal counts (raw) by $1/(1-B_{frac})$ in the respective p_T interval and on an event-by-event basis.

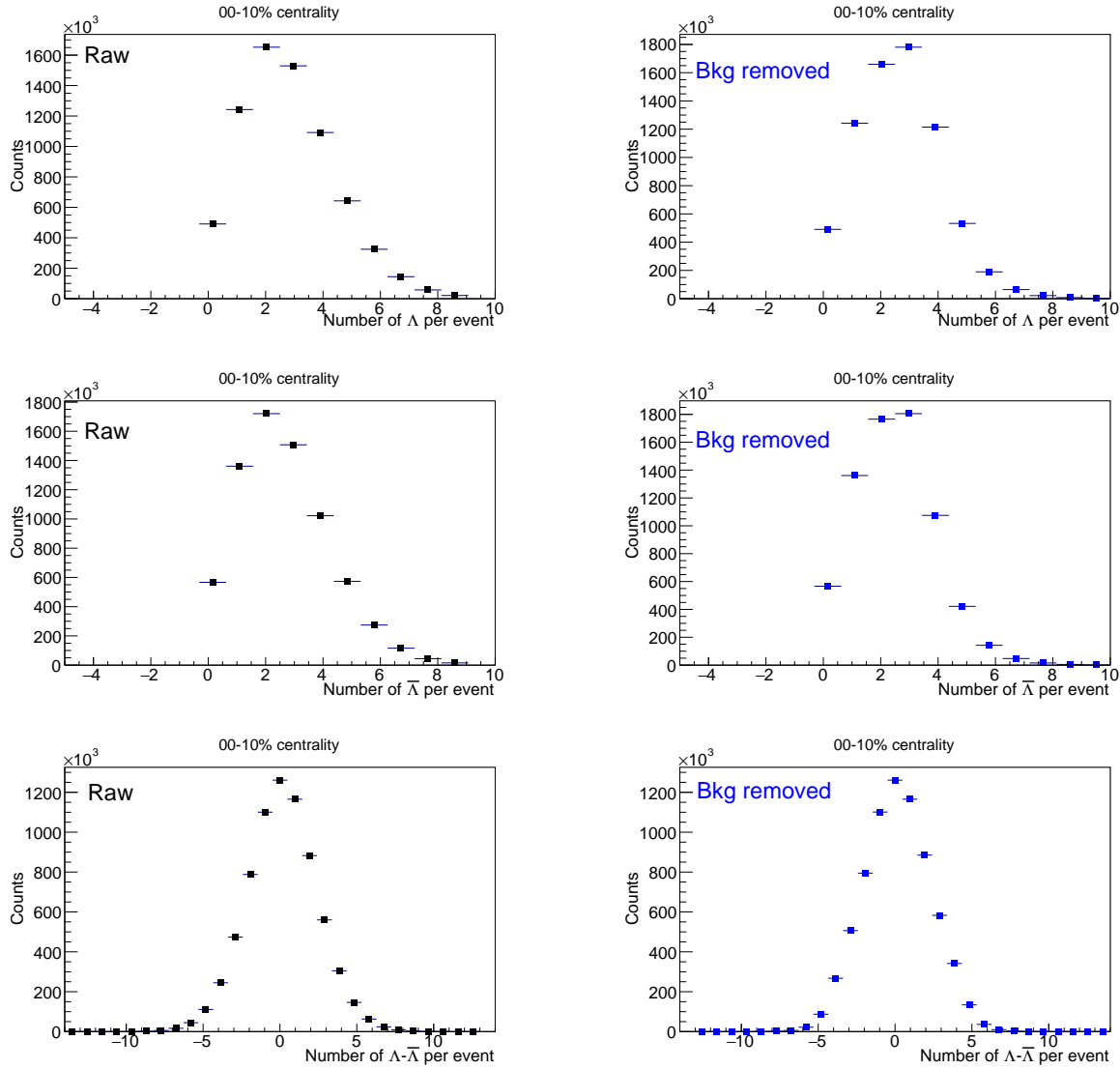


Figure 5.13: Λ , $\bar{\Lambda}$, and $\Lambda\bar{\Lambda}$ multiplicities before and after background correction. Plotted are the counts per event in 0-10% centrality class.

5.3 Monte Carlo correction factors

Reconstruction efficiency of Λ and $\bar{\Lambda}$ is obtained from HIJING events propagated through a GEANT model of the ALICE detector. The feed-down are weak decay contributions to Λ and $\bar{\Lambda}$ from Ξ and Ω baryons. However, since the Ξ baryons are a major contributor to the secondary Λ and $\bar{\Lambda}$, they were selected for feed-down contribution removal. The following channels [59] were considered to be removed from the Λ and $\bar{\Lambda}$ counts:

$$\Xi^- \rightarrow \Lambda + \pi^- \quad BR : 99.887 \pm 0.035\% \quad (70)$$

$$\Xi^0 \rightarrow \Lambda + \pi^0 \quad BR : 99.525 \pm 0.012\% \quad (71)$$

$$\Xi^+ \rightarrow \bar{\Lambda} + \pi^+ \quad BR : 99.887 \pm 0.035\% \quad (72)$$

$$\Xi^0 \rightarrow \bar{\Lambda} + \pi^0 \quad BR : 99.525 \pm 0.012\% \quad (73)$$

5.3.1 Feed-down contribution to Λ and $\bar{\Lambda}$

The feed-down contribution to Λ and $\bar{\Lambda}$ coming from weak decays is computed in the raw counts by using the following expression:

$$\Lambda_{primary}^{raw}(p_{T_i}) = \Lambda_{measured}^{raw}(p_{T_i}) - \sum_j F_{ij} \int_{p_{T_j}} \frac{dN}{dp_T}(\Xi^-), \quad (74)$$

where F_{ij} is the feed-down matrix defined as:

$$F_{ij} = \frac{N_{reco}(\Lambda)_{from \Xi}^{in bin i}}{N_{gen}(\Xi)_{\Xi bin j}} \quad (75)$$

This matrix represents a detection efficiency of secondary Λ in a given p_T bin i coming from the decay of the charged Ξ or neutral Ξ of a p_T bin j . The matrix element is multiplied by the counts of measured Ξ in real data to get the number of secondaries. The counts of Ξ from real data were obtained from the Hagedorn fit of the corrected Ξ spectrum. The Ξ^- and Ξ^+ spectra measured in

the PWGLF-Strangeness PAG at ALICE [72] fitted with a Hagedorn function can be found in the appendix (figures A.5 and A.6 respectively).

The feed-down matrix (Eq. 75) gives the correspondence between the p_T of the mother Ξ and the p_T of the daughter Λ . It is normalized by the total number of generator-level Ξ baryons (Ξ^- for Λ and Ξ^+ for $\bar{\Lambda}$) obtained from HIJING (see fig. 5.14).

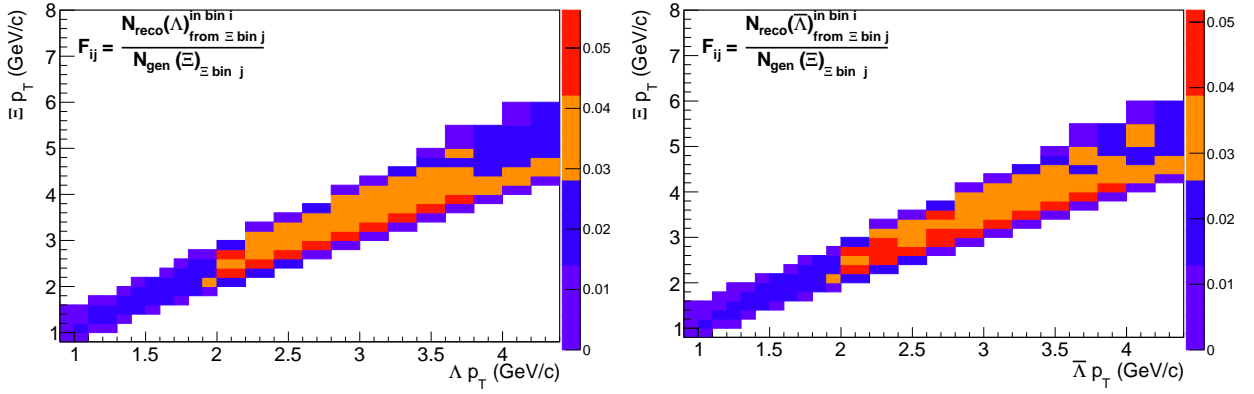


Figure 5.14: Feed-down matrices for Λ and $\bar{\Lambda}$. Left panel: feed-down to Λ includes Ξ^- and Ξ^0 (in numerator). Right panel: feed-down to $\bar{\Lambda}$ includes Ξ^+ and Ξ^0 (in numerator).

The contamination from Ξ decays is defined as:

$$\delta = \frac{N_{sec}}{N_{rec}} \quad (76)$$

Where, N_{rec} is the number of Λ or $\bar{\Lambda}$ counts from real data and N_{sec} is the number of secondaries.

The number of secondaries is obtained with:

$$\sum_j F_{ij} \int_{p_{Tj}} \frac{dN}{dp_T}(\Xi) \quad (77)$$

The number of secondaries contributing to Λ or $\bar{\Lambda}$ and their respective contamination factor, δ , is shown in fig. 5.15.

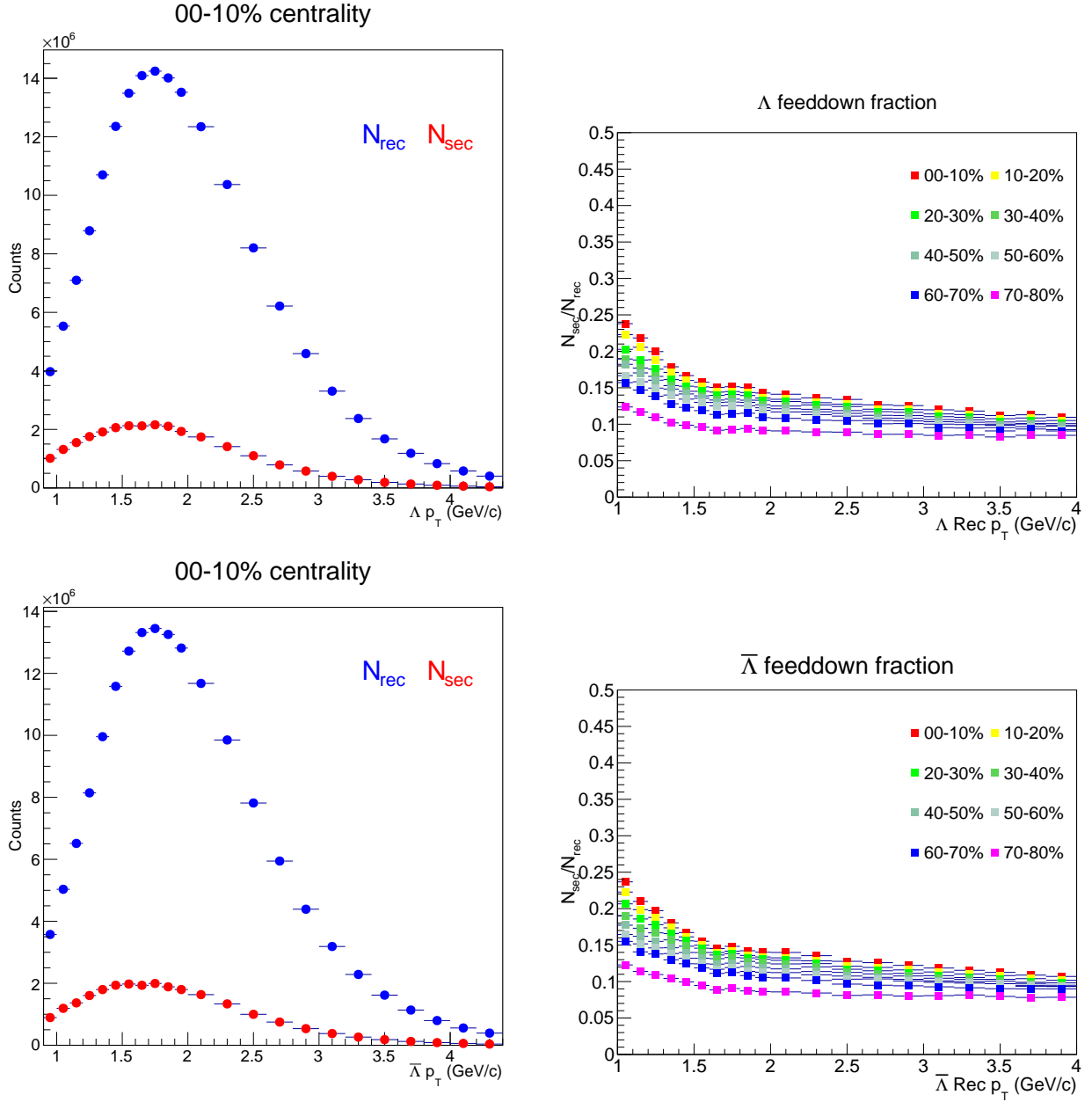


Figure 5.15: Feed-down contribution to Λ and $\bar{\Lambda}$. Left panel: in red is the number of secondary Λ and in blue is the number of all reconstructed Λ (top left figure) in 0-10% centrality class. The bottom figure is the same relationship for $\bar{\Lambda}$. Right panel: the fraction of secondaries for Λ (top right figure) and $\bar{\Lambda}$ (bottom right figure) in all centrality classes.

5.3.2 Efficiency correction

The efficiency correction procedure for fluctuation measurements is dependent on the experiment used to acquire the fluctuation measurements. If the reconstruction efficiencies are very low and have a strong dependence on transverse momentum, p_T , the correction of the second and higher order cumulants become difficult to accomplish. The ratio of the number of primary reconstructed levels to the primary generated levels as a function of p_T and centrality for Λ and $\bar{\Lambda}$ are presented in fig. 5.16.

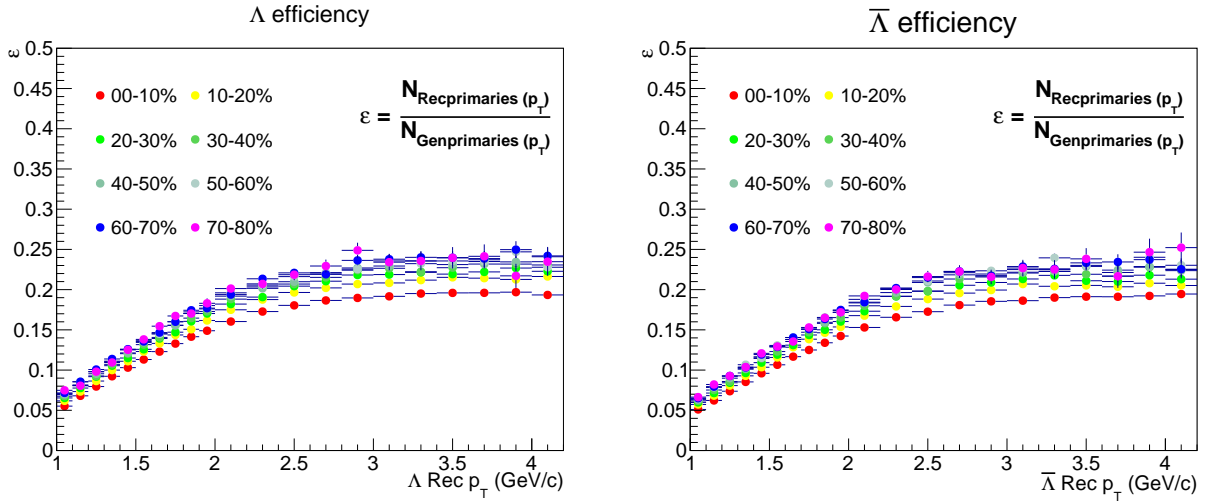


Figure 5.16: Reconstruction efficiencies for Λ (left) and $\bar{\Lambda}$ (right).

A widely used approach in modeling the efficiency losses is by binomial probability distributions [71]. An alternative to that approach is to extract the efficiencies directly from the cumulants of the generated Monte Carlo events propagated through the GEANT model of the ALICE detector. The cumulants from these events are called reconstructed level cumulants. The reconstructed level events contain the cuts applied as in real data, hence they provide an efficiency factor for identical cuts applied in real data. Each reconstructed fluctuation measurement from simulation is divided by the corresponding generated one within the same acceptance. This gives the efficiency correction factor for the specific fluctuation measure. The efficiency correction factor for Λ , $\bar{\Lambda}$ and net- Λ

cumulants follow the form:

$$C_n = \frac{c_n}{\varepsilon_{factor}} \quad (78)$$

Where, the upper case letter, C , stands for the generated level cumulants, the lower case, c , stands for the reconstructed level cumulants from HIJING, and n is the order of the cumulant. The centrality dependence of ε_{factor} specific for the cumulants of Λ , $\bar{\Lambda}$ and net- Λ can be found in fig. 5.17.

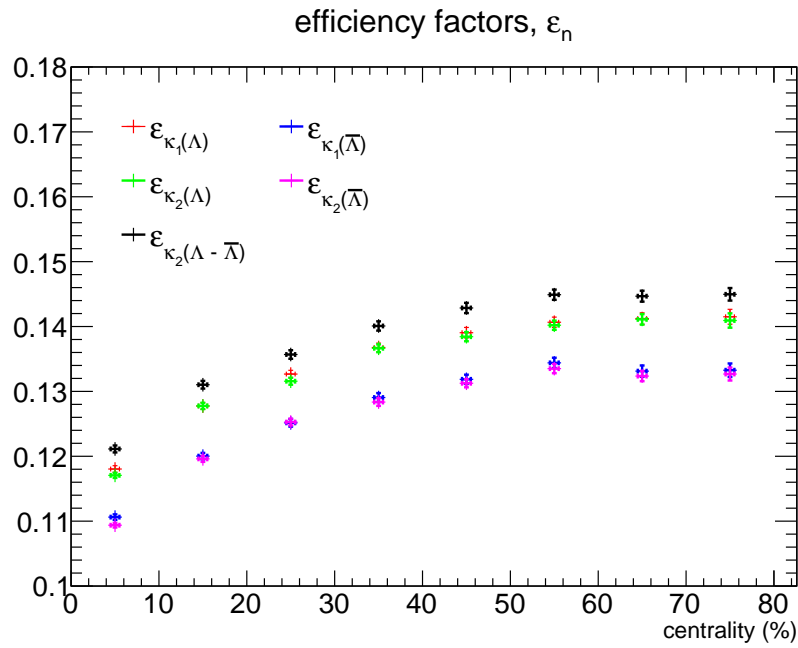


Figure 5.17: Efficiency factors specific for the Λ and $\bar{\Lambda}$ cumulants, κ_n .

5.3.3 MC closure: a test of efficiency correction procedure

To make sure that the correction procedure is under control, it is first tested on the reconstructed cumulants from HIJING. Given that the contribution to the Λ and $\bar{\Lambda}$ counts in real data include background from combinatoric pairs and secondaries from weak decay, the reconstructed counts from HIJING (see fig. 5.18) with the same cuts as in real data are corrected for background and secondaries. After the correction, the results are compared to the generated level in order to pass the so-called Monte Carlo closure test. The test verifies whether the corrected reconstructed cumulants closely matches the generated cumulants.

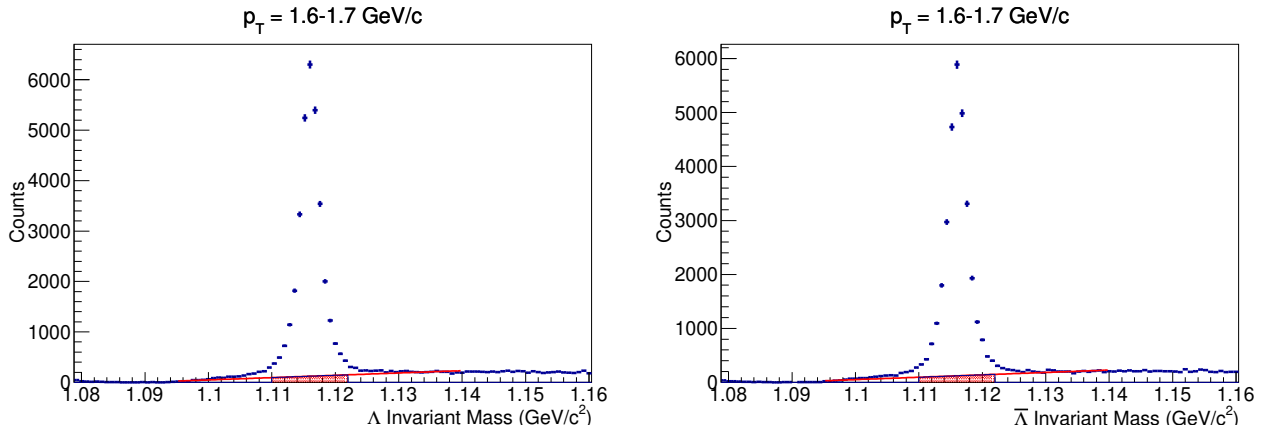


Figure 5.18: Invariant mass of Λ (left) and $\bar{\Lambda}$ (right) from Monte Carlo HIJING in 0-10% centrality class fitted with a polynomial of degree 1 to estimate the background.

The weak decays to Λ and $\bar{\Lambda}$ in simulation data was extracted by tagging the known number of reconstructed level secondaries propagated through the GEANT model of the ALICE detector. Fig. 5.20 shows a plot of the fraction of secondaries in the reconstructed Λ and $\bar{\Lambda}$ from simulation data. The raw cumulants are corrected by scaling with the factor: $\varepsilon/(1-\delta_{sec+bkg})$, where $\delta_{sec+bkg}$ is a sum of fractions of the secondaries and background. In simulation data, the fraction of background and secondaries can be found in figures 5.19 and 5.20 respectively. In real data, the secondaries fraction can be found in the right panel of fig. 5.15 and the background fraction can be found in fig. 5.12. The correction efficiencies are the same for real and simulation data and can be found in fig. 5.17.

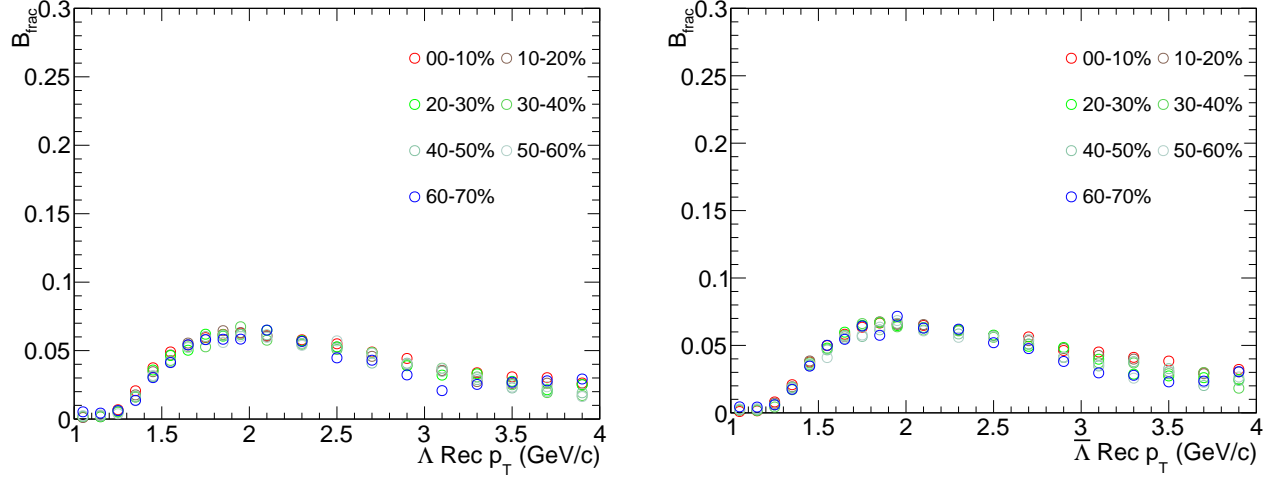


Figure 5.19: HIJING reconstructed Λ (left) and $\bar{\Lambda}$ (right) background fraction, B_{frac} , in all centrality classes. Not shown is the 70-80% class, which had very little entries to fit.

The correction factor: $\varepsilon/(1-\delta_{sec+bkg})$ is extracted from the following:

$$Nrec = Nrecpri + Nsec + Nbkg \quad (79)$$

Where,

$Nrec$ is the total number of particles reconstructed, $Nsec$ is the number of secondary particles (due to weak decays), and $Nbkg$ is the number of particles due to fake pairs (background).

$$\varepsilon = \frac{Nrecpri}{Ngenpri} \quad (80)$$

Where,

$Nrecpri$ is the number of primary reconstructed particles (produced from the primary vertex and not due to weak decays), and $Ngenpri$ is the number of generated particles due to physics (not due to the detector). Substituting Eq. 80 into Eq. 79, then:

$$Nrec = \varepsilon * Ngenpri + Nsec + Nbkg \quad (81)$$

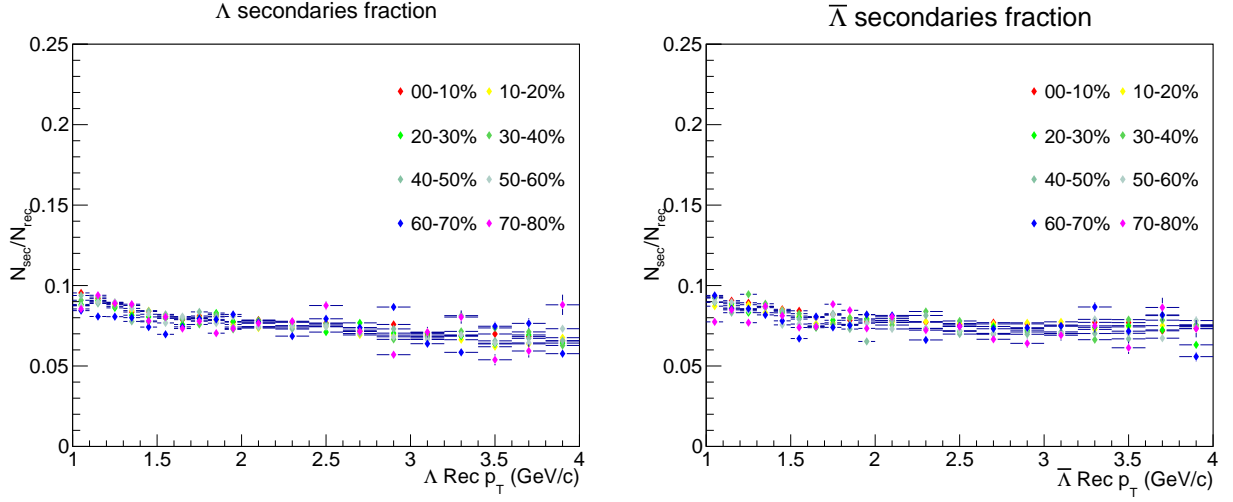


Figure 5.20: Secondaries contribution to reconstructed level Λ (left) and $\bar{\Lambda}$ (right) from Monte Carlo HIJING.

Rearranging,

$$N_{genpri} = \frac{N_{rec} - N_{sec} - N_{bkg}}{\varepsilon} \quad (82)$$

With $\delta_{sec+bkg} = (N_{sec} + N_{bkg})/N_{rec}$ and substituting into Eq. 79, the number of generated primary particles is recovered.

$$\frac{N_{rec} - N_{rec}(N_{sec}/N_{rec}) - N_{rec}(N_{bkg}/N_{rec})}{\varepsilon} = N_{genpri} \quad (83)$$

The number of total reconstructed particles in HIJING were corrected with the factor: $\varepsilon/(1 - \delta_{sec+bkg})$, and then compared to generated primary particles. Fig. 5.21 shows the results of the Monte Carlo closure test for the first and second cumulant from the HIJING Monte Carlo event generator. The results show that within statistical errors, the correction procedure for the reconstructed Λ and $\bar{\Lambda}$ cumulants is consistent with the corresponding generated cumulants. As a result, this correction procedure is used in correcting the reconstructed Λ and $\bar{\Lambda}$ cumulants from real data.

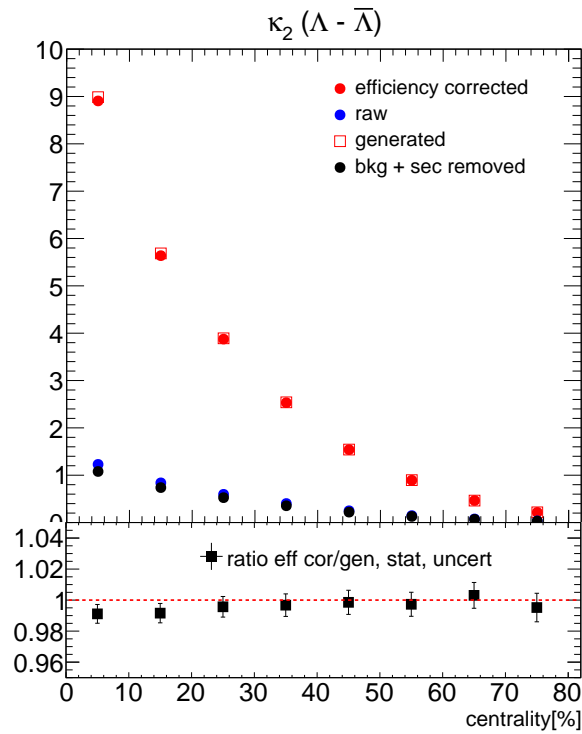
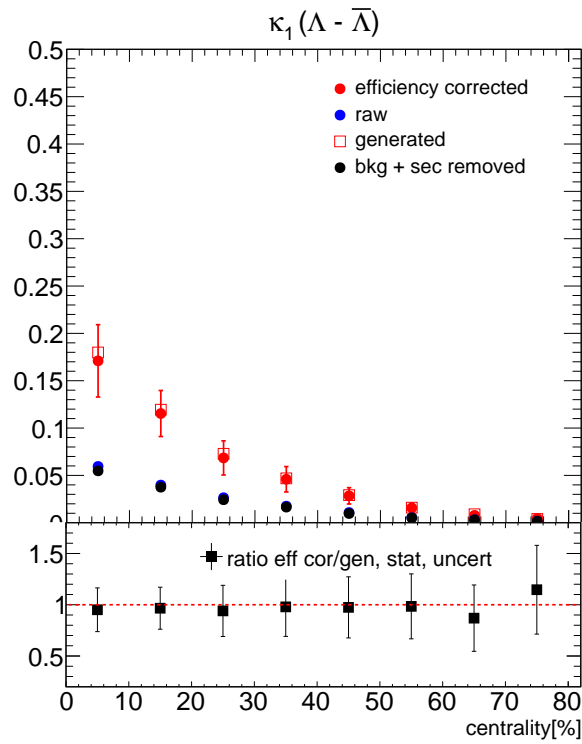


Figure 5.21: Monte Carlo Closure test for the mean (top figure) and variance (bottom figure) of the net- Λ cumulants from HIJING MC event generator.

Uncert. Source	Λ ($\bar{\Lambda}$)	Λ ($\bar{\Lambda}$)	Λ ($\bar{\Lambda}$)
Selections	Loose	Default	Tight
DCA Neg. to PV (cm)	> 0.2 (0.08)	> 0.25 (0.1)	0.3 (0.13)
DCA Pos. to PV (cm)	> 0.08 (0.2)	> 0.1 (0.25)	0.13 (0.3)
TPC dE/dx ($n\sigma$)	< 4	< 3	< 2.5

Table 5.4: Λ and $\bar{\Lambda}$ selection criteria for systematic uncertainty estimation.

Distance to PV (cm)	Λ	$\bar{\Lambda}$
Default	$p > 0.1$ $\pi^- > 0.25$	$\bar{p} > 0.1$ $\pi^+ > 0.25$
Pos loose	$p > 0.08$ $\pi^- > 0.25$	$\bar{p} > 0.1$ $\pi^+ > 0.2$
Pos tight	$p > 0.13$ $\pi^- > 0.25$	$\bar{p} > 0.1$ $\pi^+ > 0.3$
Neg loose	$p > 0.1$ $\pi^- > 0.2$	$\bar{p} > 0.08$ $\pi^+ > 0.25$
Neg tight	$p > 0.1$ $\pi^- > 0.3$	$\bar{p} > 0.13$ $\pi^+ > 0.25$
TPC dE/dx ($n\sigma$)	Λ	$\bar{\Lambda}$
Default	$ n\sigma < 3$	$ n\sigma < 3$
Nsig loose	$ n\sigma < 4$	$ n\sigma < 4$
Nsig tight	$ n\sigma < 2.5$	$ n\sigma < 2.5$

Table 5.5: Explicit description of the total cut variations for Λ and $\bar{\Lambda}$ used to estimate systematic uncertainties in the cumulants.

5.4 Systematic uncertainties

It has been shown in section 4.3 that the statistical errors are due to the sample size, in particular, the number of events used to calculate the cumulants. A different contribution to the errors is due to systematic uncertainties—that is, the error introduced due to the measuring process. Since the Λ and $\bar{\Lambda}$ particle are measured in order to calculate the cumulants, the systematic uncertainty can be estimated by varying the way in which the Λ and $\bar{\Lambda}$ particle are reconstructed. It has been shown in section 3.4 and 5.1.3 that a V0 particle, such as the Λ and $\bar{\Lambda}$ are reconstructed via topological cuts, which fix the V0 in space in a manner consistent with its decay topology. This drives the need to vary the topological cuts—tighter and looser than the default cuts, in order to estimate

the contribution of the errors due to the measuring process.

5.4.1 Selection cuts

All of the investigated sources of systematic uncertainties come from Λ and $\bar{\Lambda}$ topological selection criteria and the TPC dE/dx $n\sigma$ cuts on its daughters. For every criterium in table 5.4, the corresponding parameter value was modified while keeping other parameters to their default values when the signal was extracted (shown explicitly in table 5.5). The deviation from the default value represents the RMS caused by the selection variable. The RMS is calculated as:

$$\text{RMS} = \sqrt{\frac{1}{N} \sum_{i=1}^N (X_i - Y)^2} \quad (84)$$

Where N is the total number of variations, Y is the default value, and X_i are the different cut variations. For the total systematic uncertainty, all maximum deviations are combined in quadrature. It is calculated as:

$$\text{SYS}_{err} = \sqrt{\sum_j \text{RMS}_j^2} \quad (85)$$

Where j is the number of systematic uncertainty sources. Plots of the respective cumulant due to the cut variations of table 5.5 is shown in fig. 5.22.

To get a sense of the effect due to varying the cuts, their individual contribution can be found in table 5.6. The relative uncertainty is the absolute change from the default value, normalized by the default value and multiplied by 100. The total uncertainty of table 5.6 is the sum in quadrature of all the relative errors due to the selections.

Relative Uncertainty (%)						
Selection	$\kappa_1(\Lambda)$	$\kappa_1(\bar{\Lambda})$	$\kappa_2(\Lambda)$	$\kappa_2(\bar{\Lambda})$	$\kappa_2(\Lambda - \bar{\Lambda})$	$\kappa_2(\text{skellam})$
Nsig loose	1.45	1.87	0.25	0.89	1.73	1.66
Nsig tight	1.10	0.69	1.65	1.07	1.06	0.89
Pos loose	0.39	0.78	0.52	0.16	0.55	0.59
Pos tight	0.44	0.80	0.57	0.09	0.49	0.62
Neg loose	0.38	0.79	0.52	0.12	0.54	0.594
Neg tight	0.81	1.16	0.57	0.002	0.42	0.592
Total	1.99	2.56	2.00	1.42	2.27	2.24

Table 5.6: Relative uncertainties on the cumulants due to the different selections. The results are for 0-10% centrality class, $1 < p_T < 4$ GeV/c, and $|\eta| < 0.5$.

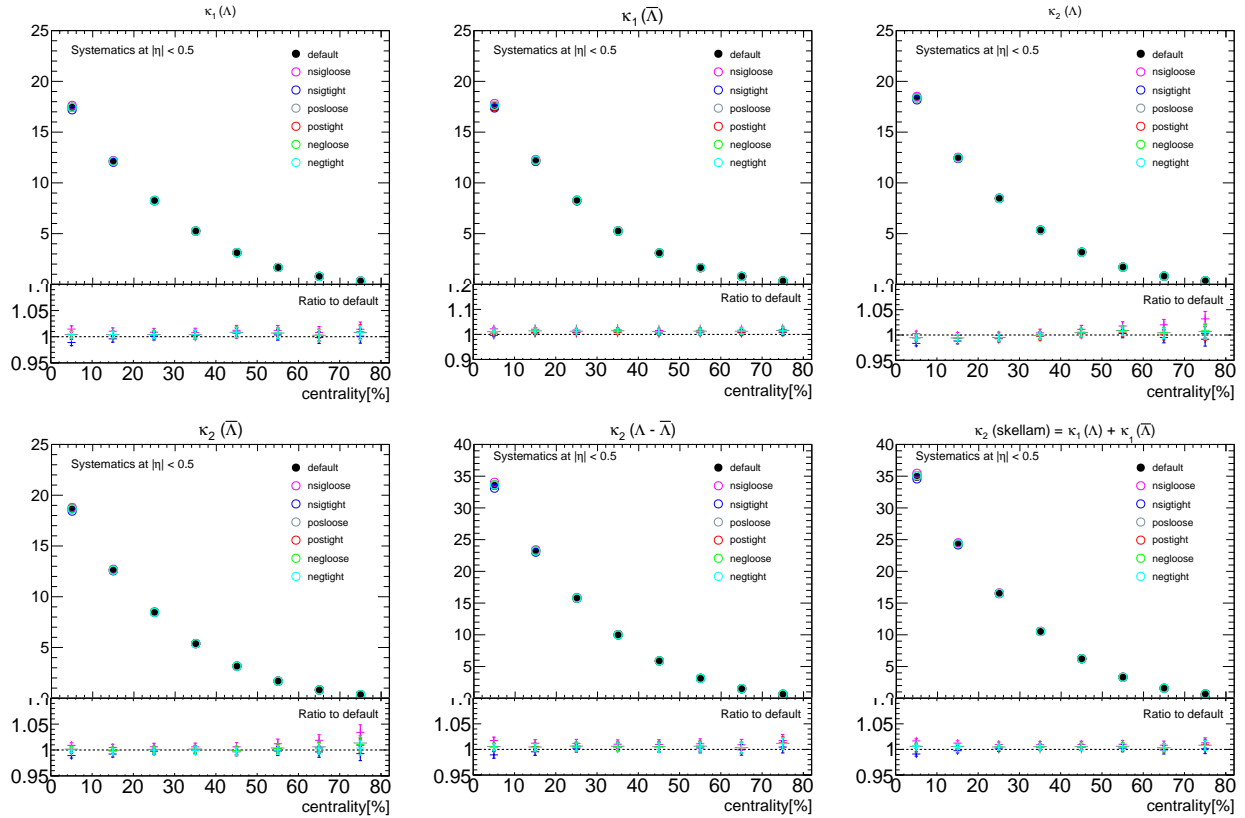


Figure 5.22: Plots of the cumulants based on the selection cuts of table 5.5 (top panel) and their comparison to the default values in the ratio plot (bottom panel).

5.4.2 Final systematic uncertainties

In 0-10% centrality, a plot of the systematic uncertainties due to the topological cut variations considered as one source, and the TPC dE/dx cut variations considered as another source can be found in fig. 5.23. Ultimately, the uncertainties in fig. 5.23 were used as the systematic uncertainties for the cumulants because the topological cuts are correlated and thus, are considered as one source. Fig. 5.23 shows that the major contribution to the systematic uncertainty is the dE/dx $n\sigma$ cut. The dashed black line is the final systematic uncertainties used for the respective cumulants.

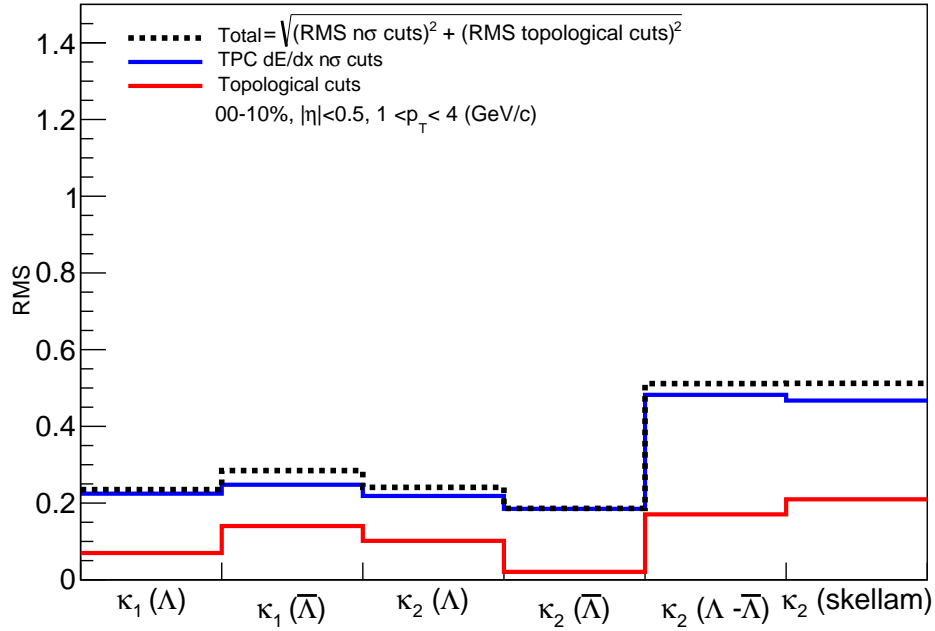


Figure 5.23: Summary of the contributions to the systematic uncertainty to the cumulants for 0-10% centrality class.

The second cumulant of the net- Λ distribution was studied in pseudorapidity ranges different from the default ($|\eta| < 0.5$). Shown in fig. 5.24 are the systematic uncertainties in $|\eta| < 0.3$ and $|\eta| < 0.8$ for $\kappa_2(\Lambda - \bar{\Lambda})$ and $\kappa_2(\text{skellam})$.

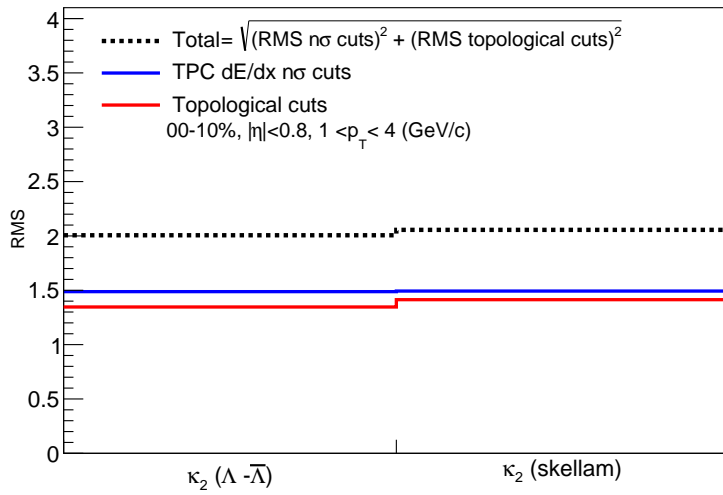
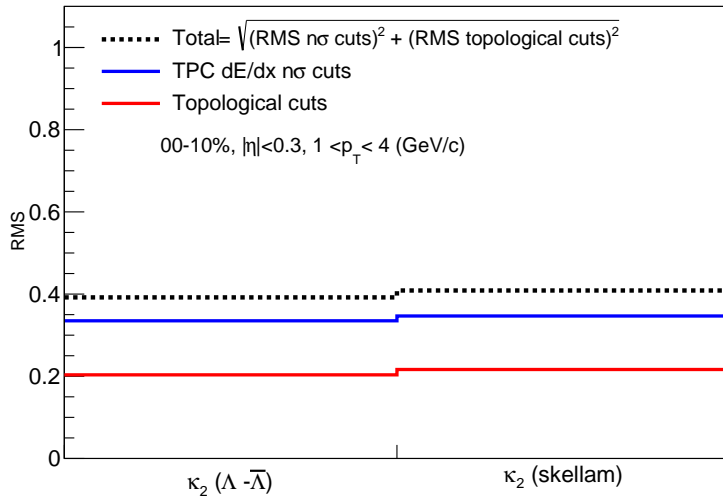


Figure 5.24: Systematic uncertainties in 0-10% centrality class for $\kappa_2(\Lambda - \bar{\Lambda})$ and $\kappa_2(\text{skellam})$ in $|\eta| < 0.3$ (top figure) and $|\eta| < 0.8$ (bottom figure).

6 Results, Discussion, and future directions

The motivation to investigate net-particle multiplicity measurements is to study the phase structure of strongly interacting matter. The event-by-event net-particle multiplicity measurement in a finite acceptance is linked to the susceptibilities of conserved quantities calculated with lattice QCD. The conserved quantities are net-charge, net-baryon number and net-strangeness. Net- Λ fluctuation measurements elucidate the correlated fluctuations of net-strangeness and net-baryon number. There is an interplay between strangeness and baryon number conservation because the Λ particle is a strange baryon, and its fluctuation measurements are acquired in a finite acceptance. The acceptance cut in which the cumulants are calculated is linked to quantum number conservation laws. The results shown in this dissertation are for the first two cumulants of the net- Λ distribution compared with the Poisson probability distribution.

Poisson statistics is based on number of occurrences of a certain event, in this case, the number of Λ and $\bar{\Lambda}$ in an event. If the fluctuation measurements strictly follow Poisson statistics, it can be inferred that the results of the measurement is due to statistics and not due to the true fluctuations under investigation that are linked to the phase structure of strongly interacting matter. Other factors that mask the true fluctuations under investigation are volume fluctuation effects which are corrected for with Centrality Bin Width Correction (CBWC). Section 4.4.1 showed that the effect of volume fluctuation on the cumulants are present for cumulants above the second order. Notwithstanding, CBWC was used in correcting the cumulants presented in this dissertation. In addition, other correction procedures to the Λ and $\bar{\Lambda}$ distribution include: removal of background (section 5.2.1) and weak decays (section 5.3.1), and correction for efficiency losses (section 5.3.2). The chapter begins with results of the raw counts of the first and second cumulant of the Λ and $\bar{\Lambda}$ distribution and ends with the corrected versions. A summary of the results, as well as future directions are discussed in section 6.7.

6.1 Centrality dependence of the raw Λ , $\bar{\Lambda}$ and net- Λ cumulants

The first two raw cumulants, i.e., the mean and variance are presented in this section. The raw counts are the number of Λ and $\bar{\Lambda}$ per event prior to background and weak decay removal. It is the counts per event in Pb-Pb collisions at $\sqrt{s_{NN}} = 5.02$ TeV. Section 5.2.2 showed a distribution of the raw counts per event for 0-10% centrality class, which showed an average number of ≈ 3 per event (in signal region with $\approx 13\%$ background) for the Λ and $\bar{\Lambda}$ distribution. In this section, the average number of the event-by-event Λ and $\bar{\Lambda}$ distribution, i.e., its mean over all centrality classes and the variance are presented. Collision centrality (already discussed in 3.5.1), is a measure of the degree of overlap between the two colliding nuclei.

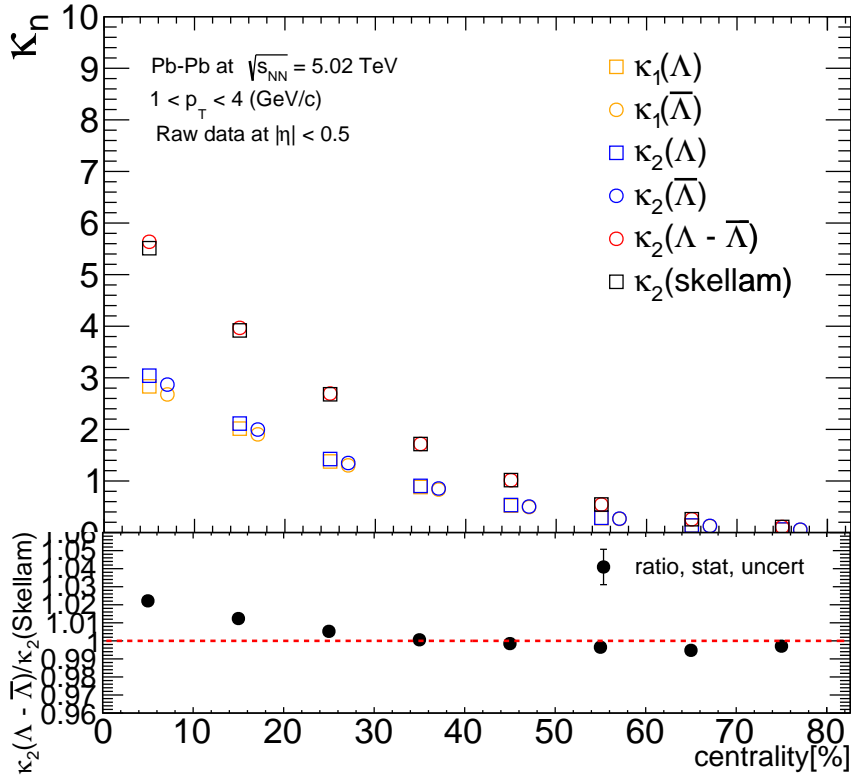


Figure 6.1: Centrality dependence of the first two raw cumulants of Λ , $\bar{\Lambda}$ and net- Λ distribution. The ratio plot is a comparison of the variance of the net- Λ distribution (red circles) to a Poisson distribution —Skellam (black boxes). The Skellam is a sum of the Λ and $\bar{\Lambda}$ distributions. The single first and second moments are the orange and blue points respectively.

From fig. 6.1 it can be seen that the mean and variance decrease with centrality class. This is expected because the larger centrality class (0-10%) contains larger number of participating nucleons during the collision. The inverse is true for the most peripheral centrality class (70-80%). The ratio plot is a comparison of the second cumulant of the net- Λ distribution, $\kappa_2(\Lambda - \bar{\Lambda})$, to the Skellam distribution. The Skellam is a sum of two Poisson distributions. Since a Poisson distribution is only defined by its mean (see section 4.1 and 4.4.2), the variance should be consistent with the mean. Thus, a comparison of the variance to the mean will show that the distribution is non-Poissonian or more interestingly, if there are true fluctuations present. In the raw counts (without background and weak decays removal), the ratio plot shows values above unity in the first 3 centrality classes. This is because the variance is slightly larger than the mean due to contaminants (background and secondaries) in the event-by-event Λ and $\bar{\Lambda}$ distribution.

6.2 Centrality dependence of the background and feed-down corrected Λ , $\bar{\Lambda}$ and net- Λ cumulants

The signal chosen for analysis in the invariant mass axis: $1.11 < \text{inv. mass} < 1.122$ [GeV/ c^2] (see section 5.2 and 5.2.1), consists of background and weak decays (section 5.3.1). The contribution of weak decays and background due to fake pairs, i.e. daughter tracks that combine to form the Λ and $\bar{\Lambda}$ invariant mass that are not true daughters, is on the order of $\approx 33\%$ in the 0-10% centrality class. The contribution from both background and weak decays are removed on a centrality and p_T dependent basis —see figures 5.12 and 5.15, respectively. Fig. 6.2 shows the cumulants after removal of the contribution due to background and weak decays. It can be seen that the mean and variance reduce after the correction for background and weak decays. In addition, the ratio plot is closer to unity after the removal of the contaminants from background and weak decays. It can also be seen that the mean (orange points) and the variance (blue points) converge, indicating that the distribution is indeed Poissonian. The second cumulant of the net- Λ distribution can be represented as a sum of the second moments of the Λ and $\bar{\Lambda}$ distributions plus the correlation term

for joint probability distributions of Λ s and $\bar{\Lambda}$ s:

$$\kappa_2(\Lambda - \bar{\Lambda}) = \kappa_2(\Lambda) + \kappa_2(\bar{\Lambda}) - 2(\langle N_\Lambda N_{\bar{\Lambda}} \rangle - \langle N_\Lambda \rangle \langle N_{\bar{\Lambda}} \rangle) \quad (86)$$

Eq. 86 shows that, in the absence of correlations between Λ and $\bar{\Lambda}$, the second cumulant of net- Λ is exactly equal to the sum of the second moments of the Λ and $\bar{\Lambda}$ distributions, $\kappa_2(\Lambda)$ and $\kappa_2(\bar{\Lambda})$ respectively. Given that the Λ and $\bar{\Lambda}$ distribution is Poissonian in nature, its higher order cumulants are equal to the mean. That is,

$$\kappa_2(\Lambda) + \kappa_2(\bar{\Lambda}) = \kappa_1(\Lambda) + \kappa_1(\bar{\Lambda}) \rightarrow \kappa_2(\text{Skellam}) \quad (87)$$

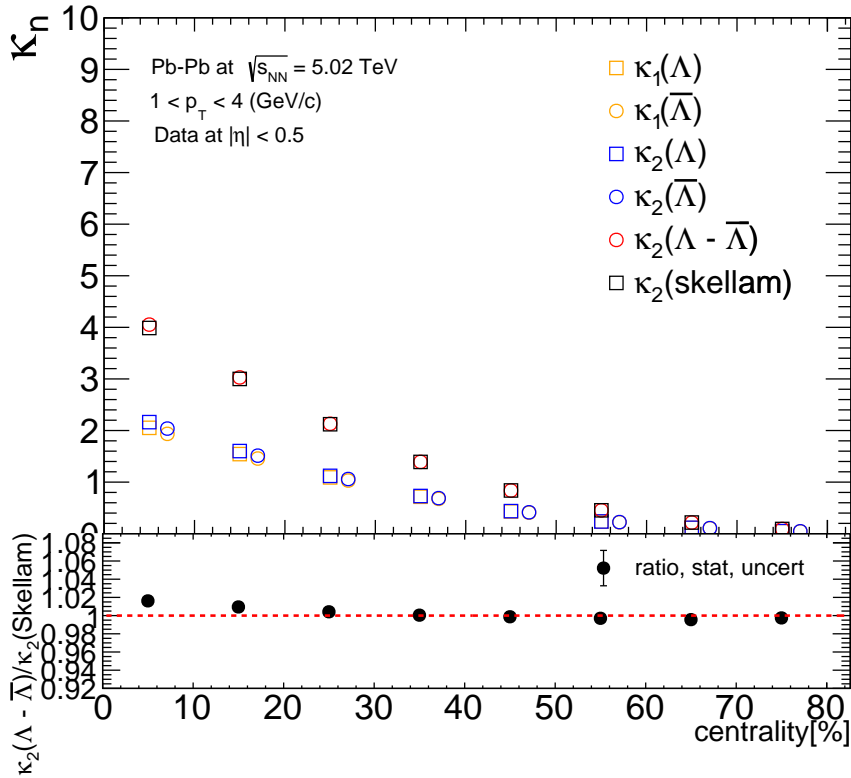


Figure 6.2: Centrality dependence of the first two cumulants of Λ , $\bar{\Lambda}$ and net- Λ distribution corrected for background and feed-down. The ratio of $\kappa_2(\Lambda - \bar{\Lambda})$ to $\kappa_2(\text{Skellam})$ approaches unity in all centrality classes after correction for background and weak decays.

6.3 Centrality dependence of the efficiency corrected Λ , $\bar{\Lambda}$ and net- Λ cumulants

Efficiency losses are expected in the experiment due to finite acceptance of the detector. That is, particles are detected with a probability, ε , that is dependent on transverse momentum and centrality (see section 5.3.2). For the Λ particle, ε ranges from 5% to 15% along the p_T axis in the 0-10% centrality class. In general, the efficiency improves with increasing transverse momentum and decreasing centrality. This shows that high multiplicity and low momentum negatively affects the detection efficiency. The efficiency corrected results can be found in fig. 6.3. The same labeling on the data points were used as in sections 6.1 and 6.2.

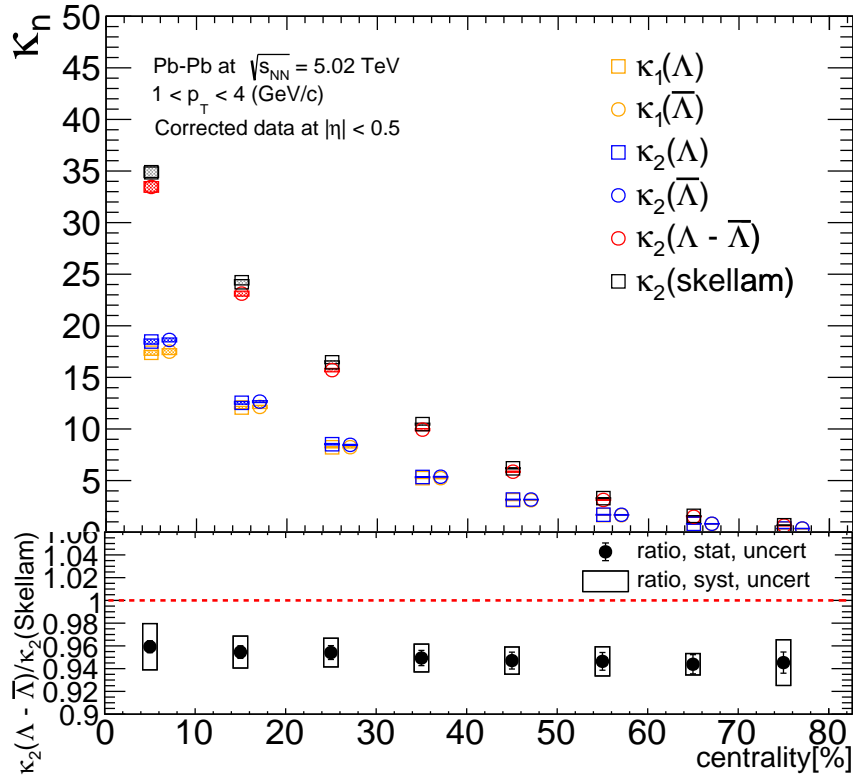


Figure 6.3: Experimentally measured first and second cumulants of the Λ , $\bar{\Lambda}$ and net- Λ distributions corrected for efficiency. The bottom panel is the corresponding ratio of the net- Λ second cumulant to the Skellam baseline.

In addition, the plot contains systematic errors, which are the shaded boxes in the single and net cumulants (in the top panel), and the open rectangular boxes in the ratio plot. From fig. 6.3, it can be seen that the ratio of the second cumulant of the net- Λ distribution to Skellam baseline deviates from unity after correcting for efficiency losses. From Eq. 86, it can be inferred that the reason for the deviation from unity may be due to the presence of a correlation term. As already stated, the presence of the correlation term can be linked to the true fluctuations under investigation. As a result, the emergence of a correlation term after correcting for efficiency losses was further investigated and presented in section 6.6. Section 6.6 investigates the effect of experimental acceptance cuts on the measured second order cumulant.

6.4 Comparison of Λ , $\bar{\Lambda}$ and net- Λ cumulants to HIJING

The HIJING Monte Carlo (MC) event generator was also studied for fluctuation measurements of the Λ , $\bar{\Lambda}$ and net- Λ distributions. The HIJING MC event generator takes in kinematic parameters like collision energy, collision system, and parton distribution functions (PDFs) to simulate events like in real data [73].

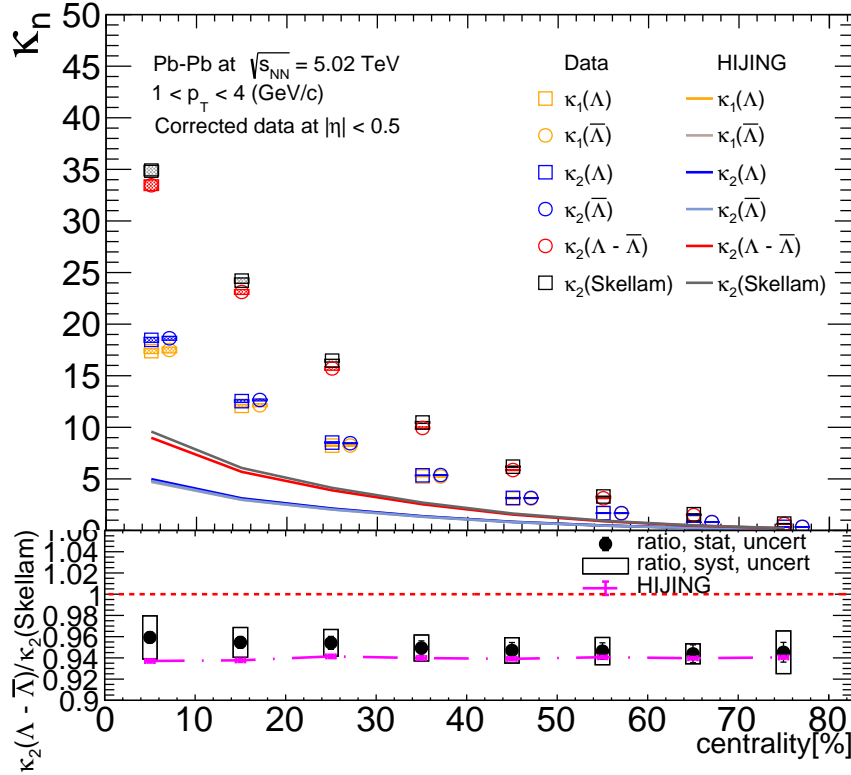


Figure 6.4: Experimentally measured first and second cumulants of the Λ , $\bar{\Lambda}$ and net- Λ distributions compared to HIJING MC generated events. The lines are the corresponding cumulants from HIJING. Note that the single first moments and second moments from HIJING closely converge.

Fig. 6.4 shows a comparison of the measured data to the prediction from HIJING MC event generator. Although HIJING describes the trend with centrality quite well, it significantly underestimates the magnitude of the measured cumulants from data. It is consistent, however, in the ratio of $\kappa_2(\Lambda - \bar{\Lambda})$ to $\kappa_2(Skellam)$ with the measured data.

6.5 Comparison of Λ , $\bar{\Lambda}$ and net- Λ cumulants to net-protons at ALICE

The first and second fluctuation measurements for the net-proton multiplicity distributions have been studied at ALICE [70]. Fig. 6.5 shows a comparison of the cumulants of the event-by-event proton and lambda distributions. A qualitative agreement is present between the two fluctuation measurements in spite of the difference in kinematics cuts and contributions due to resonant decays.

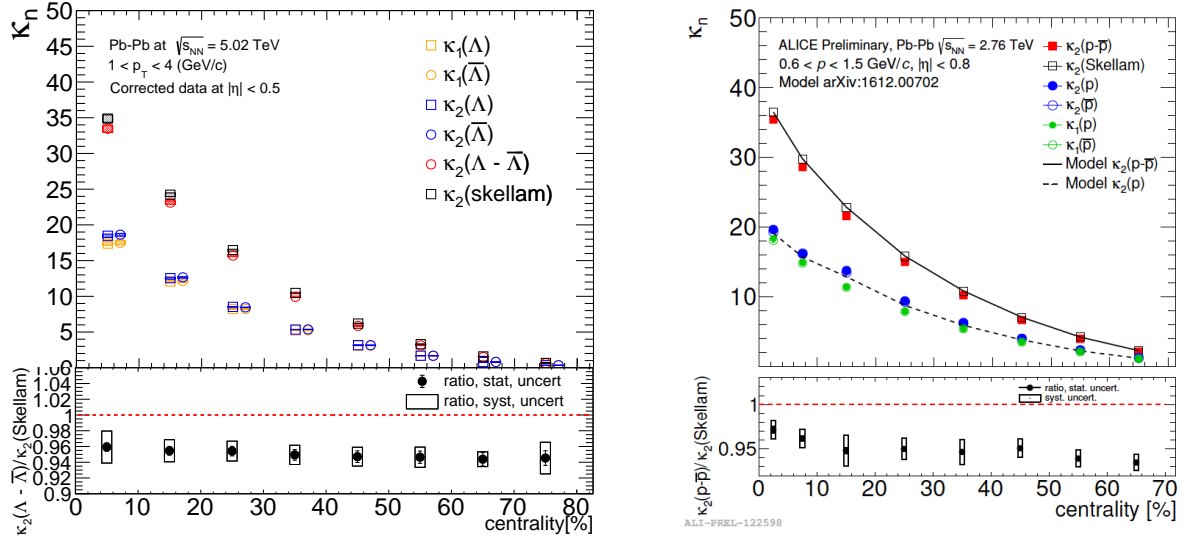


Figure 6.5: Experimentally measured first and second cumulants of the Λ , $\bar{\Lambda}$ and net- Λ distributions compared to measured p , \bar{p} and net- p cumulants from ALICE. The net-proton results plot is taken from [70].

In addition, the deviation of net-particle second cumulant from the Skellam expectation is present in the net-proton fluctuation measurement. In the net-proton analysis, the observed deviation from the Skellam expectation was attributed to global baryon number conservation [70] (see section 4.4.2). As a result, the measured second order cumulant of the net- Λ distribution was also investigated for global baryon number conservation.

6.6 Pseudorapidity dependence of ratio of $\kappa_2(\Lambda - \bar{\Lambda})$ to $\kappa_2(\text{skellam})$

The effects of global conservation laws can be tested by exploring the dependence of the measured cumulants on the pseudorapidity acceptance, $\Delta\eta$. As already discussed in section 4.4.2, the kinematic pseudorapidity correlation length of the system is of the order $\Delta\eta \approx 1$ [67]. It is expected that a pseudorapidity acceptance smaller than the pseudorapidity extent of particle production will lead to only Poissonian fluctuations. On the other hand, if the pseudorapidity acceptance in which the cumulants are measured is larger, the effects of global conservation laws become large.

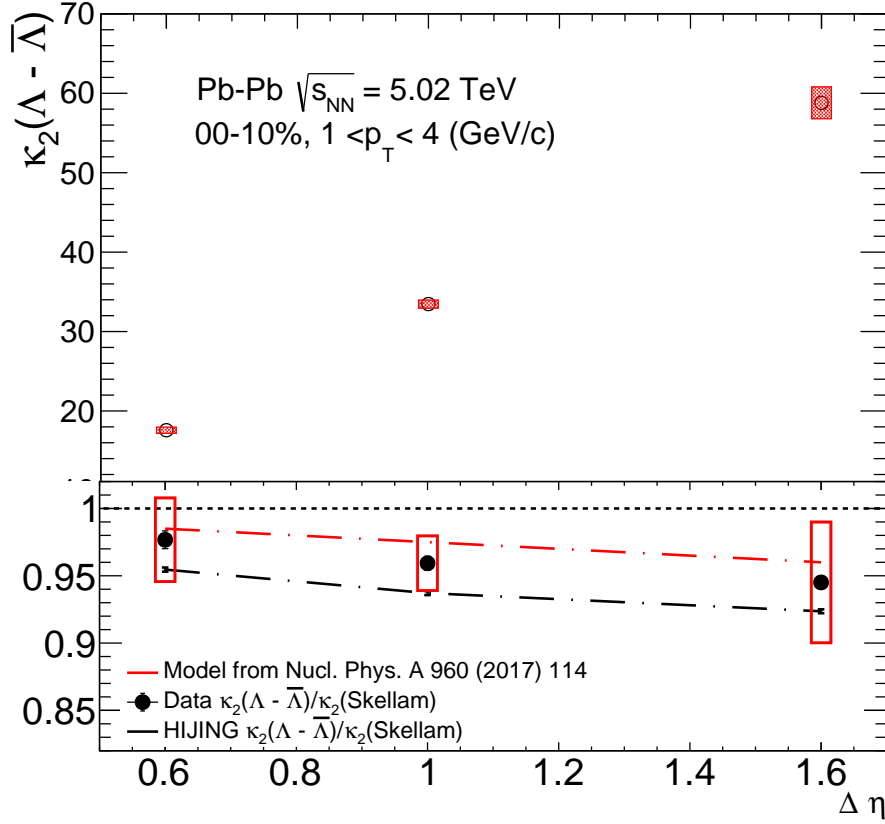


Figure 6.6: The pseudorapidity dependence of the second cumulant of net- Λ fluctuation measurement (top panel) and the ratio to Skellam baseline (bottom panel) in 0-10% centrality class. The ratio is compared to expectation from a model incorporating effects of global baryon number conservation (red dashed line) and to HIJING MC generator (dashed black line).

For the second cumulants (Eq. 86), the correlation term arising from global baryon number conservation depends only on the acceptance factor, α , (already discussed in section 4.4.2). The acceptance factor is a ratio of the mean number of measured lambdas inside the acceptance to the mean number of baryons in full phase space. The mean number of baryons in full phase space is obtained via HIJING simulations [68]. The acceptance factor is assumed to be the same for baryons and anti-baryons.

Fig. 6.6 shows a plot of the second cumulant of the net- Λ multiplicity distribution and its ratio to $\kappa_2(\text{Skellam})$ in different pseudorapidity acceptance, $\Delta\eta$. The analysis was performed in 3 different pseudorapidity ranges: $|\eta| < 0.3$, $|\eta| < 0.5$, and $|\eta| < 0.8$. As seen from fig. 6.6, at pseudorapidity acceptance of $|\eta| < 0.3$, the experimentally measured net- Λ distribution follows a Skellam distribution. This is in agreement with the Poisson fluctuation expectation when the acceptance is less than $|\eta| < 0.4$ (discussed in section 4.4.2). With large enough acceptance (beyond $|\eta| > 0.5$), which corresponds to $\Delta\eta > 1$, the deviation from the Skellam expectation becomes apparent. The degree of deviation is in good agreement with the red dashed line —based on a model including effects of global baryon number conservation. It is therefore concluded that the deviation of the second cumulant of the net- Λ multiplicity distribution from the Skellam baseline is due to global baryon number conservation. It is also noted that the deviation of the second cumulant from the Skellam baseline is also consistent with HIJING predictions (black dashed lines of fig. 6.6).

6.7 Conclusions and future directions

In summary, the first two cumulants of the net- Λ multiplicity distribution were presented in this dissertation. It was assumed and verified that the individual Λ and $\bar{\Lambda}$ are Poissonian, and thus any higher order cumulants should be comparable to the mean of the multiplicity distribution. Further analysis showed that the deviation from Poisson behavior in the second cumulant is due to global baryon number conservation. It is important to note that the Λ particle carries baryon and strangeness quantum numbers. It was not known, a priori, if the Λ s are predominantly governed by their baryon quantum number or strangeness quantum number. Its agreement to global baryon number conservation appear to indicate that the Λ particle behaves like a baryon.

Fluctuation measurements of the net- Λ multiplicity distribution at the STAR experiment [46] seem to indicate that the Λ particle may behave like both. However, it appeared to be the case that the Λ particle behaves like a strange baryon at the lower collision energy (19 GeV). Moreover, cumulant ratios compared to HRG predictions used to extract a freeze-out surface indicate that the Λ particle behaves like the kaon (carrying strangeness) in the lower cumulant ratios, and like the protons (carrying baryon number) in the higher cumulant ratios (see fig. 2.5).

It is apparent, that the complete behavior of the Λ particle is not yet understood. Further studies on higher order cumulants of the net- Λ multiplicity distribution are needed so as to compare to theoretical predictions that can shed more light on the interplay between strangeness and baryon number conservation in net- Λ multiplicity fluctuation measurements; as well as to better understand the strangeness and baryon freeze-out surfaces, if they are indeed different in experiment.

A Appendices

A.1 Polynomial fits to Λ and $\bar{\Lambda}$ Invariant masses

The reconstructed Λ and $\bar{\Lambda}$ Invariant masses contain residual background due combinatoric pairs. The signal range on the invariant mass axis where the Λ and $\bar{\Lambda}$ are counted event-by-event is $1.11 < \text{inv. mass} < 1.122 \text{ GeV}/c^2$. The contribution to the signal from the background was estimated by fitting the invariant masses with a polynomial function of degree 1. This is done by extracting the invariant masses in centrality and p_T bins. The centrality bin ranges from 0-80%, with steps of 10, which results in a total of 8 centrality bins. The p_T bins ranges from 1.0-4.0 GeV/c, with steps of 0.1 in $1.0 < p_T < 2.0 \text{ GeV}/c$ and with steps of 0.2 in $2.0 < p_T < 4.0 \text{ GeV}/c$. Altogether, there are (160×2) Λ and $\bar{\Lambda}$ invariant masses. The fits to the Λ invariant masses within: $1.0 < p_T < 2.0 \text{ GeV}/c$ and 0-10% centrality class can be found in fig. A.1. And the fits to the Λ invariant masses within: $2.0 < p_T < 4.0 \text{ GeV}/c$ and 0-10% centrality class are found in fig. A.2. Corresponding fits to the $\bar{\Lambda}$ Invariant masses are presented in figures A.3 and A.4 respectively.

A.2 Hagedorn fits to Ξ^+ and Ξ^- spectra

The corrected measured Ξ^+ and Ξ^- spectra were provided by the ALICE PWGLF-Strangeness PAG [72]. The spectra were fitted with a Hagedorn function to estimate the counts of Ξ . The p_T binning is: [0.8, 1.0, 1.2, 1.4, 1.6, 1.8, 2.0, 2.2, 2.4, 2.6, 2.8, 3.0, 3.2, 3.4, 3.6, 3.8, 4.0, 4.2, 4.4, 4.6, 4.8, 5.0, 5.5, 6.0, 7.0, 8.0] GeV/c. The counts of Ξ are then multiplied with the feed-down matrix (see fig. 5.14), which gives the correspondence between the p_T of the mother, Ξ , and the p_T of the daughter, Λ . The multiplication of the counts of Ξ with the feed-down matrix gives the counts of secondary Λ or $\bar{\Lambda}$ (see section 5.3.1). The fits to the Ξ^- and Ξ^+ spectra can be found in figures A.5 and A.6 respectively.

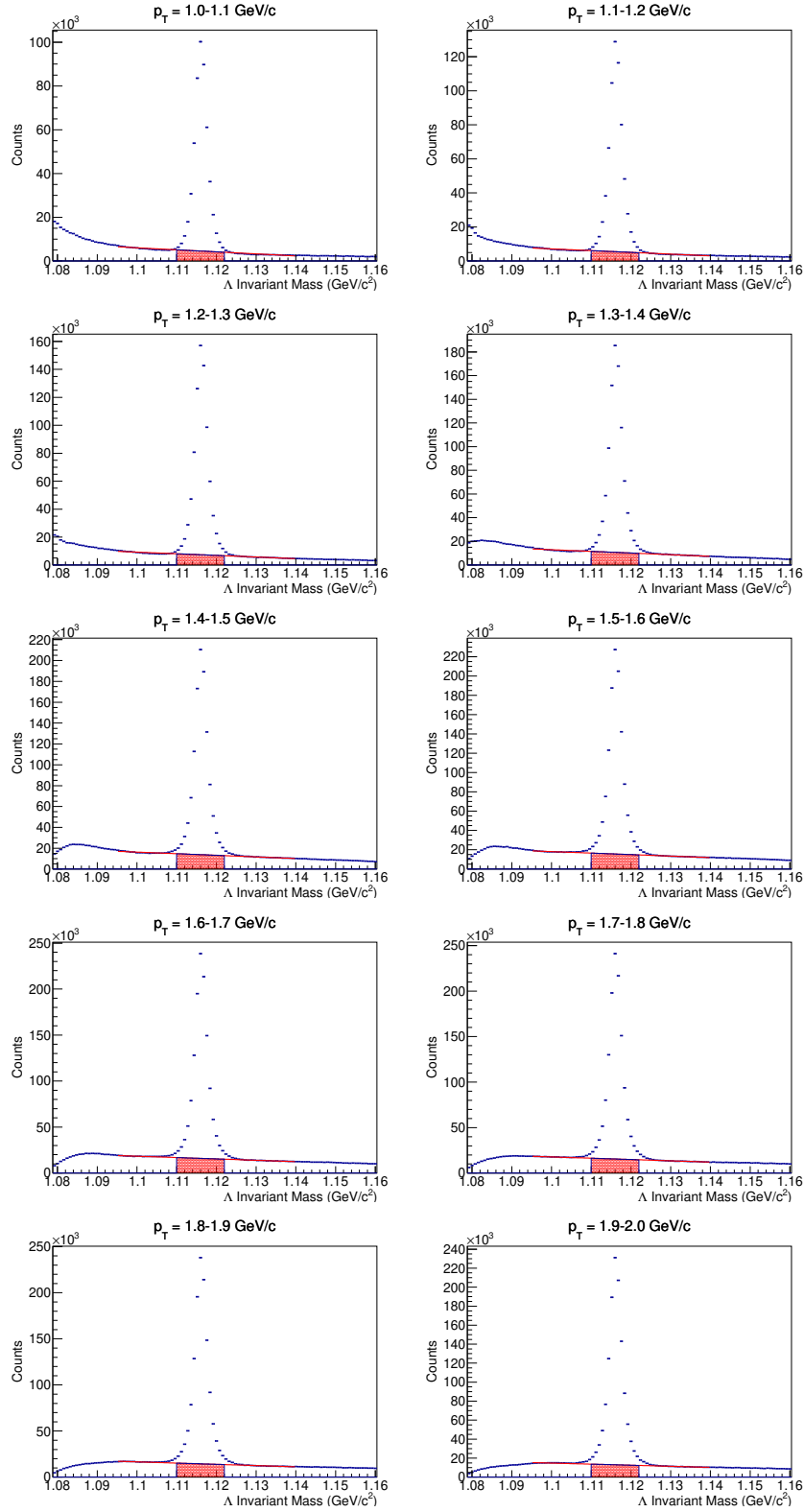


Figure A.1: Background estimation from linear fits to Λ invariant masses within p_T range: [1.0 - 2.0 GeV/c].

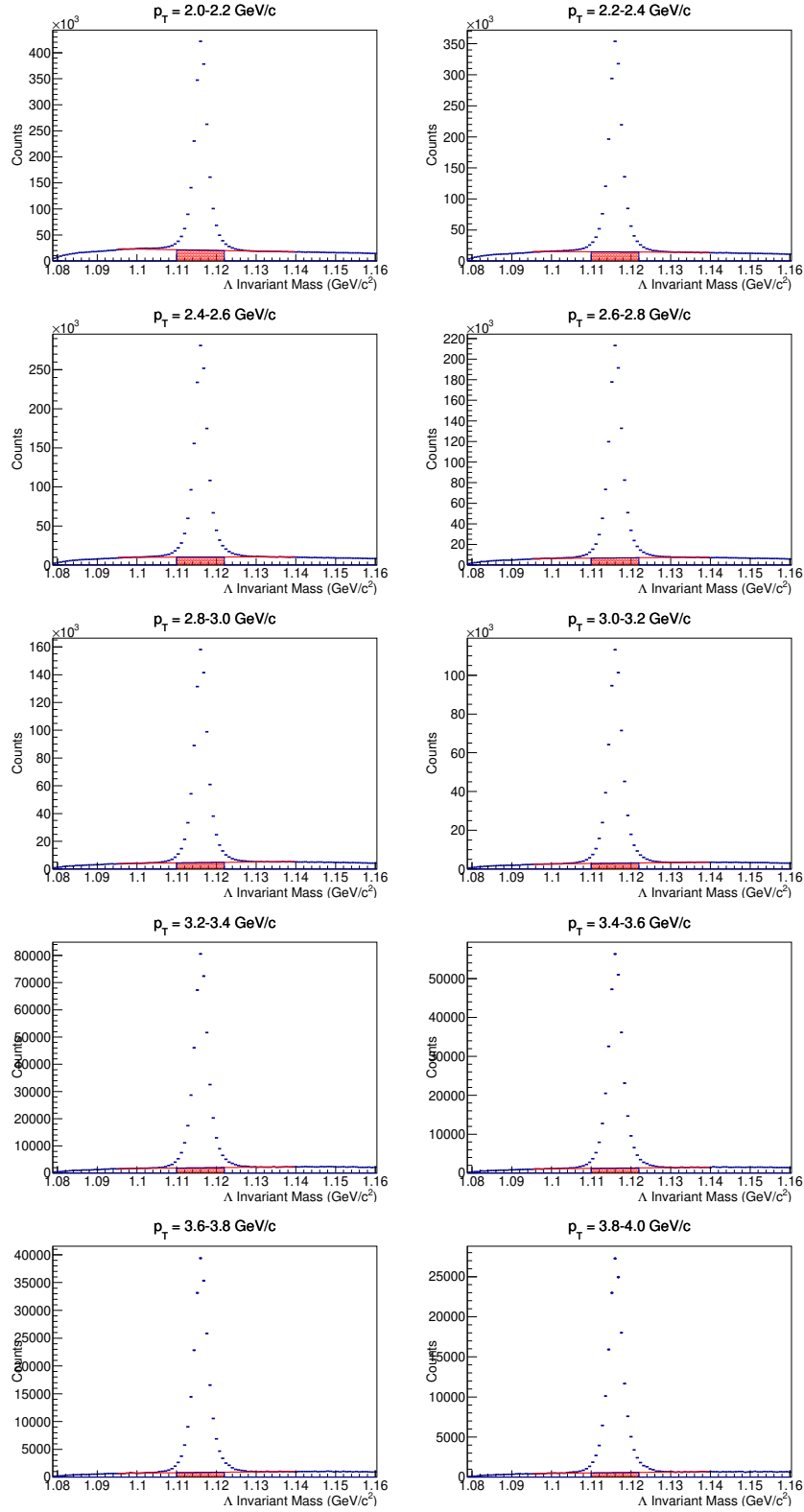


Figure A.2: Background estimation from linear fits to Λ invariant masses within p_T range: [2.0 - 4.0 GeV/c].

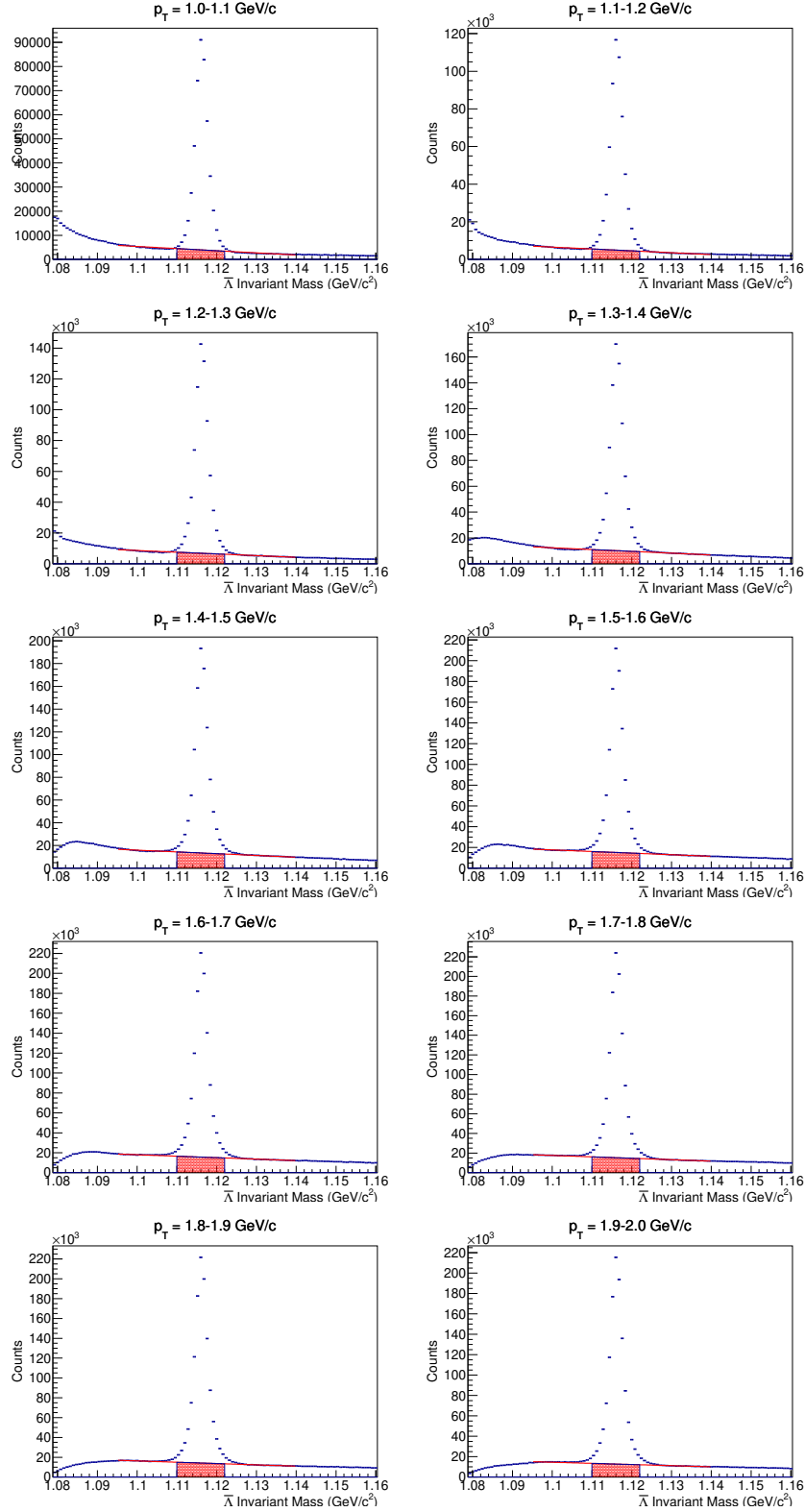


Figure A.3: Background estimation from linear fits to $\bar{\Lambda}$ invariant masses within p_T range: [1.0 - 2.0 GeV/c].

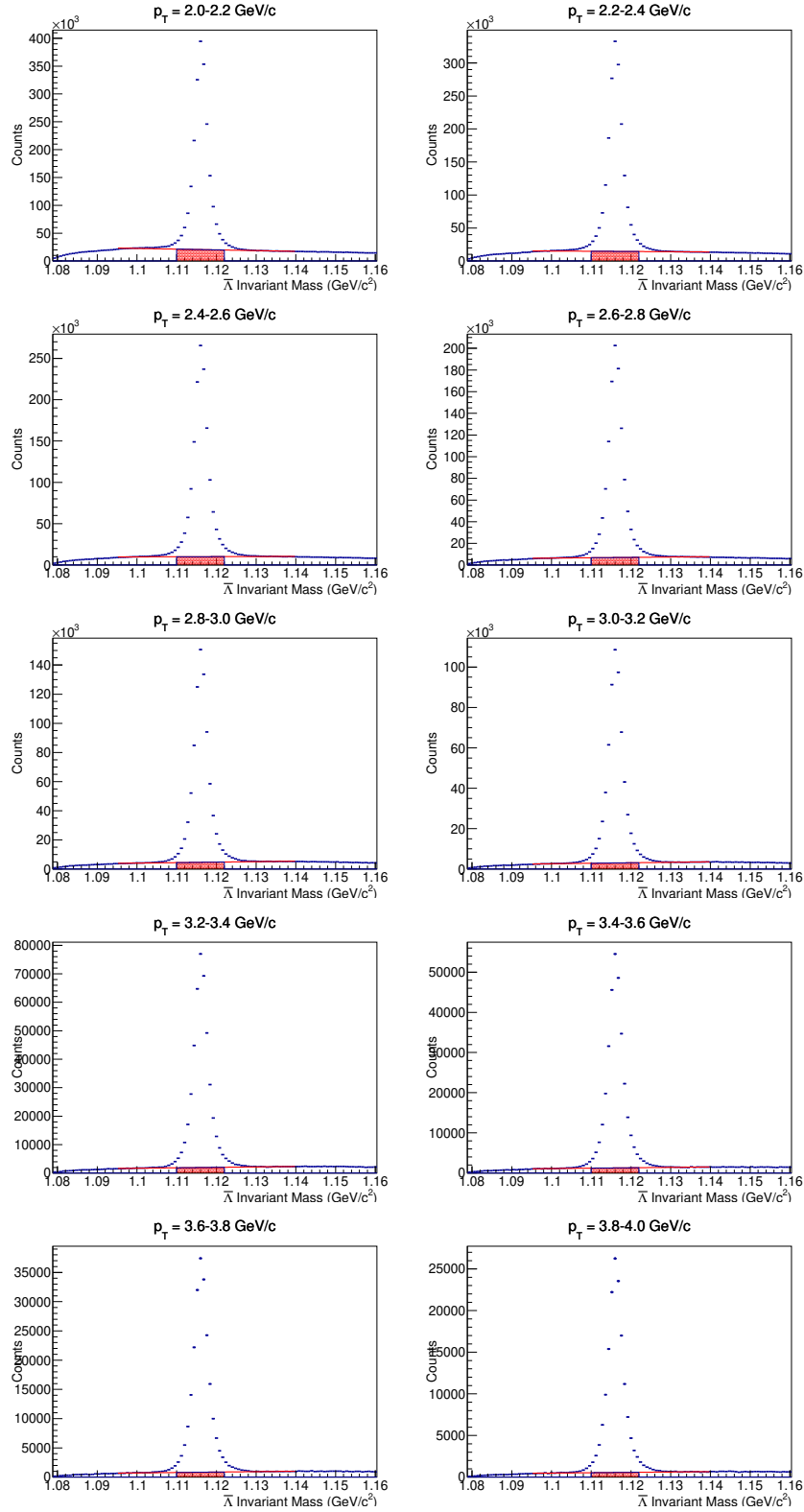


Figure A.4: Background estimation from linear fits to $\bar{\Lambda}$ invariant masses within p_T range: [2.0 - 4.0 GeV/c].

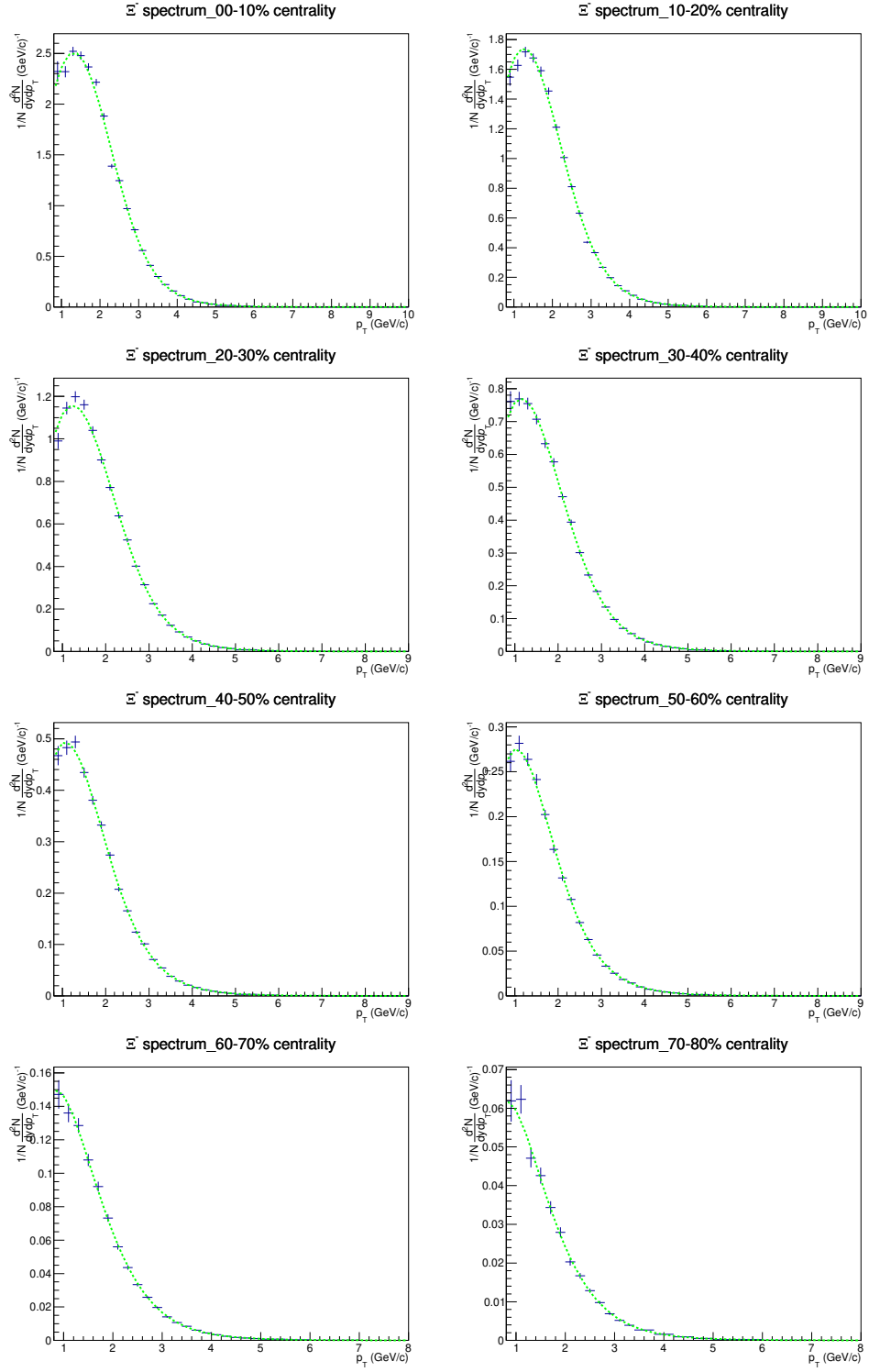


Figure A.5: Ξ^- spectra measured in $\sqrt{s_{NN}} = 5.02$ TeV Pb-Pb collisions with the Hagedorn fits in green to smooth out the spectra. The counts of Ξ^- are used to estimate the feed-down to Λ .

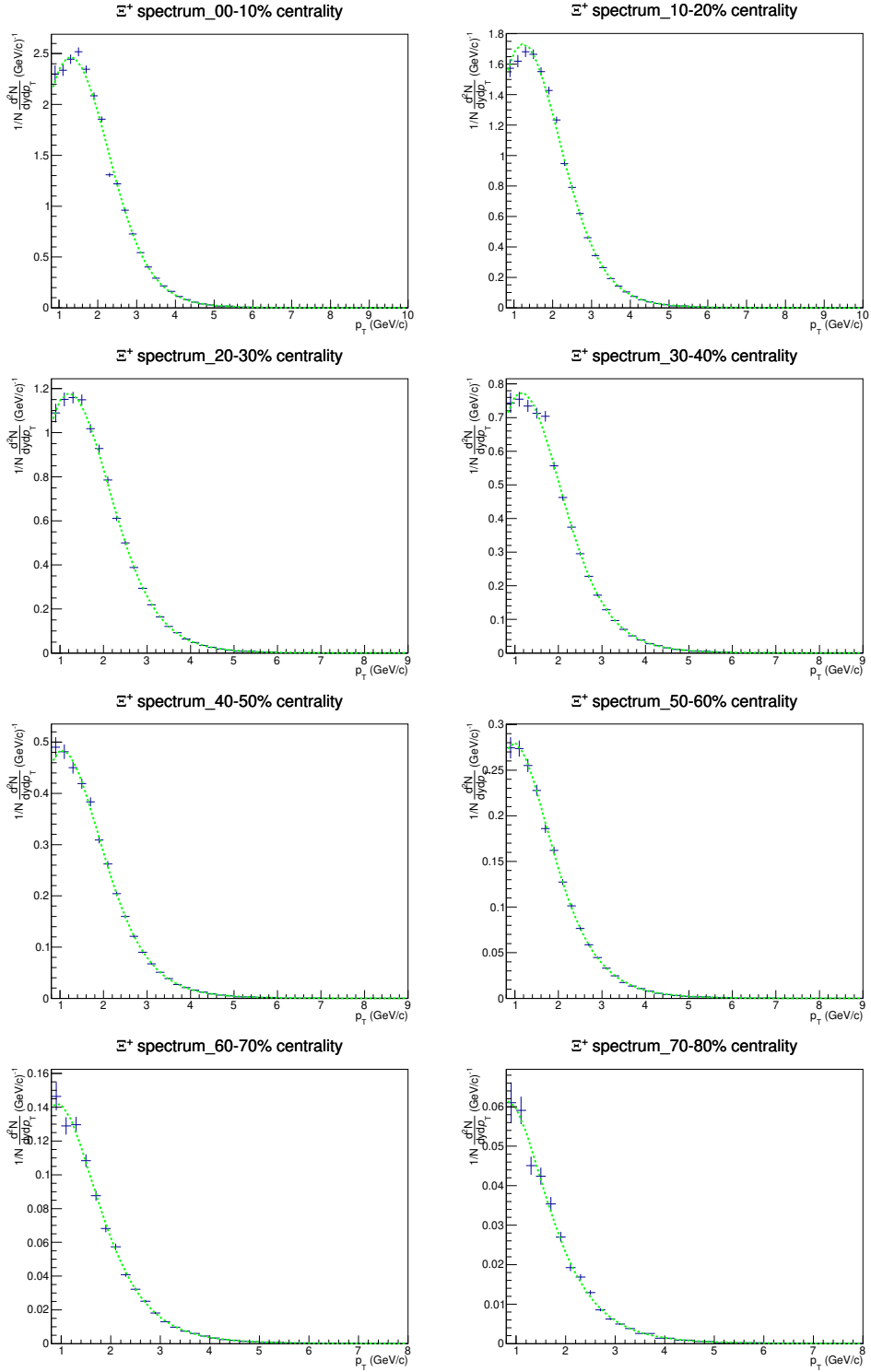


Figure A.6: Ξ^+ spectra measured in $\sqrt{s_{NN}} = 5.02$ TeV Pb-Pb collisions with the Hagedorn fits in green to smooth out the spectra. The counts of Ξ^+ are used to estimate the feed-down to $\bar{\Lambda}$.

Bibliography

- [1] BNL Newsroom, “RHIC Scientists Serve Up ‘Perfect’ Liquid”, <https://www.bnl.gov/newsroom/news.php?a=110303>.
- [2] Relativistic Heavy Ion Collider at the Brookhaven National Laboratory. <https://www.bnl.gov/rhic>.
- [3] DESY Collaboration, “On the discovery of the gluon”, *Eur. Phys. J. H* **35**, (2010) 3-28.
- [4] G. Ecker, “Quantum chromodynamics”, arXiv:0604165 [hep-ph].
- [5] M. Stephanov, “QCD phase diagram: an overview”, arXiv:0701002 [hep-lat].
- [6] Davies, C. T. H., Follana, E. Gray, A. Lepage, G. P. Mason, Q. Nobes, M. Shigemitsu, J. Trotter, H. D. Wingate, M. Aubin, C. Bernard, C., “High-Precision Lattice QCD Confronts Experiment”, *Phys. Rev. Lett.* **92**, (2004) 022001, arXiv:0304004 [hep-lat].
- [7] Elliott D. Bloom et al, “High-Energy Inelastic e-p Scattering at 6-Degrees and 10-Degrees”, *Phys. Rev. Lett.* **23** (1969) 930–934.
- [8] D. J. Gross and F. Wilczek, “Ultraviolet behavior of nonabelian gauge theories”, *Phys. Rev. Lett.* **30** (1973) 1343.
- [9] W. E. Caswell, “Asymptotic behavior of nonabelian gauge theories to two-loop order”, *Phys. Rev. Lett.* **33** (1974) 244.
- [10] D. R. T. Jones, “Two Loop Diagrams in Yang-Mills Theory”, *Nucl. Phys.* **B75** (1974) 531.
- [11] A. Deur, S.J. Brodsky, G.F. de Teramond, “QCD Running Coupling”, arXiv:1604.08082 [hep-ph].
- [12] CMS Collaboration, “Measurement and QCD analysis of double-differential inclusive jet cross sections in pp collisions at $\sqrt{s} = 8$ TeV and cross section ratios to 2.76 and 7 TeV”, arXiv:1609.05331v2 [hep-ex].
- [13] B. Andersson, G. Gustafson, G. Ingelman, and T. Sjöstrand, “Parton fragmentation and string dynamics”, *Phys. Rept.*, **97** (1983) 31 – 145.
- [14] R. Hagedorn, “Statistical thermodynamics of strong interactions at high-energies”, *Nuovo Cim. Suppl.*, **3** (1965) 147–186.
- [15] J. C. Collins and M. J. Perry, “Superdense matter: Neutrons or asymptotically free quarks?”, *Phys. Rev. Lett.* **34** (1975) 1353.
- [16] M. C. Abreu, et al., “Observation of a threshold effect in the anomalous J/ψ suppression”, *Phys. Lett.* **B45** (1999) 456-466.
- [17] E. Andersen, et al., “Strangeness enhancement at mid-rapidity in Pb Pb collisions at 158-A-GeV/c”, *Phys. Lett.* **B449** (1999) 401-406.

- [18] K. Adcox, et al., “Suppression of hadrons with large transverse momentum in central Au+Au collisions at $\sqrt{sNN}=130$ -GeV”, Phys. Rev. Lett. **88** (2002) 022301, arXiv:0109003 [nucl-ex].
- [19] K. H. Ackermann, et al., “Elliptic flow in Au + Au collisions at $\sqrt{sNN}=130$ GeV”, Phys. Rev. Lett. **86** (2001) 402-407, arXiv:0009011 [nucl-ex].
- [20] B. B. Back, et al., “The PHOBOS perspective on discoveries at RHIC”, Nucl. Phys. **A757** (2005) 28-101, arXiv:0410022 [nucl-ex].
- [21] I. Arsene, et al., “Quark gluon plasma and color glass condensate at RHIC?”, arXiv:0410020 [nucl-ex].
- [22] K. Adcox, et al., “Formation of dense partonic matter in relativistic nucleus-nucleus collisions at RHIC: Experimental evaluation by the PHENIX collaboration”, Nucl. Phys. **A757** (2005) 184-283, arXiv:0410003 [nucl-ex].
- [23] J. Adams, et al., “Experimental and theoretical challenges in the search for the quark gluon plasma: The STAR Collaboration’s critical assessment of the evidence from RHIC collisions”, Nucl. Phys. **A757** (2005) 102-183, arXiv:0501009 [nucl-ex].
- [24] R. D. Pisarski, F. Wilczek, “Remarks on the Chiral Phase Transition in Chromodynamics”, Phys. Rev. **D29** (1984) 338-341.
- [25] Y. Aoki, G. Endrodi, Z. Fodor, S. D. Katz, K. K. Szabo, “The order of the quantum chromodynamics transition predicted by the standard model of particle physics”, Nature **443** 675-678, arXiv:0611014 [hep-lat].
- [26] Y. Aoki, Z. Fodor, S. D. Katz, K. K. Szabo, “The QCD transition temperature: Results with physical masses in the continuum limit”, Phys. Lett. **B643** (2006) 46-54, arXiv:0609068 [hep-lat].
- [27] M. A. Stephanov, “QCD phase diagram and the critical point, Prog. Theor. Phys. Suppl. **153** (2004) 139–156, arXiv:0402115 [hep-ph].
- [28] M. A. Stephanov, K. Rajagopal, E. V. Shuryak, “Signatures of the tricritical point in QCD”, Phys. Rev. Lett. **81** (1998) 4816–4819, arXiv:9806219 [hep-ph].
- [29] Wilson, K., “Confinement of quarks”, Phys. Rev. **D10** (1974) 2445-2459.
- [30] C. Allton, S. Ejiri, S. Hands, O. Kaczmarek, F. Karsch, et al., “The QCD thermal phase transition in the presence of a small chemical potential”, Phys. Rev. **D66** (2002) 074507, arXiv:0204010 [hep-lat].
- [31] P. Braun-Munzinger, J. Stachel, J. P. Wessels, N. Xu, “Thermal equilibration and expansion in nucleus-nucleus collisions at the AGS”, Phys. Lett. **B344** (1995) 43-48, arXiv:9410026 [nucl-th].
- [32] P. Braun-Munzinger, J. Stachel, C. Wetterich, “Chemical freezeout and the QCD phase transition temperature”, Phys. Lett. **B596** (2004) 61-69, arXiv:0311005 [nucl-th].

- [33] Andronic A, Braun-Munzinger P and Stachel J 2007, “Heavy Ion Collisions at the LHC: Last Call for Predictions”, arXiv:0707.4076 [nucl-th].
- [34] A. Andronic, “An overview of the experimental study of quark-gluon matter in high-energy nucleus-nucleus collisions”, *Int. J. Mod. Phys.* **A29** (2014) 1430047, arXiv:1407.5003 [nucl-th].
- [35] STAR Collaboration, “Identified particle production, azimuthal anisotropy, and interferometry measurements in Au+Au collisions at $\sqrt{s_{NN}} = 9.2$ GeV”, *Phys. Rev.* **C81**, (2010) 024911, arXiv:0909.4131 [nucl-ex].
- [36] J. Cleymans, H. Oeschler, K. Redlich, “Influence of Impact Parameter on Thermal Description of Relativistic Heavy Ion Collisions at GSI/SIS”, *Phys. Rev.* **C59** (1999) 1663, arXiv:9809027 [nucl-th].
- [37] STAR Collaboration, “Scaling properties at freeze-out in relativistic heavy ion collisions”, *Phys. Rev.* **C83**, (2011) 034910, arXiv:1008.3133 [nucl-ex].
- [38] A. Bazavov, et al., “Equation of state in (2+1)-flavor QCD”, *Phys. Rev.* **D90** (2014) 094503, arXiv:1407.6387 [hep-lat].
- [39] Heng-Tong Ding, Frithjof Karsch, and Swagato Mukherjee, “Thermodynamics of strong-interaction matter from Lattice QCD”, arXiv:1504.05274 [hep-lat].
- [40] S. Borsanyi, Z. Fodor, S.D. Katz, S. Krieg, C. Ratti, K. K. Szabo “Freeze-out parameters: lattice meets experiment”, arXiv:1305.5161v1 [hep-lat].
- [41] Masayuki Asakawa, Ulrich Heinz, and Berndt Müller, “Fluctuation Probes of Quark Deconfinement”, *Phys. Rev. Lett.* **85** (2000) 2072.
- [42] F. Karsch and K. Redlich, “Probing freeze-out conditions in heavy ion collisions with moments of charge fluctuations”, *Phys. Lett.* **B695** (2011) 136, arXiv:1007.2581 [hep-ph].
- [43] S. Borsanyi, Z. Fodor, S. Katz, S. Krieg, C. Ratti, et al., “Freeze-out parameters from electric charge and baryon number fluctuations: is there consistency?” *Phys.Rev.Lett.* **113** (2014) 052301, arXiv:1403.4576 [hep-lat].
- [44] J Stachel, A Andronic, P Braun-Munzinger, K Redlich, “Confronting LHC data with the statistical hadronization model”, arXiv:1311.4662v1 [nucl-th].
- [45] R. Bellwied, S. Borsanyi, Z. Fodor, S. D. Katz and C. Ratti, “Is There a Flavor Hierarchy in the Deconfinement Transition of QCD?” *Phys. Rev. Lett.* **111** , (2013) 202302.
- [46] STAR Collaboration, “Beam energy dependence of net- Λ fluctuations measured by the STAR experiment at RHIC”, arXiv:2001.06419v1 [nucl-ex].
- [47] ALICE Collaboration, “Performance of the ALICE Experiment at the CERN LHC”, *Int. J. Mod. Phys.* **A29** (2014) 1430044, arXiv:1402.4476 [nucl-ex].
- [48] ALICE Collaboration, “The ALICE experiment at the CERN LHC,” *JINST* **3** (2008) S08002.
- [49] ALICE collaboration, “ALICE time projection chamber: Technical Design Report”, CERN-LHCC-2000-001. <http://cdsweb.cern.ch/record/451098>.

- [50] C. Lippmann, “Performance of the ALICE Time Projection Chamber”, *Physics Procedia* **37** (2012) 434–441.
- [51] <https://home.cern/resources/brochure/cern/quick-facts>.
- [52] ALICE Collaboration, “Definition of the ALICE coordinate system and basic rules for sub-detector components numbering”, ALICE-INT-2003-038 (2003).
- [53] ALICE Collaboration, “The ALICE experiment at the CERN LHC”, *JINST* **3** (2008) S08002.
- [54] J. Alme et al., “The ALICE TPC, a large 3-dimensional tracking device with fast readout for ultra-high multiplicity events”, *Nucl. Instrum. Meth.* **A622** (2010) 316-367, arXiv:1001.1950 [physics.ins-det].
- [55] ALICE Collaboration, “Highlights of the production of (anti-)(hyper-)nuclei and exotica with ALICE at the LHC”, AIP Conference Proceedings **2130** (2019) 020017.
- [56] C. Gonzáles Gutiérrez et al., “The ALICE TPC readout control unit”, *IEEE Nucl. Sci. Symp. Conf. Rec.* **1** (2005) 575.
- [57] http://aliceinfo.cern.ch/Public/en/Chapter2/Chap2_TPC.html.
- [58] W.W.M Allison and J.H. Cobb, “Relativistic Charged Particle Identification By Energy Loss”, *Annu. Rev. Nucl. Part. Sci.* **30** (1980) 253-298.
- [59] K. A. Olive et al., ” Review of Particle Physics”, *Chinese Physics C* Vol. 38, No. 9 (2014) 090001.
- [60] Toia Alberica, “Participants and spectators at the heavy-ion fireball”, CERN COURIER (2013). <http://cds.cern.ch/record/1998037?ln=en>.
- [61] ALICE Collaboration, “Centrality determination in heavy ion collisions”, ALICE-PUBLIC-2018-011 (2018).
- [62] ALICE Collaboration, “Centrality dependence of the charged-particle multiplicity density at mid-rapidity in Pb–Pb collisions at $\sqrt{s_{NN}}=5.02$ TeV”, arXiv:1512.06104v2 [nucl-ex].
- [63] G. J. Alner et al., *Phys. Lett.* **B167** (1986) 476.
- [64] Terence J. Tarnowsky, Gary D. Westfall, “First Study of the Negative Binomial Distribution Applied to Higher Moments of Net-charge and Net-proton Multiplicity Distributions”, arXiv:1210.8102 [nucl-ex].
- [65] Xiaofeng Luo, “Unified Description of Efficiency Correction and Error Estimation for Moments of Conserved Quantities in Heavy-Ion Collisions”, arXiv:1410.3914 [physics.data-an].
- [66] X. Luo, J. Xu, B. Mohanty and N. Xu, “Volume fluctuation and auto-correlation effects in the moment analysis of net-proton multiplicity distributions in heavy-ion collisions”, *J. Phys.* **G40**, (2013) 105104.
- [67] B. Ling and M. A. Stephanov, “Acceptance dependence of fluctuation measures near the QCD critical point”, *Phys. Rev.* **C93** (2016) 034915, arXiv:1512.09125 [nucl-th].

- [68] P. Braun-Munzinger, A. Rustamov, and J. Stachel, “Bridging the gap between event-by-event fluctuation measurements and theory predictions in relativistic nuclear collisions ”, Nucl. Phys. A 960 (2017) 114–130, arXiv:1612.00702 [nucl-th].
- [69] P. Braun-Munzinger, A. Rustamov, and J. Stachel, “The role of the local conservation laws in fluctuations of conserved charges,” arXiv:1907.03032 [nucl-th].
- [70] ALICE Collaboration, “Net-baryon fluctuations measured with ALICE at the CERN LHC”, Nucl. Phys. A967 (2017) 453–456, arXiv:1704.05329 [nucl-ex].
- [71] A. Bzdak and V. Koch, “Local efficiency corrections to higher order cumulants”, Phys. Rev. C **91** (2015) 027901.
- [72] <https://alice-notes.web.cern.ch/node/588>.
- [73] Miklos Gyulassy and Xin-Nian Wang, “A Monte Carlo Program for Parton and Particle Production in High Energy Hadronic and Nuclear Collisions”, arXiv:9502021v1 [nucl-th].